Preliminary Design Study of a Micro-Gas Turbine Engine

by

Christophe Groshenry

Ingénieur, Ecole Polytechnique 1992, ENSAE 1994

Submitted to the Department of Aeronautics and Astronautics
in partial fulfillment of the requirements for the degree of

Master of Science

at the

MASSACHUSETTS INSTITUTE OF TECHNOLOGY

September 1995

Author .....
Department of Aeronautics and Astronautics
August 15, 1995

Certified by .....
Alan H. Epstein
Professor
Thesis Supervisor

Accepted by .....
Professor Harold Y. Wachman
Chairman, Department Graduate Committee

Preliminary Design Study of a Micro-Gas Turbine Engine

by

Christophe Groshenry

Submitted to the Department of Aeronautics and Astronautics
on August 16, 1995, in partial fulfillment of the
requirements for the degree of
Master of Science

Abstract

Large scale gas turbine engines provide some of the highest power densities of any continuous energy sources mankind uses. Micromachining technology appears to enable the realization of these high power densities in machines of 1 cm^3, producing up to a few tens of watts of power. In comparison, the best battery of similar dimensions can only supply from one tenth to one third of this power. If the very tight tolerances microfabrication process can be extended from silicon to high strength and high temperature capability ceramics, engine thermodynamic cycle requirements can be satisfied. This work is a preliminary design study of such a device.

For a compressor pressure ratio of 5 to 1 and a 1 mm^2 inlet area (corresponding to a $1.8 * 10^{-4}$ kg/s mass flow), break-even operation can be obtained with compressor and turbine isentropic efficiencies as low as 0.55 due to the high turbine inlet temperature achievable (1600 K) using ceramic components. Self-acting gas bearings, supplied with compressed air, could provide sufficient load capability at the rotational speeds needed ($\approx 3 * 10^6$ rpm) without consuming more than a few watts by viscous dissipation. The cycle's fuel consumption can be improved further by introducing a recuperator. A design analysis shows that a micro-heat exchanger with 75% effectiveness and 5% total pressure drops is feasible, making such a device attractive.

Optimization for minimum fuel consumption to power output ratio (PSFC) has resulted in a cycle with a $1.8 * 10^{-4}$ kg/s inlet mass flow, a 4.6 pressure ratio and 0.5 efficiency compressor, a 1600 K turbine inlet temperature and a 0.7 turbine efficiency. Up to 16 watts could be produced with 0.45 PSFC. However, compressor and turbine design for such levels of performance appear to be very challenging due to microfabrication geometric constraints.

This analysis suggests that a micro-gas turbine is feasible but points out several challenging engineering issues.

Thesis Supervisor: Alan H. Epstein
Title: Professor

Acknowledgments

I would like to thank Professor Alan H. Epstein for his guidance throughout the course of this project and for the opportunity to work on this challenging project. He gave me his confidence and allowed me to join the "Professors team" working on this project.

I would also like to thank Professor Ian A. Waitz who took time to share with me his views on the combustor design.

Special thanks to Stuart Jacobson who gave me his support, his attention and devoted a lot of time to me. His advices were very helpful in the critical steps of the micro-engine design and his critics helped me improving this report.

Many thanks to Richard Walker who provided many references which I used for the gas bearing design.

I would also like to thank Ismail Ceyhan for introducing me to the secrets of heat exchangers and for giving me lots of practical and helpful advices.

Many thanks to Diana who helped me with the illustrations.

My stay here was made possible by the French Délégation Générale pour l'Armement. I wish to thank them, especially the Direction du Centre d'Essais des Propulseurs, for making this possible.

But most of all, I wish to address my warmest thanks to my wife Catherine for her love, her support, her patience and her comprehensiveness. Without her, this would have never been possible.

Finally, I would like to thank my whole family for its interest and its supports, even far away from here.

Contents

List of Figures

List of Tables

Nomenclature

A	Area (m^2)
c_p	Specific heat $(J.kg^{-1}.K^{-1})$
C_i	Flow-stream capacity rate of side i $(\dot{m}.c_p)$ $(J.s^{-1}.K^{-1})$
C	Bearing clearance (m)
D	Diffusion factor
D	Diameter (m)
D_h	Hydraulic diameter $(\frac{4 * cross\ sectional\ area}{wetted\ perimeter})$ (m)
ECV	Effective Caloric Value $(J.kg^{-1})$
f	Friction coefficient
f	Fuel-to-air mass flow ratio
g	Gravity constant $(9.8\ m.s^{-2})$
h	Heat-transfer coefficient or convection conductance $(W.m^{-2}.K^{-1})$
h	Specific enthalpy $(J.kg^{-1})$
h	Blade height (m)
k	Thermal conductivity $(W.m^{-1}.K^{-1})$
K	Bearing stiffness $(N.m^{-1})$
$\bar{K}$	Stiffness parameter
L_{hy}	Hydrodynamic entrance length (m)
L_{th}	Thermal entry length (m)
$\dot{m}$	Massflow rate $(kg.s^{-1}$ or $g.h^{-1})$
M	Mach number
$\dot{N}$	Mole flow rate $(mol.s^{-1})$

NTU	Number of transfer units $(\frac{U\ A_w}{C_{min}})$
Nu	Nusselt number $(\frac{h.D_h}{k})$
P	Power (W)
P_{out}	Shaft power (W)
P	Static pressure (Pa)
P_a	Ambient pressure (Pa)
P_t	Total pressure (Pa)
Pr	Prandtl number $(\frac{\mu c_p}{k})$
$PSFC$	Power specific fuel consumption $(\frac{\dot{m}_f}{P_{out}})$ $(kg.W^{-1}.h^{-1})$
$\dot{q}$	Heat transfer rate $(J.s^{-1})$
$\dot{q}''$	Heat-flux or heat-transfer rate per unit area, at surface or phase interface $(J.s^{-1}.m^{-2})$
r	Gas constant $(287\ J.kg^{-1}.K^{-1})$
R	Radius (m)
R	Stage reaction rate
Re	Reynolds number $(\frac{\rho V\ D_h}{\mu})$
St	Stanton number $(\frac{h}{\rho V\ c_p})$
t	Thickness (m)
T	Friction torque $(N.m)$
T	Static temperature (K)
T_t	Total temperature (K)
U	Overall thermal conductance $(W.m^{-2}.K^{-1})$
V	Velocity $(m.s^{-1})$
v	Tangential velocity $(m.s^{-1})$
β	Velocity angle with radial direction $(^\circ)$
ϵ	Heat exchanger effectiveness
η	Isentropic component efficiency
Φ	Equivalence ratio $(\frac{f}{f_{stoichio}})$

γ	Isentropic exponent
Λ	Bearing compressibility number
μ	Viscosity of the gas ($N.s.m^{-2}$)
ν	Poisson's ratio
ω	Rotational speed ($rad.s^{-1}$ or rpm)
π	Pressure ratio
Ψ	Specific entropy ($J.kg^{-1}.K^{-1}$)
ρ	Density ($kg.m^{-3}$)
σ	Solidity ($\frac{chord}{spacing}$)
σ	Stress (Pa)
Θ	Correction term

Subscripts

BE	Break-even
$. c$	Compressor
c	Cold flow
f	Fuel
h	Hot flow
H	Constant heat transfer
in	Inlet
m	Mean value
max	Maximum value
min	Minimum value
out	Outlet
r	Radial
t	Turbine
t	Tangential

tf	Transfer
w	Wall

For the engine cycle

2	Compressor inlet
3	Compressor exit, combustor inlet
4	Combustor exit, turbine inlet
5	Turbine exit

For the compressor design

b	Rotor inlet
c	Rotor exit and stator inlet
d	Stator exit

For the turbine design

a	Stator inlet
b	Stator exit and rotor inlet
c	Rotor exit

Superscripts

$'$	Relative frame
$\cdot$	$\frac{d}{dt}$

Chapter 1

Introduction

1.1 Micro-Gas Turbine Concept

The gas turbine engine is the most compact controlled power source that mankind has developed. It is a complex and expensive device and only large scale engines are currently being used. However, the development of micromachining technology suggests that it would be possible to build $1cm^3$ gas turbine engines. Indeed, a $100\mu m$ diameter electrical micromotor has been successfully developed [18], thus opening the road to micro-mechanical devices. With an estimated power output of a few tens of watts, a micro-gas turbine would represent a power density ten times better than the best current batteries. Thus, this concept would be a real breakthrough in small scale power generation.

The enabling technology is microfabrication, for it can satisfy the main requirements for a good gas turbine cycle. First of all, tight tolerances are necessary to avoid parasitic leakage losses. Micromachining deals routinely with precisions as high as 1 part in 2000 and this should be sufficient for limiting these losses. The second key to high power density is high turbine inlet temperatures. In large scale engines, turbine blade cooling and burned gases dilution make them possible. However, this cannot be implemented at micro-scale. Micromachining may be extendable from silicon to silicon carbide, whose properties are appropriate for micro-gas turbine application.

This material can stand temperatures as high as $1600K$, thus making component with low efficiencies still viable. In addition, this material's high strength would allow high rotational speeds which are necessary for high compressor pressure ratios.

The load bearing at these high rotational speeds could be provided by gas bearings. Indeed, they have already been implemented at microscale in gyroscopes and accelerometers. Thus, self-acting gas bearings supplied with part of the compressed air could satisfy the load capability requirements.

This suggests that micro-gas turbine engines are feasible. However, many challenges still remain [3], such as:

- low Reynolds numbers which imply high viscous losses;
- very low combustor residence time;
- micromachining geometry constraints: 3-D shapes routinely used in large engines are not possible with microfabrication process;
- microfabrication of refractory ceramics is still not established.

1.2 Baseline Design

Reference [3] suggested a baseline design obtained by scaling down the $100mm$ diameter rotor automative gas turbines developed by Allied Signal [1] and Allison Gas Turbines [2] for a NASA/DOE-sponsored project. Figure 1-1 gives the conceptual layout of a $1mm^2$ intake area engine [3]. A centrifugal compressor and a radial inflow turbine have been selected. A pressure ratio of 5:1 and a turbine inlet temperature in the $1400K$-$1600K$ range are proposed for cycle design, imposing a rotor tip tangential Mach number of 1.4 and a rotational speed of approximately $3 * 10^6 rpm$.

1.3 Possible Applications

The micro-gas turbine could find many applications in different fields. They are precisely identified in [3] and are summarized briefly below:

- Power generator: coupled to an electric generator, it could replace batteries, providing a 10 times greater power density than the best current batteries.
- Model market: it could spin propellers for hobbyists mini-engine use.
- Boundary layer control: the micro-gas turbine intake could suck off the boundary layer at critical points on aircrafts.
- Mini-refrigerator: coupled to a compressor/expander refrigeration cycle, it could work as a mini-refrigerator.
- Propulsion: micro-engines could be used as modular propulsion system for any aircraft size.

1.4 Thesis Overview

The present work presents the preliminary design study of a micro-gas turbine. Chapter 2 focuses on the thermodynamic cycle and details the interplay between component characteristics. Chapter 3 evaluates gas bearings as candidate for microengine application. Chapter 4 presents a microrecuperator design and estimates actual levels of performance. Chapters 5 and 6 then compile these results, optimize the cycle and propose an engine design corresponding to it.

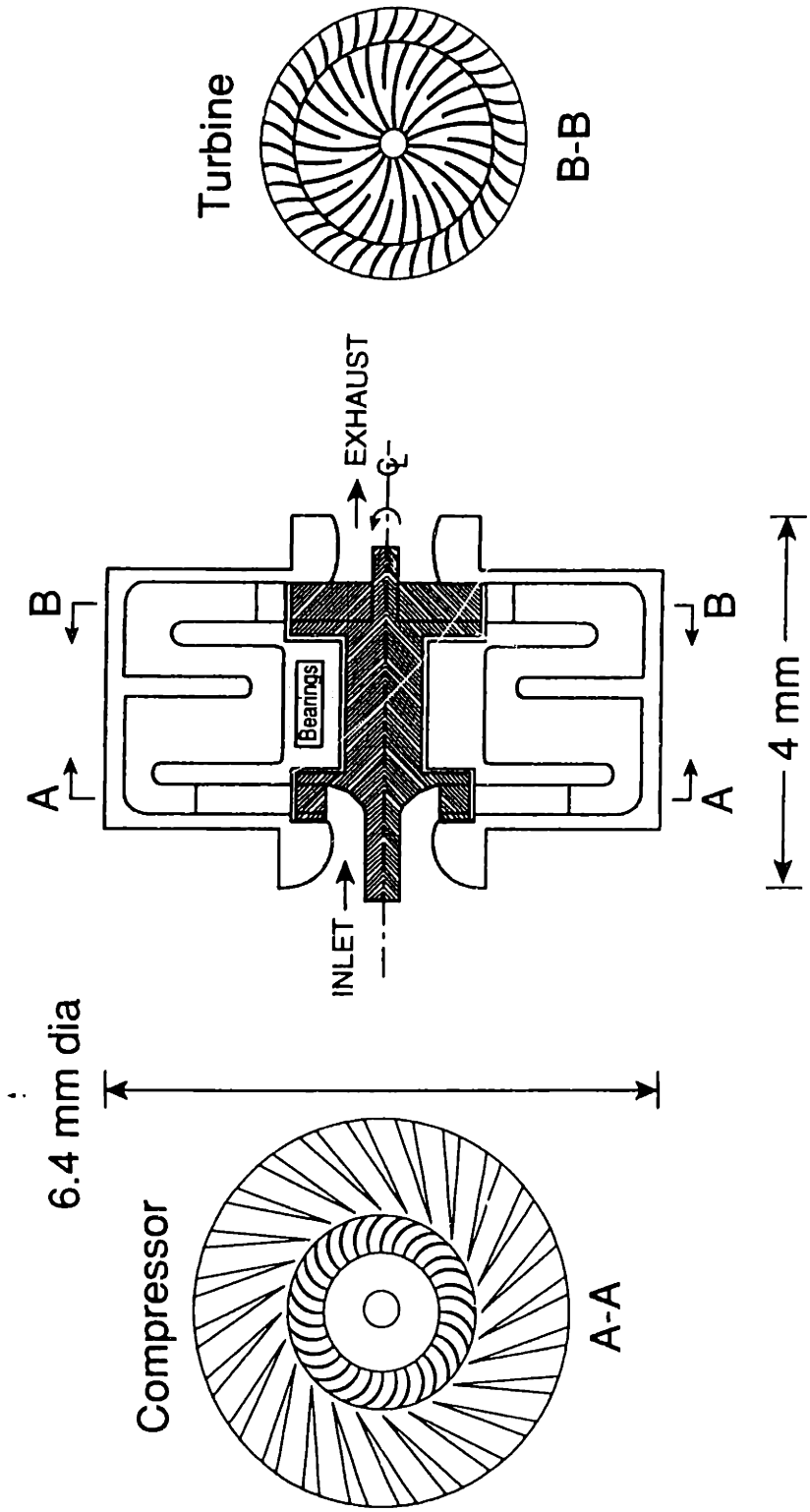

Figure 1-1: Conceptual layout of a micro-gas turbine engine. The inlet flow area is $1mm^2$. The hatched area is the rotor (from reference [3]).

Chapter 2

Parametric Engine Cycle Analysis

2.1 Introduction

Gas turbines are heat engines, in which thermal energy derived from the combustion of fuel with air is converted to useful work. Figure 2-1 represents a basic gas turbine cycle. The compressor raises the temperature and pressure of the incoming air. This air is then mixed with fuel and burned in the combustion chamber. The flow is expanded through the turbine where the thermal energy is converted into shaft power. Part of this power drives the compressor. The excess can be converted to useful work. The exhaust gases are typically hotter than the compressor discharge and can be used to increase the enthalpy of the gas at the combustor inlet, as shown in Figure 2-2.

This chapter explores the thermodynamic cycle considerations of a micro-gas turbine engine. The starting point is the baseline cycle described in Chapter 1 and the fuel considered is conventional jet fuel (Jet A). The specific concern here is the interplay between combustor exit temperature (CET) or T_{t4}, the highest bulk temperature in the engine, and turbomachinery (compressor and turbine) component efficiencies. These are expected to be a limiting factor for microengines and were thus selected for study.

The combustor exit temperature, together with the compressor pressure ratio, sets the cycle specific power (power per unit airflow) which should be as large as possible

to minimize engine size and compensate for component inefficiencies. However, this is the peak temperature in the cycle and is therefore constrained by material capabilities (or, alternately, it sets the requirements for the materials).

Achieving high compressor and turbine efficiencies is expected to be one of the greatest challenges in micro-gas turbine engineering. The primary reason is the increasing importance of viscous forces in the fluid as the physical scale of the device is reduced. Thus, we would expect the component efficiencies to be reduced over those which can be achieved in conventionally sized compressors and turbines.

One convenient measure of the interaction between component efficiencies and CET is the break-even point, the values at which the turbine produces just enough power to drive the compressor with zero net power output from the engine. To first order, additional gains in efficiency or increases in combustor temperature beyond this point will appear as increases in engine output power. Thus, cycle break-even was a central point of this study.

The second focus was an examination of the role of cycle recuperation on microengine performance and break-even and a comparison with the non-recuperated cycle. Recuperation refers to extracting thermal energy from the turbine exhaust and transferring it to the compressor discharge fluid with a heat exchanger in order to reduce the fuel flow required for a given power output. The recuperator effectiveness is a strong function of the cycle parameters and details.

The tool used for this investigation was a gas turbine cycle deck (one-dimensional, lumped parameter, thermodynamic model) known as NPAS, supplied by the NASA Lewis Research Center.

2.2 Cycle Break-Even

Many parameters in an engine influence the break-even point. Here, the compressor isentropic efficiency ($\eta_c = \frac{\text{Ideal work of compression for a given } \pi_c}{\text{Actual work of compression for a given } \pi_c}$) has been chosen as a main parameter. Thus, break-even compressor efficiency is determined for different turbine efficiencies ($\eta_t = \frac{\text{Actual work for a given } \pi_t}{\text{Ideal work for a given } \pi_t}$), combustor exit temperature

Combustor Exit Temp T_{t4} (K)	Heat Exchanger		Comp. & Turb. Eff., $\eta_c = \eta_t$	Fuel Flow (Jet A) $\dot{m}_f$ (g/h)
	$\Delta P/P$	ϵ		
1500	–	–	0.533	17.28
	0	1	0.539	5.13
	0.1	1	0.572	4.85
	0	0.75	0.538	8.30
	0.1	0.75	0.57	8.16
	0	0.5	0.536	11.39
	0.1	0.5	0.568	11.39
1600	–	–	0.515	19.32
	0	1	0.522	5.35
	0.1	1	0.553	5.03
	0	0.75	0.520	8.98
	0.1	0.75	0.551	8.85
	0	0.5	0.518	12.52
	0.1	0.5	0.549	12.56

Table 2.1: Break-even compressor/turbine adiabatic efficiency and fuel flow at design point ($\pi_c = 5$, $\dot{m}_{air} = 1.8 * 10^{-4}\ kg/s$, $\omega = 3 * 10^6\ rpm$). - indicates a non-recuperated cycle.

(T_{t4}), and heat exchanger effectiveness ($\epsilon = \frac{\text{Actual heat transfer rate}}{\text{Maximum heat transfer rate}}$) and pressure drops ($\Delta P/P$). Standard pressure and temperature have been assumed at the inlet. The airflow has then been set to $1.8 * 10^{-4} kg/s$ which corresponds to the inlet air passing through a $1mm^2$ intake area at Mach $M = 0.5$.

To begin with, the turbine efficiency was assumed equal to that of the compressor to simplify analysis. Results are summarized in Table 2.1 and Figure 2-3. For comparison, large scale radial compressor isentropic efficiencies are of the order of 0.85.

These calculations show that:

- The compressor/turbine break-even efficiency decreases when the turbine inlet temperature increases, as expected.
- For $T_{t4} = 1500K$, the break-even efficiency is between 0.53 and 0.57.
- For $T_{t4} = 1600K$, the break-even efficiency is between 0.51 and 0.55.

- The required fuel flow increases as the heat exchanger effectiveness decreases. Without a heat exchanger, the fuel flow is of the order of $18g/h$. With a heat exchanger of high effectiveness, the fuel flow is reduced to $5g/h$.

- The recuperated cycle requires a slightly higher compressor/turbine efficiency for break-even than the non-recuperated one, even when the heat exchanger has no pressure drop and very high effectiveness. However, the recuperator reduces the fuel consumption considerably.

- The lower the heat exchanger effectiveness, the lower the break-even component efficiencies, but the higher the fuel flow.

- The higher the heat exchanger pressure drop, the higher the break-even efficiency, although the fuel flow remains about the same.

2.3 Compressor Break-Even Efficiency as a Function of Turbine Efficiency and Other Variables

The preliminary analysis of the previous section assumed equal compressor and turbine efficiencies. Microscale components have never been studied nor implemented before, therefore the achievable efficiencies are not known. In particular, since the Reynolds number is very low ($\approx$ 1000) at this length scale, low efficiencies are expected, especially for the compressor. However, because of the turbine higher inlet pressure and favorable pressure gradients, the turbine efficiency may be higher than that of the compressor.

Therefore, the turbine efficiency was varied between 0.6 and 0.8 to establish break-even levels. Results are represented in Figures 2-4 to 2-6. From these calculations we conclude that:

- The break-even compressor efficiency drops as turbine efficiency increases.

- An increase of turbine inlet temperature from 1500 to 1600K allows a drop in compressor efficiency of approximately 0.04, for fixed turbine efficiency (Figure 2-4).

- As previously observed, a slightly higher compressor efficiency is required from an engine with heat-exchanger, even with no pressure drop and 100% effectiveness, than from an engine without a recuperator (Figure 2-4).

- The pressure drop in the heat exchanger increases the minimum compressor efficiency necessary for break-even (Figure 2-4).

- The heat exchanger effectiveness has only a small influence on the compressor efficiency at break-even (Figure 2-5).

- As previously observed, introducing a heat exchanger results in a dramatic drop in fuel consumption. Indeed, the engine requires a fuel flow of approximately $6g/h$ with recuperation in comparison to the $16g/h$ without it (Figure 2-6).

- Without recuperation, the engine needs less fuel when the turbine efficiency increases. With a recuperator, the fuel consumption increases with the turbine efficiency (Figure 2-6). This is expected since the turbine exit temperature decreases as the turbine efficiency increases. Thus, the ability of the recuperator to raise the combustor inlet temperature is reduced.

- The fuel consumption increases with the turbine inlet temperature.

- A drop in the heat exchanger effectiveness increases dramatically the fuel consumption. Similarly, a smaller pressure drop (smaller $\Delta P/P$) increases the fuel flow.

2.4 Influence of Compressor Pressure Ratio on the Efficiency at Break-Even

At first, it may be difficult to build the micro-gas turbine with pressure ratios (π_c) as high as 5. Therefore, we studied the correlation between compressor pressure ratio and efficiency. The following calculations consider pressure ratios between 2 and 5 and turbine efficiencies between 0.6 and 0.8 at two turbine inlet temperatures: 1500 and $1600K$. Only the configuration without a heat exchanger was examined.

The results are shown in Figure 2-7 and can be summarized as:

- A reduction in the compressor pressure ratio results in a decrease of the break-even compressor efficiency.
- As before, a higher turbine inlet temperature reduces the break-even compressor efficiency.
- The higher the turbine efficiency, the lower that needed for the compressor.
- For low compressor pressure ratios, it is possible to run the engine at break-even with very low compressor efficiencies. For instance, for $\pi_c = 3$ and $\eta_t = 0.7$, the compressor efficiency can be as low as $\eta_c = 0.33$ for a turbine inlet temperature of $T_{t4} = 1600K$.

2.5 Conclusion

This parametric analysis has examined the relationship between the main cycle parameters for a micro-gas turbine at a break-even (zero net power output) operating point. It must be emphasized that no attempt has been made yet to optimize the cycle parameters about a given combustor exit temperature or compressor characteristic. Only the break-even compressor efficiency has been examined as a function of the turbine efficiency, combustor exit temperature, compressor pressure ratios, and heat exchanger characteristics.

The low efficiencies necessary for break-even seem achievable even at very low Reynolds number and suggest that it would be possible to operate a gas turbine at microscale. These efficiency levels can still be reduced by using higher combustor exit temperatures and lower compressor pressure ratios.

Introducing a recuperator in the cycle appears to be an effective way of reducing the fuel consumption. Therefore, this option should be considered in the micro-engine deisgn, even if the required compressor and turbine efficiencies are higher.

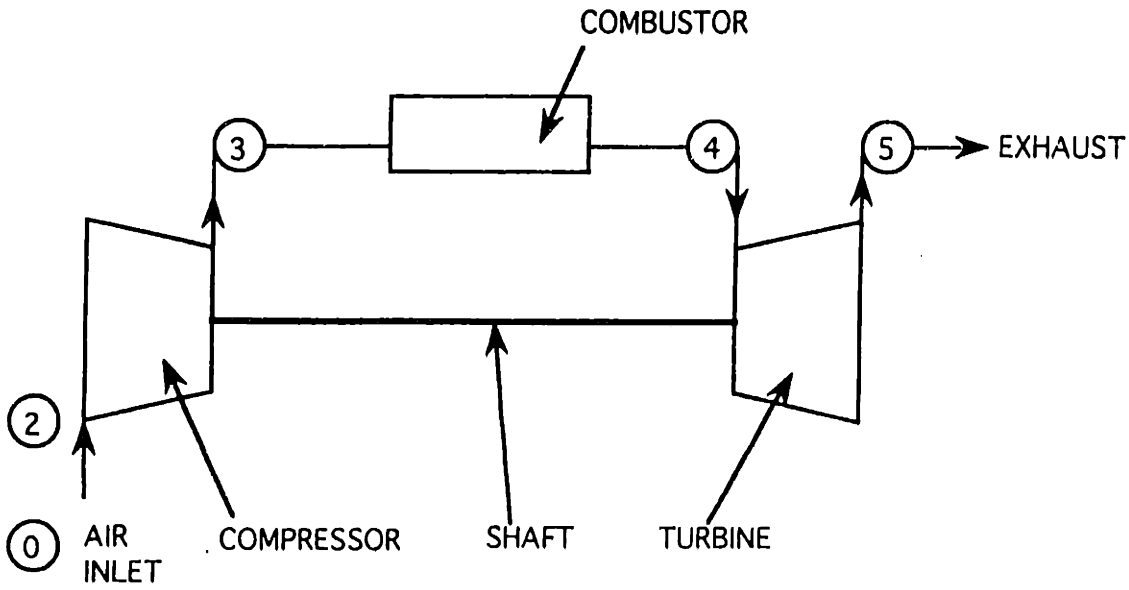

Figure 2-1: Diagram of a basic gas turbine cycle with station numbers.

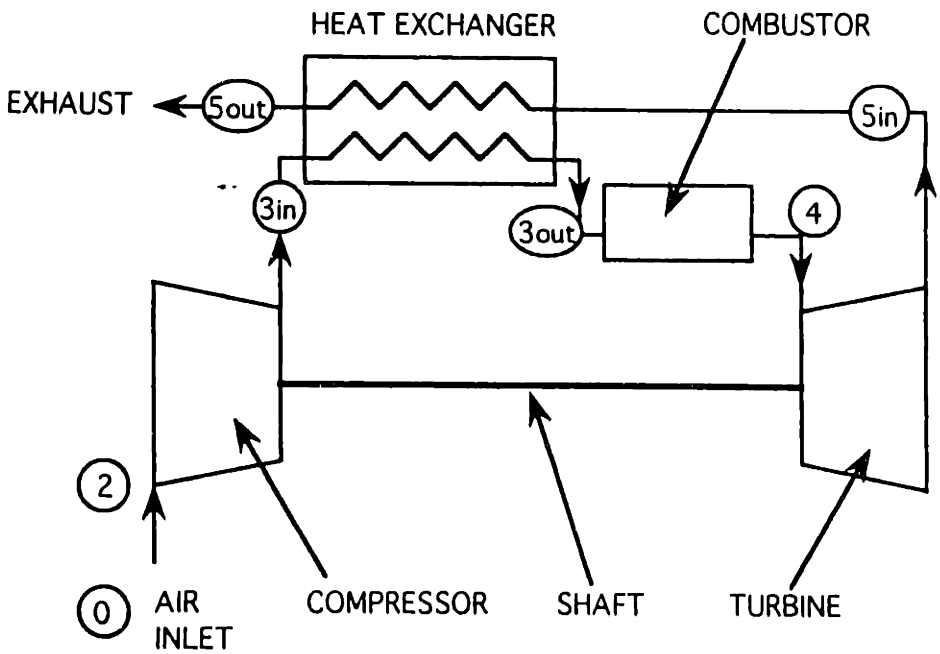

Figure 2-2: Diagram of a gas turbine cycle including a heat exchanger.

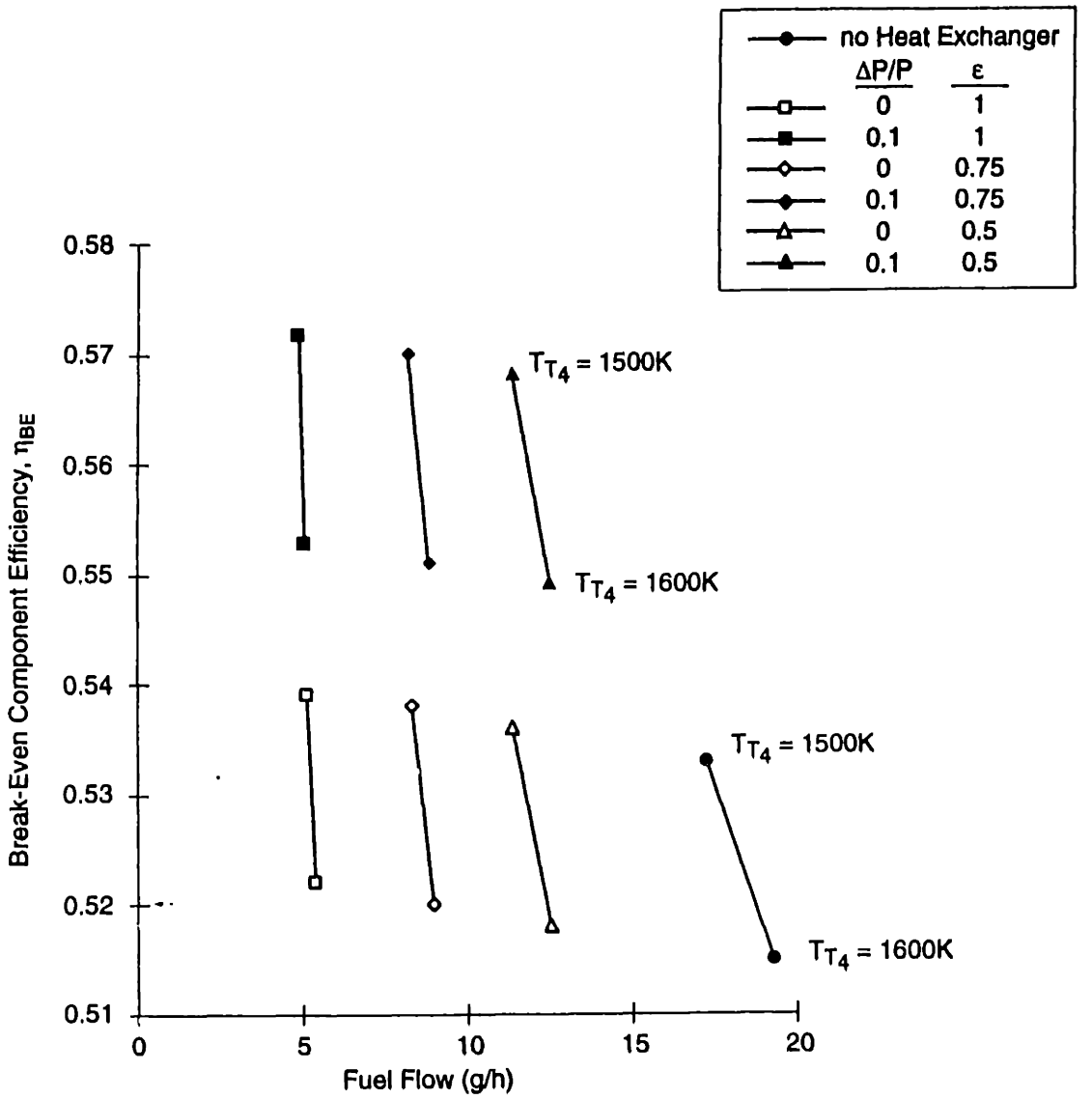

Figure 2-3: Break-even compressor/turbine isentropic efficiency (η_{BE}) and fuel flow at design point ($\pi_c = 5$) for a microengine with a $1mm^2$ intake area.

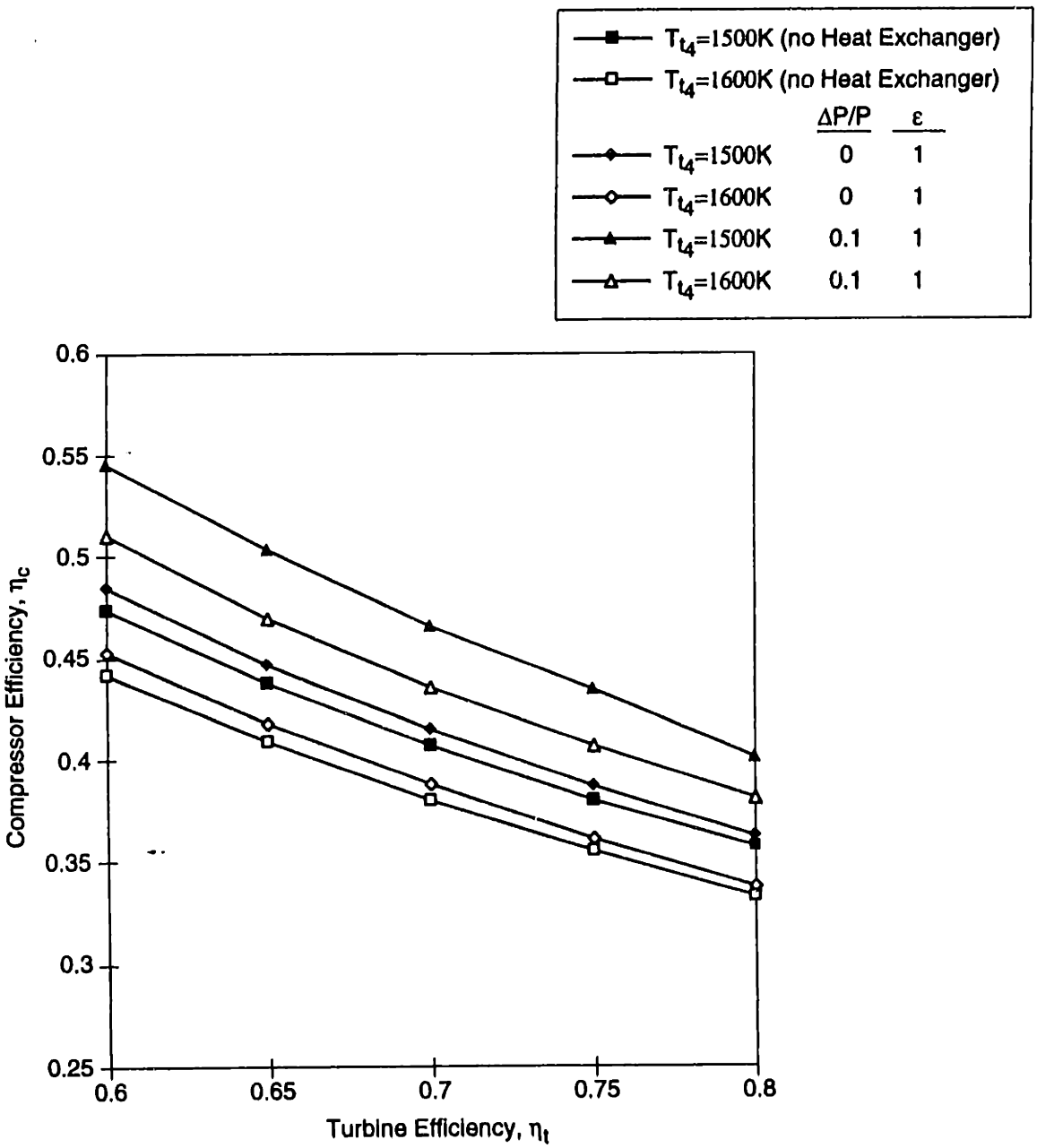

Figure 2-4: Tradeoff between break-even compressor and turbine isentropic efficiency as a function of heat exchanger pressure drop ($\Delta P/P$) and effectiveness (ϵ).

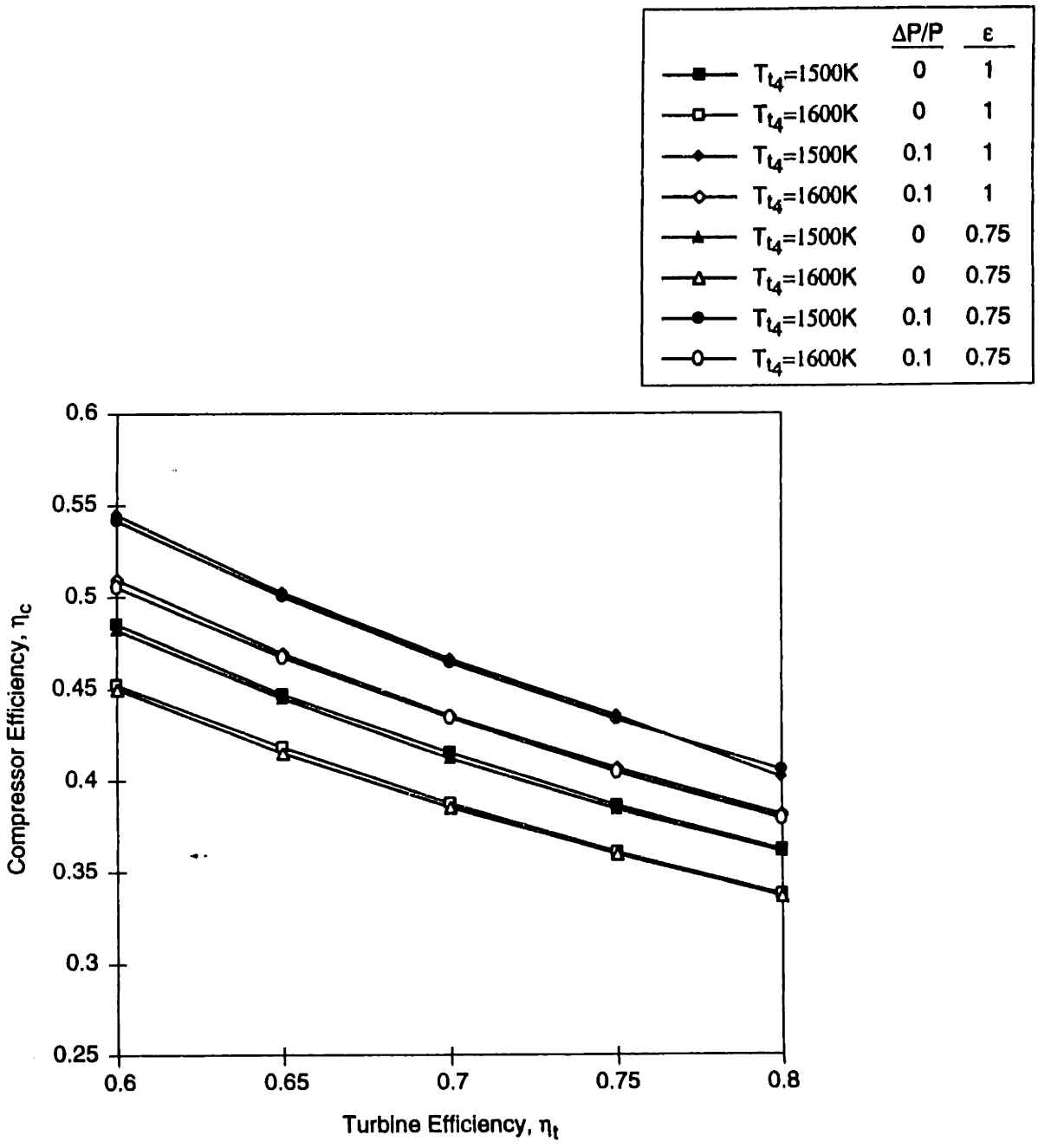

Figure 2-5: The influence of heat exchanger effectiveness (ϵ) on compressor and turbine efficiencies needed for cycle break-even.

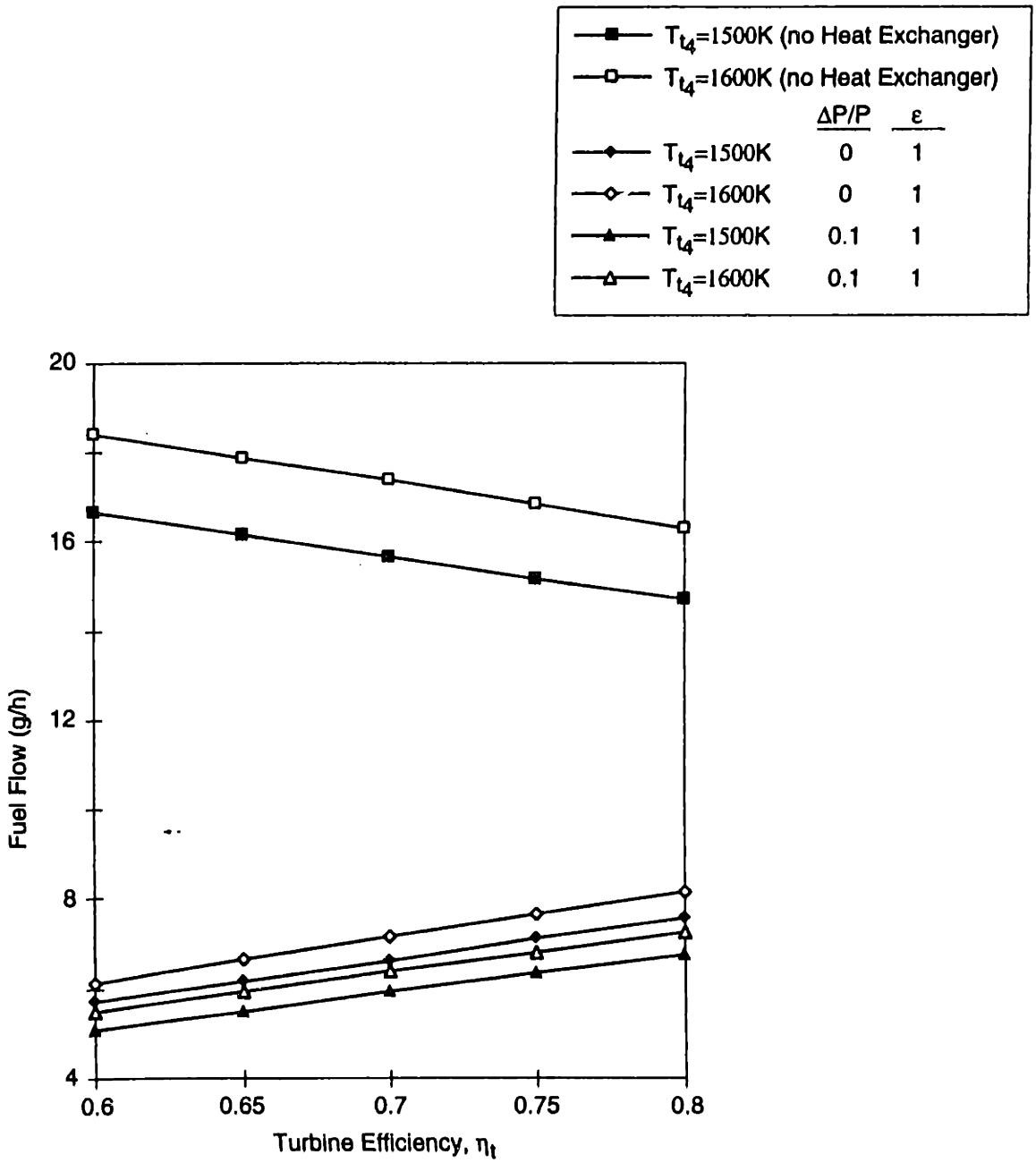

Figure 2-6: Fuel consumption at break-even for a $1mm^2$ intake area microengine.

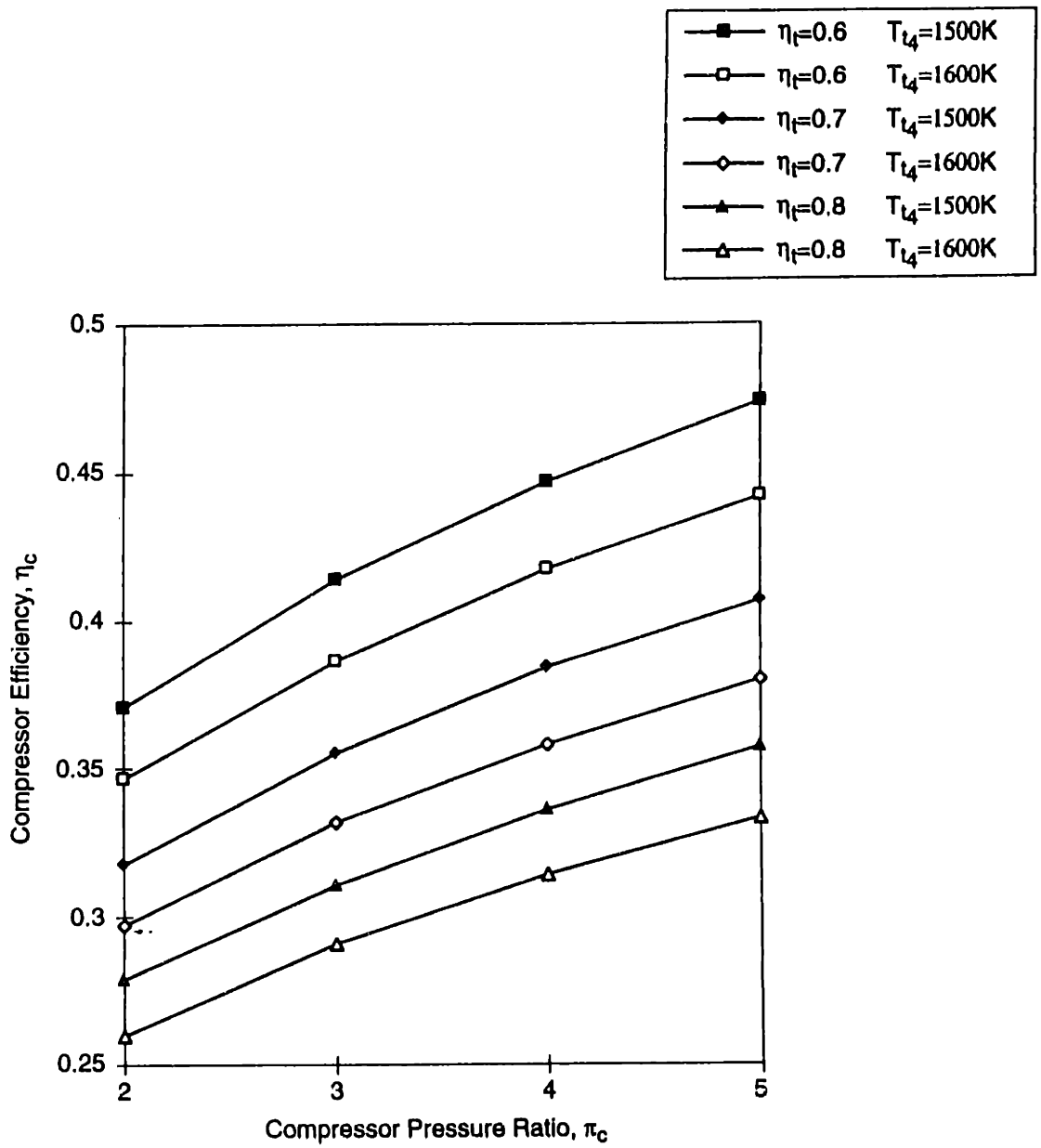

Figure 2-7: The influence of compressor pressure ratio on cycle break-even efficiency as a function of turbine efficiency (η_t) and CET (T_{t4}).

Chapter 3

Gas Bearings

3.1 Introduction

High speed rotating machinery imposes several critical design requirements on bearings, including:

- axial and radial load carrying capability;
- stiffness and damping to control the rotor dynamics;
- clearances between rotating and stationary parts;
- small friction losses; and
- operation in the engine high temperature environment.

For microengines, gas bearings appear to be an interesting solution, since they offer the potential of meeting the design requirements and being compatible with microfabrication techniques. Gas bearings have been implemented for gyroscopes and accelerometers and thus have been built at relatively small scale, which is essential for their use in microengines. Moreover, they exhibit high axial and radial load capability, have low clearances (in the order of $1\mu m$), and low friction losses.

This chapter provides a first order estimate of gas bearing performance as applied to micro-gas turbines. It presents a brief review of gas bearing principles and then applies a simple, empirically based, analysis to the dimensional regions of interest.

3.2 Gas Bearing Principles and Theory

Small scale gas bearings have been widely studied for application to gyroscopes and accelerometers. Reference [12] summarizes the results in this field, giving a theoretical approach and a comparison with experiments.

Gas bearings are similar in some ways to conventional oil journal bearings in that they use the viscosity of the fluid squeezed between the shaft and the sleeve to carry the load. When a gas is sandwiched between two surfaces, it exhibits a resistance to being extruded so that the surfaces are maintained apart for a short time. This effect is the so-called "fluid cushion" [4]. In order to maintain load capability, the interspace in the bearing must be supplied with gas. Typically the shaft is spiral grooved for this purpose and such bearings are called self-acting, or hydrodynamic.

On the one hand, the rotation of the shaft creates a circumferential flow around the bearing due to the viscosity of the gas. On the other hand, the spiral groove leads the gas inwards, so that the molecules which have not joined the primary flow are impelled toward the groove end. Thus, the density is higher at this end, creating a "superambient pressure" [12]. The force appearing between the shaft and the sleeve corresponds to the superambient pressure integrated over the area. This force increases with decreasing film thickness. The ratio of the change in force to the change in film thickness is the stiffness of the bearing.

Three bearing configurations have been developed:

- spool bearing (see Figure 3-1)
- cone bearing (see Figure 3-2)
- hemisphere bearing (see Figure 3-3).

The latter is the most studied in reference [12] and seems attractive, even if it does not have the highest stiffness. It is relatively easy to manufacture in macroscale, there is no problem of alignment and the radial and axial stiffnesses are quite insensitive to axial clearance [13]. Since information on the hemisphere bearings was most readily available, we considered them first for the micro-gas turbine application

3.2.1 Design Constraints

Gas bearings must be designed for the specified axial and radial loads. They are also subject to other forces however, including compliance torques that result from aniso-elasticity and eccentricity of the shaft in the sleeve. These are side effects that one usually tries to avoid.

Aniso-compliance torque is due to the stiffness difference between the axial and the radial directions. Because of this aniso-elasticity, the rotor moves in a direction which is not parallel to the applied force. Then, the orthogonal displacement results in an imbalance torque.

Cross-compliance torque appears when the shaft climbs up in the sleeve, for instance in a plain ungrooved journal bearing. The displacement of the shaft is characterized by the angle between the direction of the load and the radius of minimum film line, the attitude angle. This displacement, which is not parallel to the applied force, creates a "cross-compliance" torque.

These torques vanish when the attitude angle is zero and the axial and radial stiffnesses are matched. Optimized bearing grooving can reduce the attitude angle. Isoelasticity is approached when both stiffnesses are high, so that the difference between the axial and radial directions gets relatively small.

Charles Stark Draper Laboratory has developed a procedure to minimize compliance torques [12], the results of which are used here. Thus, the bearings considered in the following sections are optimized for isoelasticity and zero attitude angle.

3.2.2 Theoretical Approach

The most common theory concerning gas bearings, called "infinite groove theory", assumes that no gas leaks from the ends of the bearing. This allows great simplification in the optimization process although the results do not perfectly match experience.

As with any bearing, an important characteristic is its stiffness, which is defined as the ratio of the load carried by the bearing to the displacement this load induces.

This stiffness is given by:

$$K = \bar{K}\frac{P_a \pi R^2}{C}$$

where

$\bar{K}$: stiffness parameter

P_a : ambient pressure

R : shaft radius

C : mean radial clearance between the shaft and sleeve.

$\bar{K}$ is obtained after isoelastic optimization of the bearing. The calculation was made in [12] in the case of a hemispherical gas bearing and the results are given as a function of the compressibility number Λ :

$$\Lambda = \frac{6\mu\omega R^2}{P_a C^2} \tag{3.1}$$

where

μ : viscosity of the gas

ω : shaft rotational speed

This dependence is shown in Figure 3-4.

Then, assuming linearity between load and deflection, the load capability of the bearing is

$$Load = K\ C$$

An approximate theoretical bearing friction loss is also provided by [12]. The viscous friction torque is given by

$$T = 5.341\ \frac{\mu\omega R^4}{C}$$

with all values in SI units. The resulting friction power loss is

$$P_{friction} = T\ \omega$$

3.2.3 Comparison of Theory to Experiments

The above formulas were based on the assumption of an infinite groove so that the results are approximate for realizable designs [12]. Gas bearings for gyroscopes and accelerometers have also been studied. It was observed experimentally that the above analysis largely overestimated the stiffness, but accurately estimated the power loss. Thus, correction coefficients were established for the stiffness, leading to corrections to the load capability.

The theory/test ratios for the stiffness are [12]:

$$r = 1.5 \quad \text{if } 20 < \Lambda < 50$$
$$r = 2 \quad \text{if } 50 < \Lambda$$

These coefficients will lead to a discontinuity in our results since they change for $\Lambda = 50$. No attempt has been made to smooth this discontinuity, since the results are only approximations.

3.3 Microengine Bearing Design

The above relations are now applied to micro gas turbines. The baseline design assumes that the bearings are fed by compressor discharge at $T = 500K$, $P_a = 4.5atm$, $\mu = 27.16\mu N.s/m^2$, and the shaft rotational speed is $\omega = 3 * 10^6 rpm = \pi * 10^5 rad/s$.

This is sufficient information to calculate the bearing load capability and friction power loss as a function of the bearing radius and clearance. The performance of bearings are not known at this scale, and the bearing geometry is not fixed, so a sensitivity analysis with respect to the radius and the clearance was performed. We note that clearances of no more than $0.5\mu m$ are chosen to be consistent with the desired maximum rotor clearances for the compressor and the turbine ($0.5\mu m$).

The calculated theoretical infinite groove load capability is given as a function of radii and clearances in Figure 3-5. Estimated true load capability is then obtained by applying the correction coefficients (Figure 3-6). Load capabilities are expressed

in *gram-g*, so that the shaft acceleration the bearing can stand is obtained in $g's$ by dividing the load by the rotor mass. The theoretical friction power loss is also plotted (Figure 3-7).

The maximum shaft radial acceleration was estimated from the bearing load capability. Here, we assumed that the microengine rotor will be fabricated from silicon carbide or silicon nitride, with a specific gravity of about 2.7. Thus, the mass of the shaft is estimated to be between 10 and $20mg$. Taking $m_{shaft} = 15mg$, the maximum acceleration that the bearing can carry is given in g's by:

$$c = \frac{Load}{m_{shaft}\, g}$$

The results are plotted in Figure 3-8. Here we assumed that each bearing is sized for the total inertia load.

3.4 Discussion

The preliminary design estimates given above indicate that gas bearings are a plausible candidate for micro-jet engine applications. Discussions with C.S. Draper Laboratory personnel reveal that although they have not built bearings at these dimensional parameters ($3 * 10^6 rpm$, 0.015 gram rotor mass), the non-dimensional parameters are within their experience base. Also, $0.5\mu m$ bearing clearances are not new or particularly challenging.

The work done here has been on bearing capability only; we have not considered microengine requirements. Aircraft gas turbine engines typically must withstand $9g$ landing loads as limits with concomitant radial forces. The estimates in Figure 3-8 indicate that operating microengines may be capable of withstanding several thousand g's, compatible with being dropped onto a hard surface from a height of several feet. This favorable scaling may be due to the cubed-square scaling effect. Other related issues which must be explored include axial load capability and rotor dynamics.

To the detail examined to date, gas bearings appear a viable candidate for micro-

gas turbine applications.

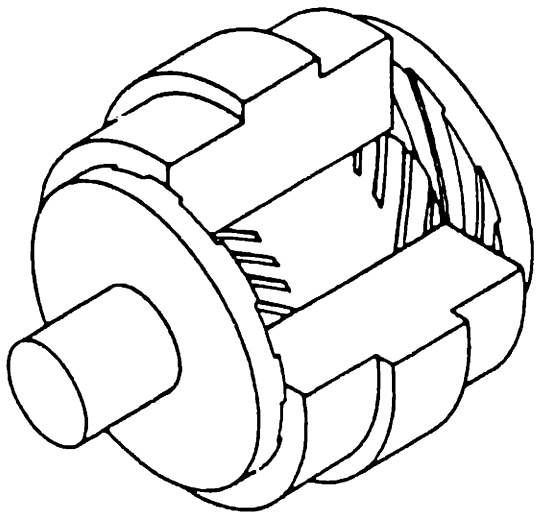

Figure 3-1: Closed spiral-grooved spool gas bearing: one journal bearing and two thrust disc bearings (from reference [12])

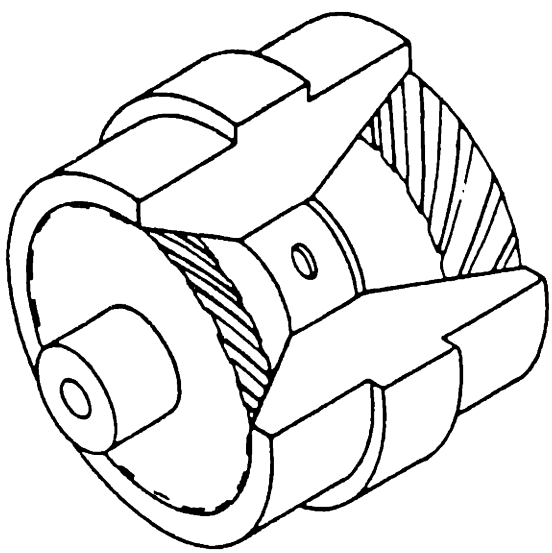

Figure 3-2: Spiral-grooved cone gas bearing (from reference [12])

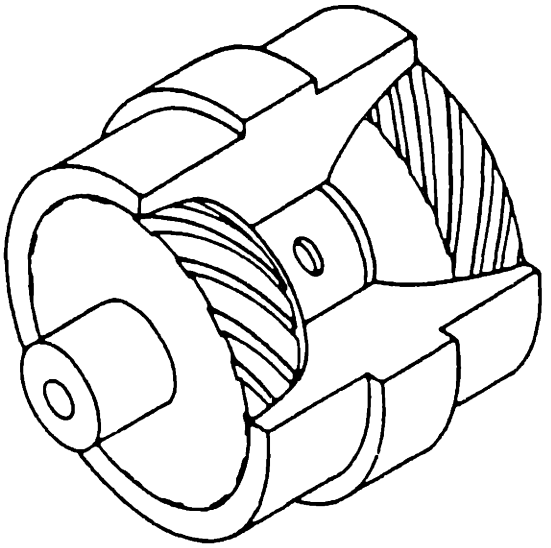

Figure 3-3: Spiral-grooved hemisphere gas bearing (from reference [12])

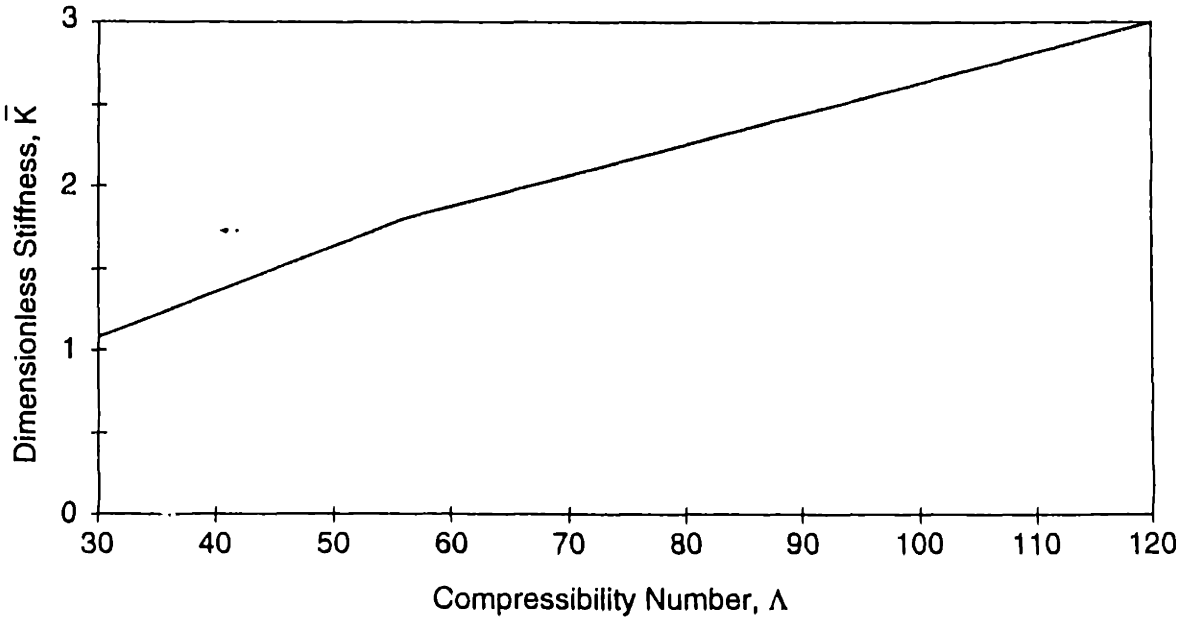

Figure 3-4: Dimensionless stiffness for optimized hemispherical gas bearings as a function of compressibility number, Λ.

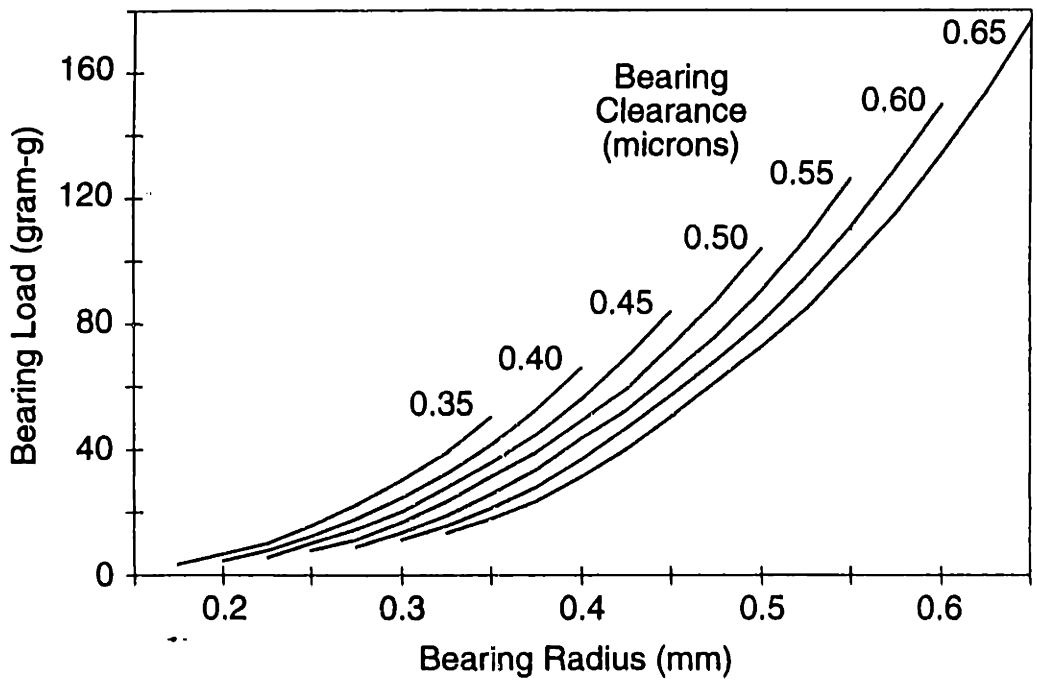

Figure 3-5: Theoretical load capability of an infinite groove hemispherical gas bearing at $3 * 10^6 rpm$, fed with air at $T = 500K$ and $P = 4.5atm$.

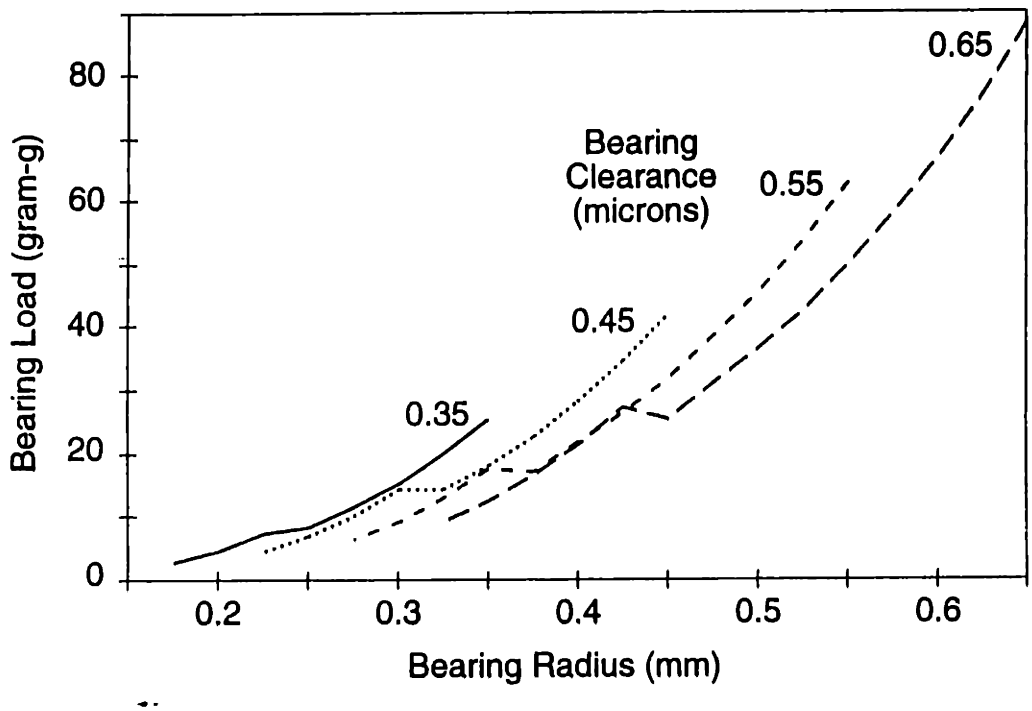

Figure 3-6: Estimated load capability of a finite groove hemispherical gas bearing at $3 * 10^6 rpm$, fed with air at $T = 500K$ and $P = 4.5atm$.

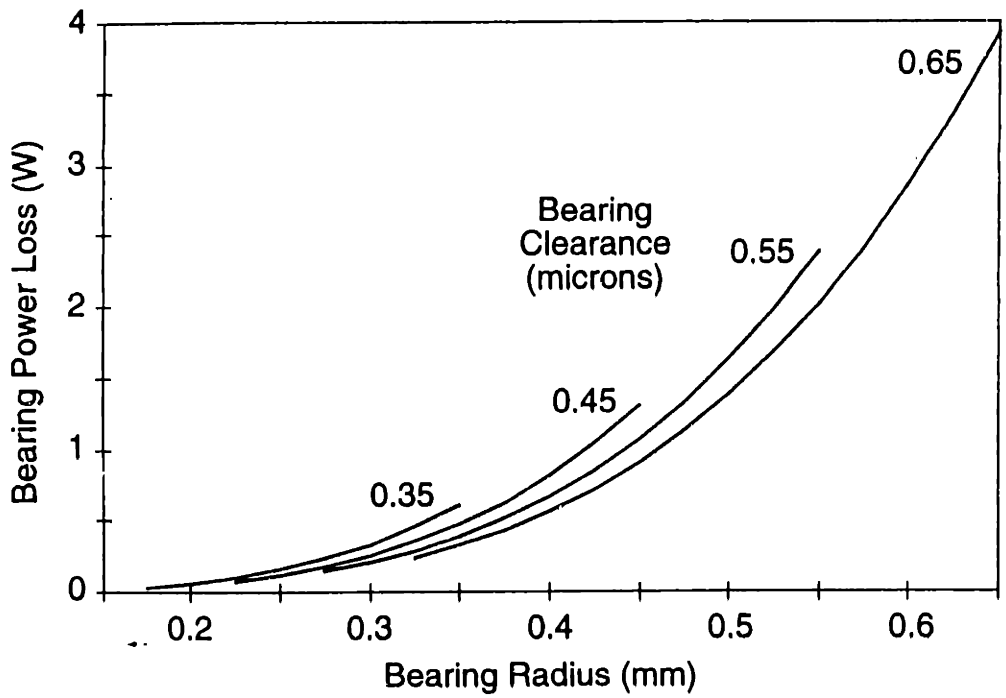

Figure 3-7: Friction power loss of a hemispherical gas bearing at $3 * 10^6 rpm$, fed with air at $T = 500K$ and $P = 4.5atm$.

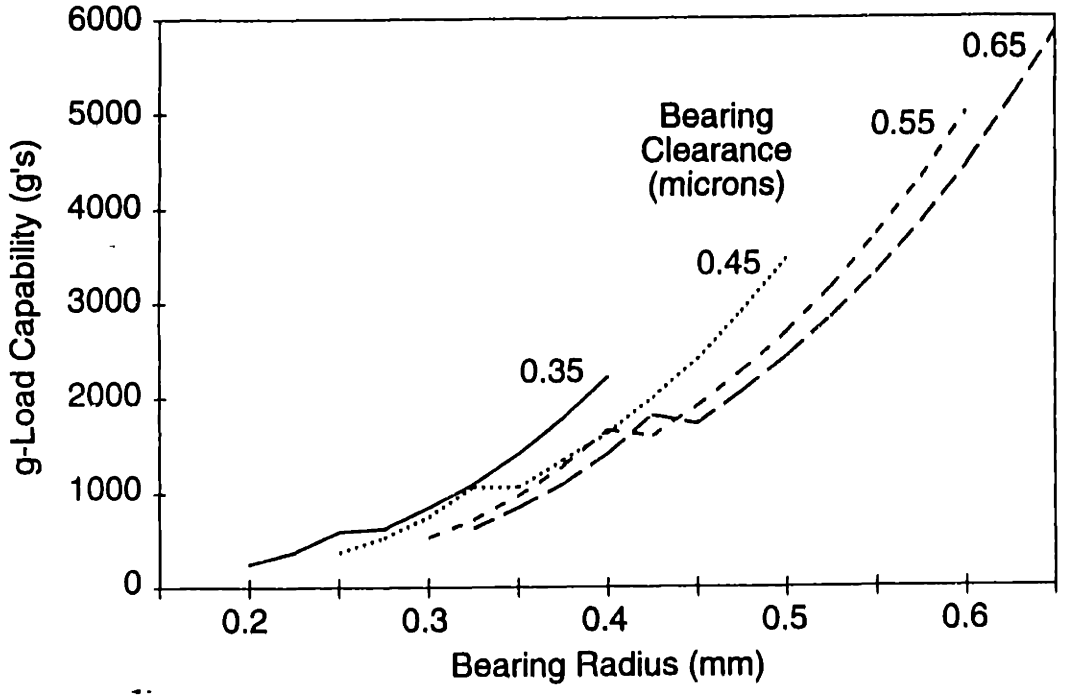

Figure 3-8: g-load capability of a finite groove hemispherical gas bearing at $3*10^6 rpm$, fed with air at $T = 500K$ and $P = 4.5atm$ for a $15mg$ shaft.

Chapter 4

Micro-Recuperator

4.1 Introduction

The parametric cycle analysis described in Chapter 2 has demonstrated the utility of a recuperator for improving the overall cycle. Such a device permits a reduction of fuel consumption for a given power output. For instance, at break-even, a heat exchanger with 100% effectiveness and 10% pressure drop reduces the Jet A fuel flow required from $18g/h$ to $8g/h$.

A recuperator is particularly attractive for the micro-gas turbine for two main reasons:

- the turbine exit temperature is high (relative to the compressor exit temperature) as a consequence of the very high turbine inlet temperature, so that even low heat exchanger effectiveness improves the fuel consumption greatly.

- the limitation on the size and weight of the micro-gas turbine is not so strong as that for conventional aircraft turbine engines.

Therefore, using a recuperator is an option that has to be considered and this chapter estimates to a first order the performance of a micro-recuperator.

4.2 Principle of a Recuperator

A recuperator is a heat exchanger which transfers the otherwise wasted thermal energy from the turbine exhaust to the compressor discharge fluid, thus raising the fluid temperature at the combustor inlet. This decreases the temperature rise in the combustor, allowing for a reduction in the fuel flow required for a given power output. Thus, the heat exchanger considered is of the gas-to-gas type.

Figure 2-2 presents schematically a recuperator integrated in a gas turbine.

4.3 Inlet Conditions

The heat exchanger analysis was performed using typical values from the cycle analysis (see Chapter 2) and air standard inlet conditions ($T_{t2} = 288K$ and $P_{t2} = 1atm$):

$$\begin{aligned} \dot{m} &= 1.8 * 10^{-4} kg/s \\ \pi_c &= 5 \\ T_{t4} &= 1600K \\ P_{out} &= 40W. \end{aligned}$$

The energy balance gives:

$$\begin{aligned} \Rightarrow \quad T_{t3} &= 530K \\ T_{t5} &= 1230K \end{aligned}$$

with $\eta_c = 0.70$ and $\eta_t = 0.82$.

4.4 Heat Exchanger Design Procedure

4.4.1 Conventions and Notations in Heat Exchanger Design

A few preliminary definitions are necessary before dealing with the heat exchanger design.

Flow-Stream Capacity Rate of side i :

$$C_i = \dot{m} c_{pi}$$

where c_{pi} is the specific heat.

Hydraulic Diameter D_h**:** heat exchanger characteristic dimension, used for instance for the Reynolds number Re or the Nusselt number Nu.

$$D_h = 4 \frac{\text{cross sectional area}}{\text{wetted perimeter}}$$

This parameter is introduced for consistency in notation between the different kinds of heat exchanger geometries.

Examples:

- For a tube with circular cross-section of radius r:

$$D_{h,circular} = 4 \frac{\pi r^2}{2\pi r} = 2r.$$

- For a tube with annular cross-section (inner radius r_i, outer radius r_o):

$$D_{h,annular} = 4 \frac{\pi(r_o^2 - r_i^2)}{2\pi(r_o + r_i)} = 2(r_o - r_i).$$

Reynolds Number Re**:** characteristic of the relative importance of inertia and viscous forces.

$$Re = \frac{\rho V D_h}{\mu}$$

Heat-Transfer Coefficient or **Convection Conductance** h: coefficient linking the heat-flux $\dot{q}''_w$ and the temperature difference at a tube wall interface [11]:

$$\dot{q}''_w = h(T_w - T_m)$$

where

T_w is the wall temperature,

T_m is the mixed mean fluid temperature: $T_m = \frac{1}{A_c V} \int_{A_c} u\, T\, dA_c$ (u is the velocity component in the tube axial direction, V is the mean fluid velocity in the tube, A_c is the tube cross-sectional area, T is the local temperature).

Nusselt Number Nu: characteristic of the relative importance of convection conductance and thermal conductivity.

$$Nu = \frac{hD_h}{k}$$

where k : thermal conductivity, $W/(mK)$.

Stanton Number St: alternative non-dimensionalization of the heat-transfer coefficient, showing the relative importance of the convection conductance to the flow thermal capacity:

$$St = \frac{h}{\rho V c_p}.$$

Prandtl Number Pr:

$$Pr = \frac{\mu c_p}{k}$$

If the numerator and denominator are multiplied by density, Pr becomes

$$Pr = \frac{\nu}{\alpha} = \frac{\text{kinematic viscosity}}{\text{thermal diffusivity}}.$$

Thus, the Prandtl number compares the diffusivity of momentum, or velocity, to the diffusivity of heat, or temperature (the diffusivity is the rate at which a particular effect is diffused through the medium).

If Pr is greater than 1, the velocity profile develops more rapidly than the temperature profile. If Pr is less than 1, the temperature profile develops faster. For air at high temperatures, Pr is of the order of 0.7.

Note that

$$Nu = St\ Pr\ Re$$

Heat Exchanger Effectiveness ϵ: this parameter characterizes the level of performance of the heat exchanger. It is defined as [11]:

$$\epsilon = \frac{\dot{q}_{actual}}{\dot{q}_{max\ possible}}.$$

The energy balance gives

$$\dot{q}_{actual} = \dot{m}_c c_c (T_{c,out} - T_{c,in}) = \dot{m}_h c_h (T_{h,in} - T_{h,out})$$

with the definition of the flow stream capacity rate

$$\dot{q}_{actual} = C_c (T_{c,out} - T_{c,in}) = C_h (T_{h,in} - T_{h,out}).$$

The subscripts c and h correspond respectively to the cold and hot flows.

The thermodynamic limit on the maximum heat-transfer rate is achieved when one of the two fluids exits with the entering temperature of the other fluid. If $C_c < C_h$,

$$\dot{q}_{max} = C_c (T_{h,in} - T_{c,in});$$

otherwise

$$\dot{q}_{max} = C_h (T_{h,in} - T_{c,in}).$$

Thus

$$\dot{q}_{max} = C_{min}(T_{h,in} - T_{c,in}).$$

Then the effectiveness is defined as

$$\epsilon = \frac{C_c(T_{c,out} - T_{c,in})}{C_{min}(T_{h,in} - T_{c,in})}$$

or

$$\epsilon = \frac{C_h(T_{h,in} - T_{h,out})}{C_{min}(T_{h,in} - T_{c,in})}.$$

4.4.2 Design Procedure

Figure 4-1 presents the successive steps for designing a heat exchanger.

For a given geometry and imposed inlet conditions, we can determine the hydraulic diameter on each side (cold and hot) and the Reynolds number, which can be used to determine the Nusselt number from tabulated experimental data: $Nu = F(Re, \text{tube shape})$ [10]. The thermal conductivity (k) and D_h then determine h by the definition of the Nusselt number. The overall thermal conductance U is then defined by:

$$\frac{1}{UA_w} = \frac{1}{h_c A_c} + \frac{t}{k_w A_w} + \frac{1}{h_h A_h} \tag{4.1}$$

where

A_c : cold side transfer area

A_h : hot side transfer area

A_w : average wall area, average of A_c and A_h

t : wall thickness

k_w : wall thermal conductivity

Equation (4.1) is true in the case where there is no fin on either side (fins are often used to increase the heat-transfer area).

The number of transfer units $NTU = UA_w/C_{min}$ and the capacity-rate ratio C_{min}/C_{max} give the effectiveness for the configuration considered. Reference [10] presents such correlations for all kind of flow arrangements.

Concerning the pressure drop, the friction factor f is obtained through a formula of the kind $f * Re = K$, where K is a constant depending of the tube shape. The geometry sets the velocities in the different passages, giving access to acceleration pressure losses and dynamic heads, so that the overall pressure drop can be calculated.

4.4.3 Heat Exchanger Configurations

There are many possible flow arrangements, with single or multiple passages [11]. Only the simplest one will be considered here.

- Parallel-flow (see Figure 4-2)

  The effectiveness obtained for this configuration is low for thermodynamic reasons. In the case where $C_c = C_h$, the exit temperatures can only approach a temperature halfway between inlet temperatures, thus limiting the effectiveness to $\epsilon_{max} = 0.5$.

- Counterflow (see Figure 4-3)

  This configuration gives the best effectiveness for a given surface area, since one of the fluids can exit with the inlet temperature of the other fluid. However, the headers geometry has to be more complex, because the two fluids must be somehow separated at the entrance and exit.

- Cross-Flow, both fluids unmixed (see Figures 4-4 and 4-5)

  This is the most common flow arrangement, because of its geometric simplicity. However, the effectiveness is lower than for the counterflow configuration, for a given transfer area.

4.5 Counterflow Heat Exchanger with Concentric Annuli

An interesting flow arrangement is the concentric annular counterflow, with the fluids flowing axially in the tubes. It has a high effectiveness and could be built on the outside of the micro-gas turbine, thus saving space. Here, the inside diameter of the heat exchanger should be no less than the engine outside diameter, which is nominally $6mm$. Figure 4-6 is a sketch with dimensions.

The estimation of the performance of the recuperator is complex and requires the use of empirical correlations which only apply in specific situations. Therefore, some assumptions are necessary for solving this problem. The validity of these assumptions will be checked with the results obtained.

4.5.1 Flow Arrangement Assumptions

The heat exchanger is made of a series of annuli, which are assumed to be **infinite parallel plates**. Indeed, the radius of one annulus is larger than $3mm$ and the height is around $30\mu m$ for the cold flow and around $150\mu m$ for the hot flow. Thus, the tube perimeter and the radius of curvature are a lot larger than the interval between the walls. The assumption of infinite parallel plates is then reasonable.

4.5.2 Heat Transfer Assumptions

A simplification in the case of a counterflow heat exchanger is obtained by assuming that the heat transfer is constant along the tube. Indeed, the flow-stream capacity rates on both sides C_c and C_h are of the same order of magnitude ($C_c/C_h \approx 0.8$) , so that with this configuration, the temperature difference between both sides remains about the same. Thus, the assumption of **constant heat transfer** is not too bad.

The axial conduction should be taken into account since the tubes are short. However, this axial conduction is totally negligible for Péclet numbers $Pe = Re\ Pr = 100$ and is quite small even for $Pe = 10$ [11]. The present situation corresponds to

Péclet numbers higher than $90 * 0.7 \approx 60$, so that **axial heat conduction can be neglected.**

No heat loss has been considered in this analysis. Since the annuli are concentric, the only place where the heat of one side can be transfered to is the fluid on the other side. The only place where a heat loss can occur is at the outside and inside heat exchanger walls. However, this heat loss can be neglected since it occurs only for two annuli compared to the eight of the entire device.

4.5.3 Flow Characteristics Assumptions

The cold and hot flows in the passages are assumed to be **laminar.** They are characterized by very small Reynolds numbers: $Re \approx 50 - 150$.

The flow is assumed to be **thermally and hydrodynamically fully developed:** the nondimensional temperature profile [11] and the velocity profile are invariant along the tube length. In particular, the boundary layers on the inner and outer radii have grown so that they cover the entire height. This assumption allows us to take a constant Nusselt number Nu_m for the entire annulus as well as a constant product $f\ Re$. This approximation is reasonable when the ratio of the length of the tube to the hydraulic diameter is larger than $L_{th,H}/D_h$ and L_{hy}/D_h [20]:

$$L_{th,H}/D_h = 0.0115439 Re Pr$$

$$L_{hy}/D_h = 0.3125 + 0.011 Re$$

where $L_{th,H}$ is the thermal entry length of parallel plates at constant heat transfer and L_{hy} is the hydrodynamic entrance length of parallel plates (with the assumption of a uniform velocity profile at the entrance [20]).

Applying these formula to this case, with $Pr = 0.7$, give

$$L_{th,H}/D_h \approx 1$$

$$L_{hy}/D_h \approx 1 - 2$$

The geometry proposed later on satisfies these conditions since $(L/D_h)_h \approx 15$ and $(L/D_h)_c \approx 50$. If this assumption was not perfectly valid, the effectiveness and the friction factor (and thus the pressure drop) would be underestimated.

The assumptions of infinite parallel plates and constant heat transfer along the tubes are sufficient for determining the main flow parameters. Reference [10] proposes the following values in such a configuration:

$$Nu_{m,H} = 8.325$$

$$f\ Re = 24$$

The subscript m means that the Nusselt number is an average along the tube; H signifies that a constant heat transfer has been assumed.

The heat exchanger consists of many concentric passages so that each has a different radius. Since we keep the same height for all the passages of one side, the cross-sectional areas are not the same and the mass flow rate through them are different. Instead of doing the heat transfer analysis for each set of two annuli (one cold, one hot), we did the calculation only once at the mean radius, thus considering a mean massflow rate. This implies the assumption of **uniform splitting of the flow on one side between all the passages.**

4.5.4 Gas Properties Assumption

In the recuperator, the cold fluid is the compressor exit air at high pressure ($5atm$) and low temperature ($530K$) at the inlet to the heat exchanger.

On the hot side, there are **burned gases** which have somewhat different properties than air. However, the correction coefficient is low (about 2%) in the present situation according to [10] p.301, because the fuel-to-air ratio is small (only a few percent). Thus, the burned gases are assumed to have the **same properties as air** at $1atm$ and $1230K$ at the hot side inlet.

The formula used for the characteristics of air at different temperatures and pressures [5] are given in Appendix A.

4.5.5 Pressure Drop

The pressure drop of the fluid in the heat exchanger passages has several origins: friction, acceleration due to change in temperature, change in passage cross-sectional area.

In the heat exchanger core where heat transfer occurs (see Figure 4-2 for core definition), the friction and acceleration terms can expressed as [10]:

$$\frac{\Delta P}{P_{in}} = \frac{(\rho V^2)}{2P_{in}}[f\frac{A_{tf}}{A_{core}}\frac{\rho_{in}}{\rho_m} + 2(\frac{\rho_{in}}{\rho_{out}} - 1)]$$

They have been neglected everywhere else.

For the pressure drop in the header where the cross-sectional area changes many times, a conservative assumption has been made. The dynamic head loss has been set to 1 for tube expansion and to 1/2 for tube contraction. This means that:

- for an expansion

$$P_{t,out} = P_{t,in} - 1 * (\frac{1}{2}\rho V_{in}^2)$$

- for a contraction

$$P_{t,out} = P_{t,in} - \frac{1}{2}(\frac{1}{2}\rho V_{out}^2)$$

4.5.6 Results

Calculations have been done for several configurations. The free variables that have been used are:

- the number of passages on each side (cold and hot)
- the length of the heat transfer zone (or core)
- the inlet and outlet velocities in the device for each flow

	Cold side	Hot side
# of passages	4	4
height (μm)	31	145
D_h (m)	$6.15 * 10^{-5}$	$2.91 * 10^{-4}$
Re_{D_h}	147	87
h ($W/(m^2.K)$)	5522	2538
T_{in} (K)	528	1229
T_{out} (K)	1063	806
$V_{in,core}$ (m/s)	20	45
$V_{out,core}$ (m/s)	42	30
P_{out}/P_{in}	0.96	0.95
$P_{t,out}/P_{t,in}$	0.96	0.94

$\dot{m}$ (kg/s)	$1.8 * 10^{-4}$
core length (mm)	3
mean radius (mm)	3.5
wall thickness (μm)	10
NTU	2.46
C_{min}/C_{max}	0.791
ϵ	0.76

Table 4.1: Concentric heat exchanger design parameter (see Figure 4-6)

- the inlet velocity in the heat transfer zone for each flow
- the thickness of the walls

These parameters have been varied to arrive at a design for a high effectiveness heat exchanger with low pressure drop.

Some observations detailed in Appendix B seem important to point out before discussing the design results. Very low velocities are necessary in the core in order to limit the pressure drop. There is a trade-off between good effectiveness and low pressure drop. The higher the transfer area, the higher the friction surface and thus the higher the pressure drop. Therefore, a higher number of passages or a longer core amplifies the pressure drop.

The material used here is silicon carbide which has a thermal conductivity $k \approx 100 W/mK$. The selected wall thickness is $10 \mu m$. However, these parameters do not have a large influence on the effectiveness, because t/kA_w is negligible in the expression of the overall conductance UA_w (Equation (4.1)). The annulus height on the hot side is five times larger than that of the cold side. This is due to the large pressure difference (ratio of 5:1) which induces a large density difference between the two flows.

One reasonable configuration appears to be with four passages on each side, with a core length of $3mm$. The effectiveness is then 76% for hot and cold flows static pressure drops of respectively 6% and 5% of the inlet static pressures. This final design is presented in Table 4.1.

4.6 Some Remarks on the Cross-flow Heat Exchanger

As previously explained, the cross-flow heat exchanger is less effective than the counterflow, but the header geometry is simpler. For instance, a section of the heat exchanger could appear as drawn on Figure 4-5. It would also be easier to build a cross-flow device using micromachining by superposing layers with simple geometry.

However, the estimation of the recuperator performances is more complex for cross-flow than for counterflow configurations. The air temperature on one side is changing along one tube and from one tube to another, as illustrated on Figure 4-7. Moreover, at a given section of the tube, the wall temperature is not the same on every face. Thus, no assumption such as constant wall temperature or constant heat transfer is allowed, so that neither Nu nor h can be taken as constant along one tube and from one tube to another. Therefore, no analytical solution is available as is the case with the counterflow arrangement.

Usually, cross-flow heat exchangers are designed by using experimental data books providing information about specific heat transfer surfaces. These surfaces are macrosurfaces with very large fin area and staggered fins. The data are not very helpful in the present case, since laminar flows do not require very large fins which increase the pressure drop by friction but do not improve greatly the effectiveness. Also, scaling is difficult since macrosurfaces are metallic, so that the ratio of wall thickness to tube width is very small. This is in contrast to microsurfaces which would be made of silicon nitride or silicon carbide and would have a larger wall thickness to tube width ratio.

Thus, the classical methods cannot be used in the present case. A solution could be to use a finite element analysis to solve the heat transfer problem by starting with the upper left hand side corner (see Figure 4-7) where the inlet conditions are known. However, heat transfer across square section tubes is complex (there is almost no transfer in the corners) and finite element methods were beyond the scope of this effort. Therefore, this analysis was limited to the counterflow configuration which gives the order of magnitude of the achievable performance. A more precise analysis could be done further in the development of the project if recuperators still appear to be attractive.

4.7 Discussion

This analysis gives an idea of the level of performance achievable for micro-heat exchangers and suggests that effectiveness as high as 75% can be obtained with stagnation pressure drops of the order of 5% of the inlet pressure. However, these results have to be considered with great care for several reasons.

First of all, it is commonly accepted that performance prediction by the method used above has an accuracy of less than 30% [15]. Many assumptions were made, some of them accurate, others only approximate. Also, many relationships are empirical and of limited precision. Thus, the results given here should be considered first estimates.

The counterflow configuration is the most effective, but it requires headers with complex geometry. This issue would have to be considered carefully because of the microfabrication constraints: conventional techniques do not allow complex three dimensional geometries. The length of tubes is also an important parameter since microfabrication can only be applied to limited sizes (a few millimiters). A solution to these geometry and fabrication constraints would be to use a counterflow exchanger similar to the one presented in Figure 4-8. Headers and surfaces would then be a lot simpler to manufacture. However, experimentation would be the only way to accurately determine performance.

The last aspect to consider is the integration of the recuperator with the micro-engine. The piping arrangement between the turbomachinery and the heat exchanger would probably be complex, thus inducing pressure drops, and this has not been taken into account in the present calculations. Further, recuperation greatly increases the combustor inlet temperature. This temperature has to be below that of fuel autoignition in order to insure proper mixing before burning occurs. For hydrogen, the autoignition limit is $858K$, i.e., less than the cold flow exit temperature, so that fuel may burn prematurately. Therefore, high recuperator effectiveness, which gives high burner inlet temperatures, is not necessary desirable. A heat exchanger with a smaller core length could be designed, thus reducing the effectiveness to a level where autoignition problems would be avoided. The resulting reduction of pressure drops would increase the power output and thus the margin above break-even. However, low gas turbine component performances are expected and all parasitic loss sources are not identified yet, so that even low pressure drops caused by recuperation may be too high for closing the cycle. Further development of the project will determine if a recuperator is viable to the cycle.

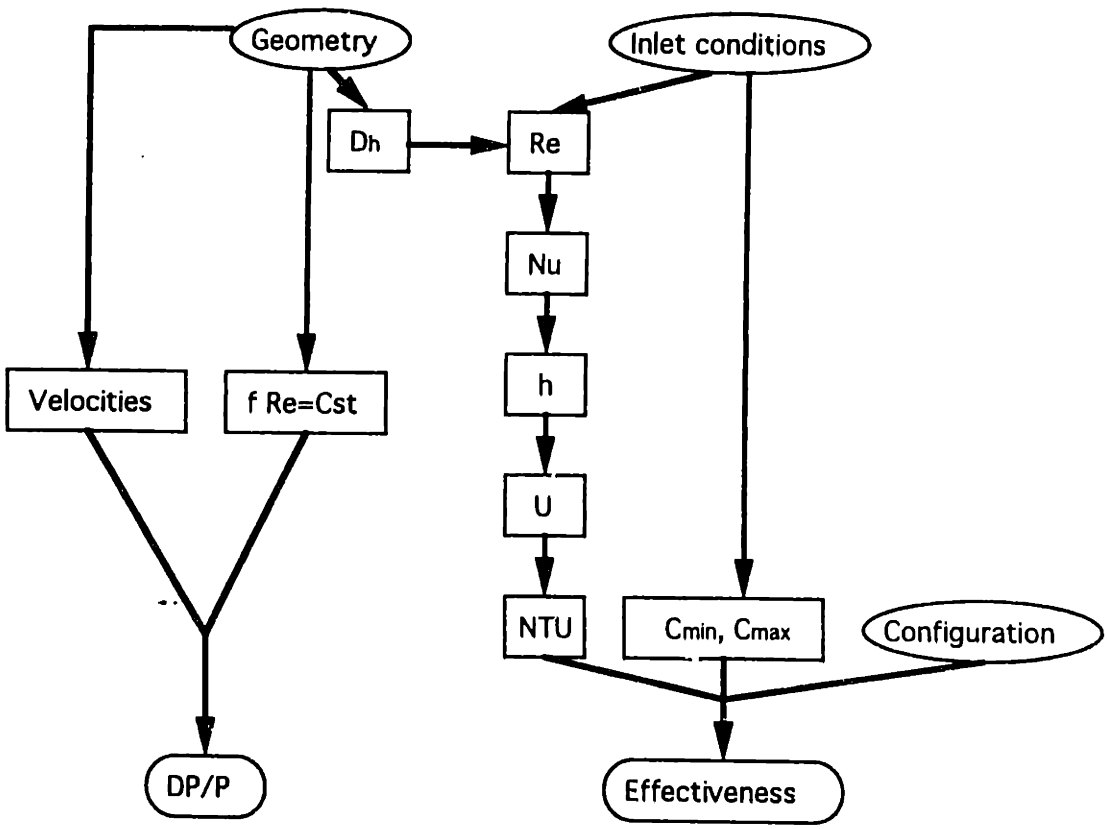

Figure 4-1: Heat Exchanger Design procedure.

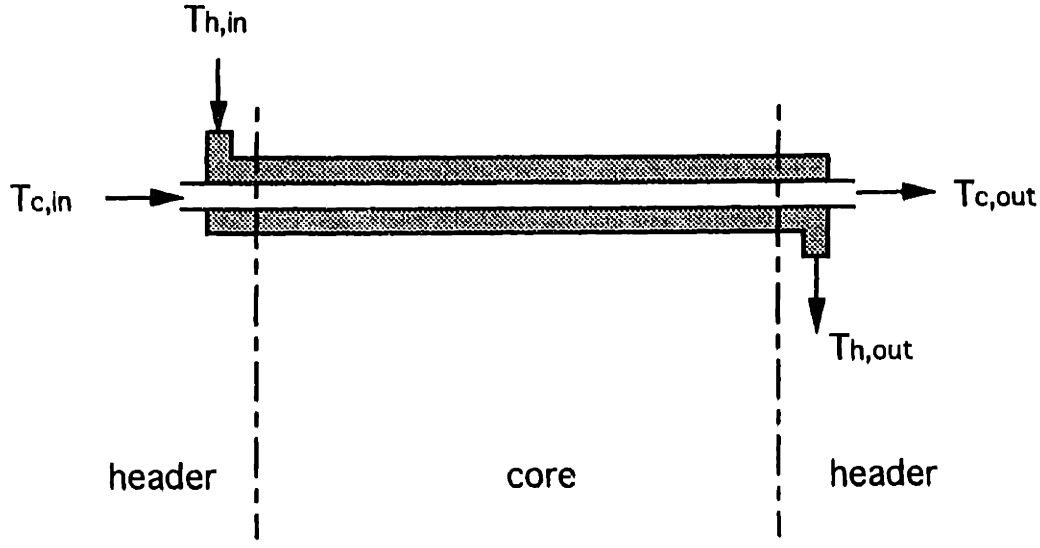

Figure 4-2: Parallel-flow heat exchanger.

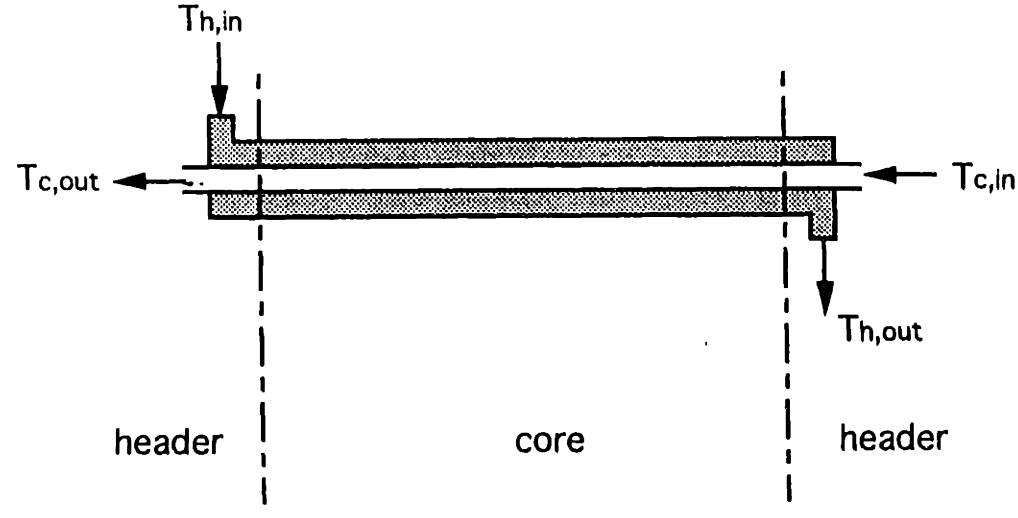

Figure 4-3: Counterflow heat exchanger.

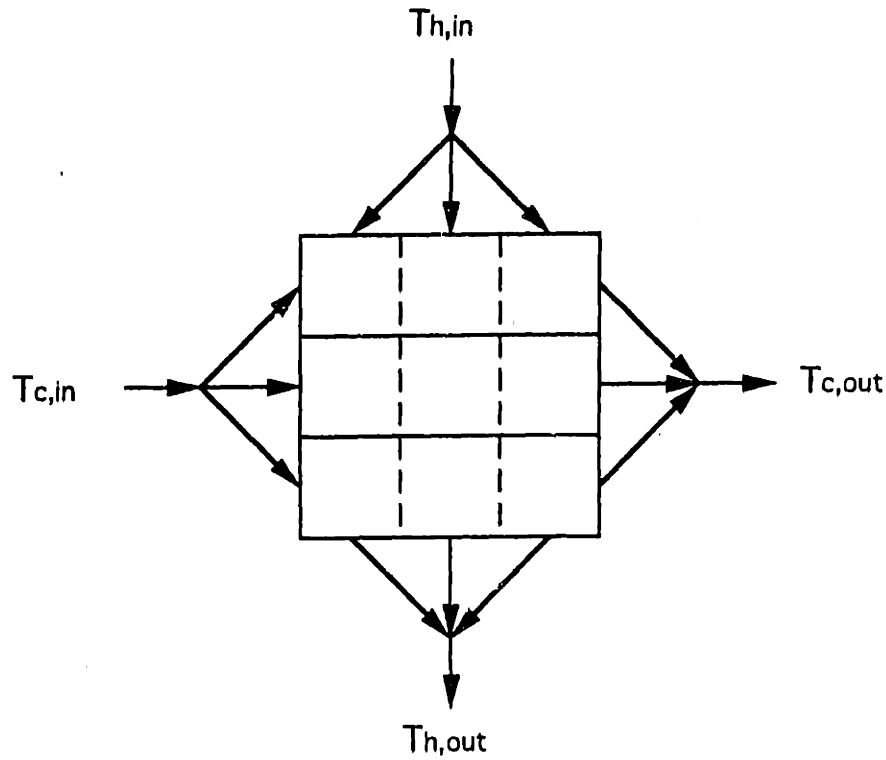

Figure 4-4: Cross-flow heat exchanger, both fluids unmixed.

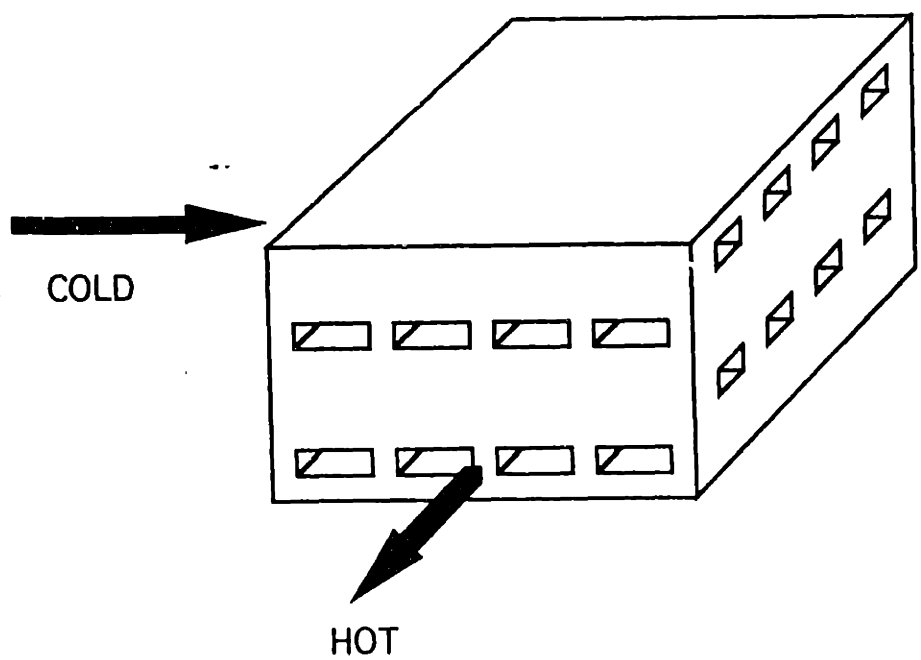

Figure 4-5: Cross-flow recuperator.

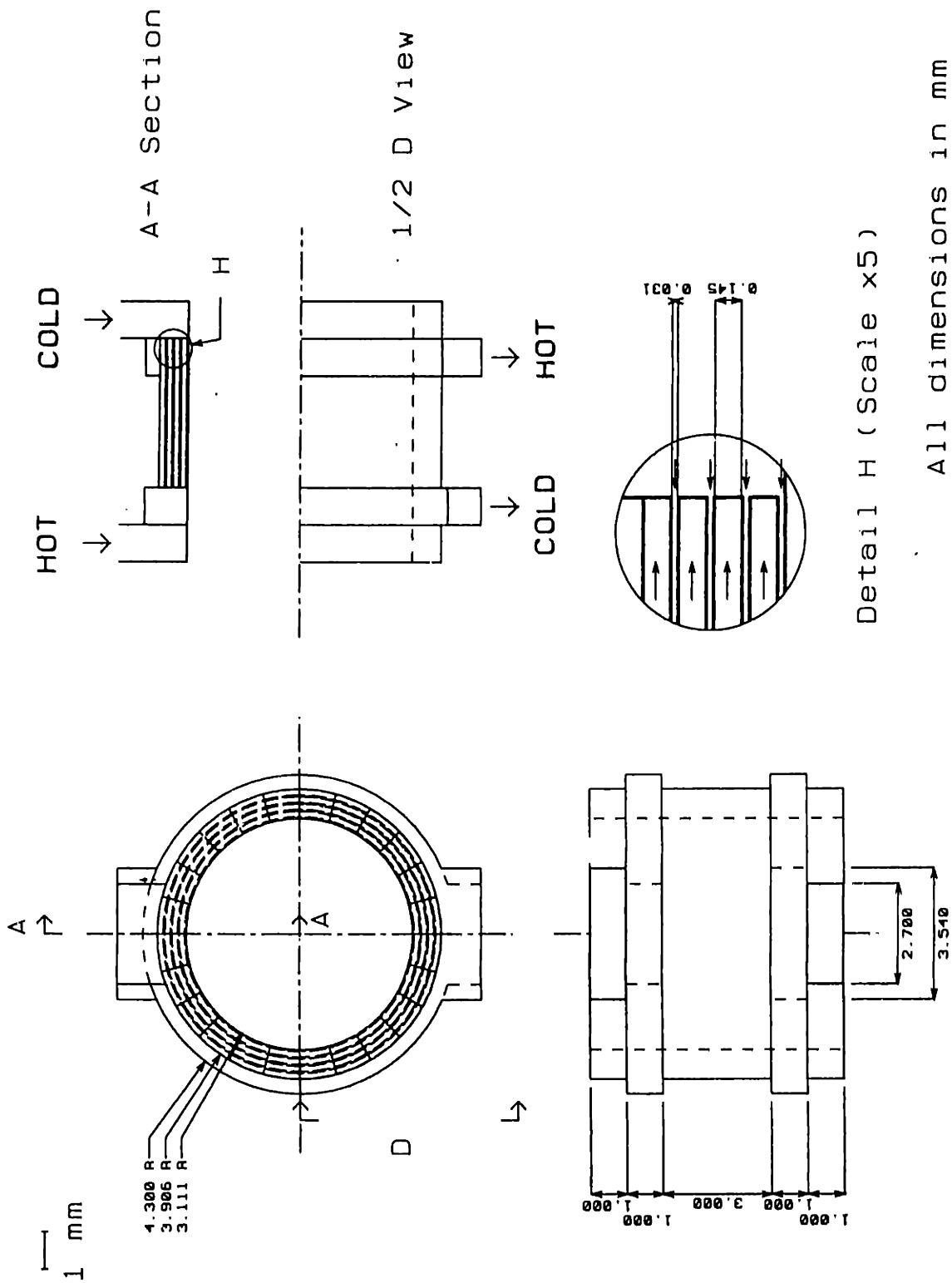

Figure 4-6: Concentric heat exchanger design sketch.

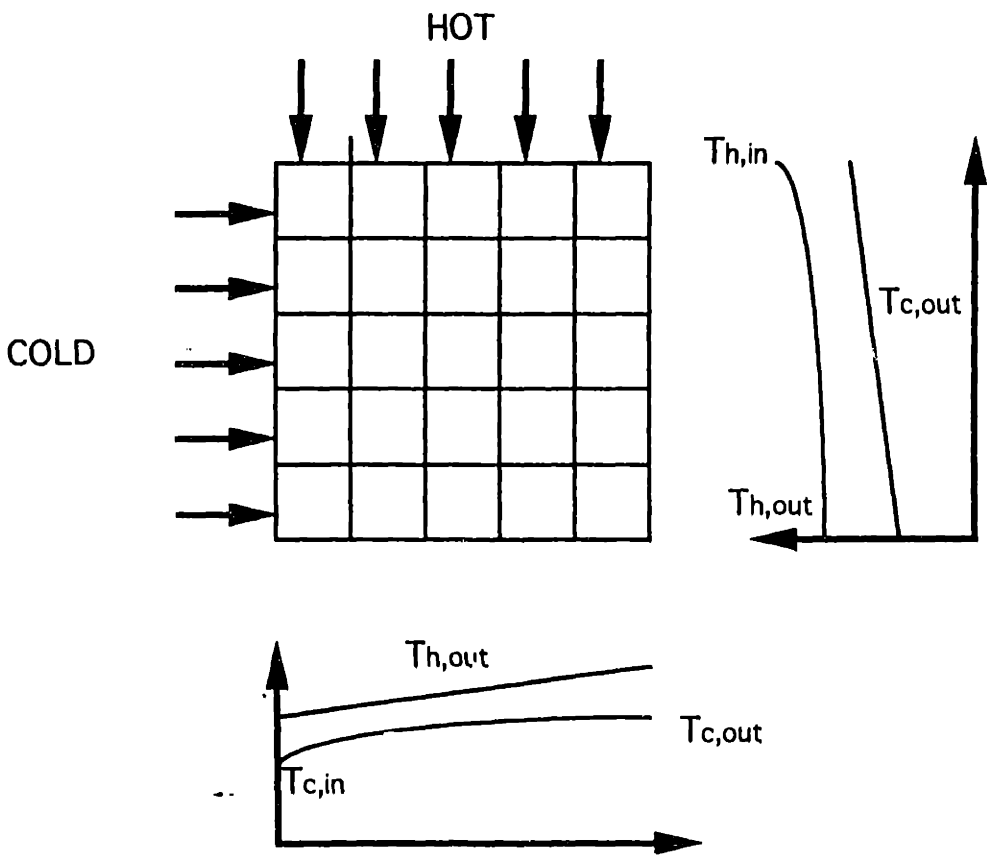

Figure 4-7: Cross-flow heat exchanger temperature profile (both fluids unmixed).

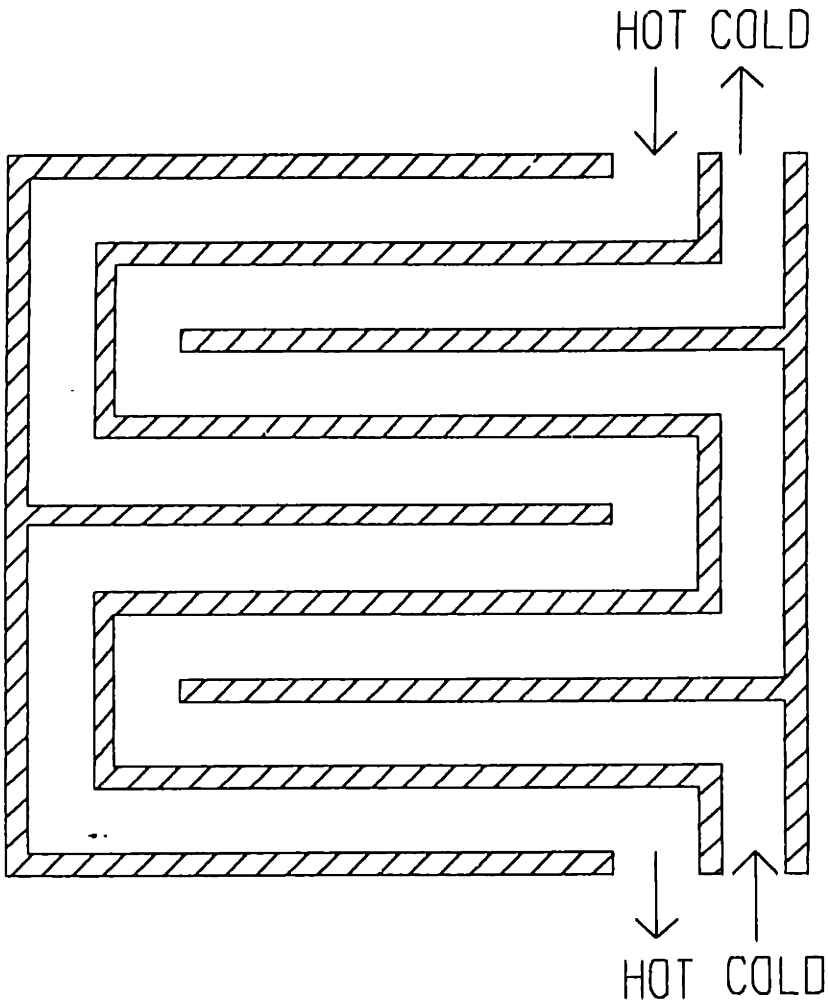

Figure 4-8: Counterflow heat exchanger with simple 2D geometry.

Chapter 5

Engine Cycle Optimization

5.1 Introduction

Chapter 2 outlined a parametric engine cycle analysis for a Jet A-fueled gas turbine. The main concern was to identify the interplay between engine component characteristics at break-even. We now must optimize the cycle for shaft power production. This chapter presents the optimized cycles for a turboshaft with and without a recuperator. Hydrogen is now the fuel considered since it presents many advantages compared to hydrocarbon fuels such as Jet A [3]:

- wide flammability limits: 4 to 75% Vol.,
- high autoignition temperature: $858K$,
- high heating value: $120kJ/g$.

The tool used for this investigation is a gas turbine cycle deck known as GASTURB (v. 6.0) [16]. This program was written for hydrocarbon fueled engine cycle analysis. Therefore, modifications were necessary before using it to study a hydrogen-fueled micro-gas turbine engine. These modifications are detailed in Appendix C.

This chapter first proposes a theoretical introduction to cycle optimization, then presents the optimized cycle and shows the sensitivity of this optimum to parameter variations.

5.2 Cycle Optimum Considerations

The power density of a gas turbine engine can be characterized by two parameters:

- the Specific Shaftpower defined as the ratio of the power output to the air massflow rate $\frac{P_{out}}{\dot{m}_{air}}$. The size of the engine is in particular set by $\dot{m}_{air}$, so that the specific shaftpower represents one aspect of the power compactness. The higher this parameter, the more compact the power source.

- the Power Specific Fuel Consumption (PSFC) defined as the ratio of the fuel massflow rate to the power output $\frac{\dot{m}_f}{P_{out}}$. The PSFC represents the mass of fuel burned for producing one unit of energy. Therefore, the lower the PSFC, the more fuel efficient the gas turbine.

For our application, we have set the air inlet area to $1mm^2$, thus imposing an air massflow rate of $1.8 * 10^{-4} kg/s$. Therefore, maximizing the specific shaftpower is equivallent to maximize the power output. However, optimizing the engine cycle for minimum PSFC seems more appropriate, for the tank will dominate the size of the engine as soon as more than a few minutes of operation are required. The micro-gas turbine will therefore be optimized for minimum PSFC.

A simple theoretical approach shows that there is a compressor pressure ratio π_c that minimizes the PSFC, everything else being kept the same. The ideal Brayton cycle represents the gas turbine engine cycle in a temperature-entropy diagram, as shown on Figure 5-1. As previously described, the air flow is isentropically compressed (segment 2-3), then heated at constant pressure (3-4) and isentropically expanded down to the inlet pressure (4-5). The fuel flow is proportional to the temperature difference ΔT_{3-4}. The power output is positive when the turbine temperature difference ΔT_{4-5} is larger than that of the compressor ΔT_{2-3} (assuming the same C_p). In the ideal cycle, there is always excess power, due to the diverging of the iso-pressure curves with increasing entropy in the (T,S) diagram. The cycle peak temperature is limited to T_{max} by material capability. The pressure ratio is therefore also limited to a maximum value.

Considering a compressor pressure ratio of 1, the cycle is 2-3'-4'-5' (see Figure 5-1). The pressure output is zero but the fuel massflow is not zero. The corresponding PSFC is then infinite. If a slightly higher pressure ratio is taken (cycle 2-3"-4"-5" on Figure 5-1), P_{out} is then strictly positive, so that the PSFC is now finite. Thus, for increasing compressor pressure ratios starting at 1, the PSFC is decreasing. It could be shown that for an ideal cycle, the minimum PSFC is obtained for the maximum π_c (corresponding to $T_3 = T_4$).

However, the analysis of a cycle with inefficiencies proves the existence of a compressor pressure ratio minimizing the PSFC. Figure 5-2 represents a break-even cycle 2-3-4-5 with inefficiencies in compression and expansion (entropy is created during these processes). The power output is zero but the fuel flow is not, so that the PSFC is infinite. When π_c is slightly decreased (cycle 2-3'-4'-5' on Figure 5-2), the turbine produces more power than required from the compressor. The power output is then strictly positive and the resulting PSFC is finite. This shows that for an inefficient cycle, an increase of the compressor pressure ratio near its maximum value increases the PSFC. Thus, when π_c increases from 1 to $\pi_{c,max}$, the PSFC first decreases and then increases. Therefore, there is a pressure ratio π_c minimizing the power specific fuel consumption.

In this section, only the compressor pressure ratio has been considered as an optimizing variable. The next section also considers other cycle parameters and proposes a numerical optimization.

5.3 Engine Cycle Optimization

As previously explained, the gas turbine cycle is optimized for minimum power specific fuel consumption. This optimization is constrained by the component characteristics. Some of these characteristics can be estimated accurately and therefore are set to their probable value as shown in Table 5.1. For others, only achievable ranges can be evaluated (see Table 5.2). Optimization is then obtained by varying these parameters within the defined ranges.

$\dot{m}_{air}\ (kg/s)$	$1.8 * 10^{-4}$
η_{burner}	99.5%
π_{burner}	0.95
$\eta_{HE} = \epsilon$	75%
$(P_{t,out}/P_{t,in})_{HE,cold}$	0.96
$(P_{t,out}/P_{t,in})_{HE,hot}$	0.94

Table 5.1: Fixed cycle parameters

Parameter	Range
π_c	≤ 5
η_c	$0.3 - 0.5$
η_t	$0.6 - 0.7$
T_{t4}	$1500 - 1600\ K$
P_{out}	≥ 0

Table 5.2: Parameter range

The gas turbine cycle deck GASTURB provides a mathematical optimization routine which has been used in the present situation. The actual optimization inputs are summarized in Table 5.3 and are detailed in Appendix C. The analysis developed in the next section shows that within the ranges considered here, any increase in η_c, η_t or T_{t4} decreases the PSFC. Therefore, these parameters have been set to their maximum reasonable value:

$$\eta_c = 0.5$$

$$\eta_t = 0.7$$

$$T_{t4} = 1600\ K$$

and only the two variables π_c and P_{out} have been used for optimization.

The cycle optimization with GASTURB shows that the minimum PSFC is obtained for $\pi_c = 4.6$ when there is no recuperation and for $\pi_c = 3.7$ when a heat

	Parameters	Range
Variable	π_c	$2.5 - 5$
	$P_{out}\ (kW)$	≥ 0
Figure of merit	$PSFC$	*minimized*

Table 5.3: GASTURB inputs for cycle optimization.

exchanger is added. The perfomance is then:

without recuperator:

$$\pi_c = 4.6$$
$$P_{out} = 15.8W$$
$$PSFC = 0.452kg/(kW * h)$$
$$\dot{m}_f = 7.15g/h$$

with recuperator:

$$\pi_c = 3.7$$
$$P_{out} = 10.6W$$
$$PSFC = 0.317kg/(kW * h)$$
$$\dot{m}_f = 3.35g/h$$

It can already be noticed that the use of a heat exchanger reduces the PSFC by 30% at the expense of the power output which drops by 30%. This gain comes from the reduction by half of the fuel consumption.

5.4 Parametric Analysis

This section provides a parametric analysis that is similar to that done in Chapter 2, except that here the engine operates with excess power, not only at break-even. The main concern now is to analyze the sensitivity of the optimum to each parameter and to identify the expected level of performance.

Figures 5-3 to 5-19 illustrate the results of this analysis. The design cycle is plotted with a square. The curves are obtained by computation of a few points (nodes of the grid) and then interpolation. For the results presented in each figure, two parameters have been varied simultaneously. The compressor pressure ratio π_c is always one of these parameters since it is the optimizing variable. The PSFC is the main concern. However, the power output must also be considered if a specific level of performance is desired.

	η_c	η_t	T_{t4} (K)	$\pi_{c,opt}$	$\dot{m}_f$ (g/h)	P_{out} (W)	$PSFC$ $(kg/(kW*h))$
	0.45	0.7	1600	3.5	7.39	10.9	0.679
$\Rightarrow$	0.5	0.7	1600	4.6	7.15	15.8	0.452
	0.55	0.7	1600	5	7.20	21.0	0.343
	0.45	0.6	1600	2.5	7.91	3.8	2.075
	0.5	0.6	1600	3.1	7.74	7.5	1.029
	0.5	0.8	1600	5	7.01	26.3	0.266
	0.5	0.7	1500	3.9	6.56	11.7	0.560

Table 5.4: Non-recuperated optimum performance with variations in the main cycle characteristics (assuming a $1mm^2$ intake area, $\dot{m}_{air} = 1.8 * 10^{-4} kg/s$). $\Rightarrow$ indicates the design cycle.

This analysis leads to the following observations.

Engine without recuperator

- At given π_c, any gain in η_c, η_t or T_{t4} reduces the Power Specific Fuel Consumption, which confirms what was stated for the cycle optimization (see Figures 5-3, 5-9, 5-13).

- If a higher compressor or turbine efficiency η_c or η_t can be obtained, a higher compressor pressure ratio π_c is necessary for minimizing the PSFC (see Figure 5-3, 5-9). The same is also true with the turbine inlet temperature T_{t4} (see Figure 5-13).

- The minimum PSFC does not correspond to the maximum power output P_{out}. The minimum $\frac{\dot{m}_f}{P_{out}}$ is obtained with a pressure ratio π_c which is always less than that corresponding to the maximum P_{out} (see Figure 5-7. For instance, at design point without recuperator, $(\pi_c)_{PSFC\ min} = 4.6$ and $(\pi_c)_{P_{out}\ max} = 3.9$. Thus, the pressure ratio difference is large between the two optimum. However, the power output and PSFC differences are very small. For instance, selecting π_c for minimum PSFC represents a power loss of less than $0.5W$ compared to the maximum P_{out}.

- Table 5.4 summarizes the optimum sensitivity to the main cycle parameters.

	η_c	η_t	T_{t4} (K)	n_{HE}	$\pi_{c,opt}$	$\dot{m}_f$ (g/h)	P_{out} (W)	$PSFC$ $(kg/(kW*h))$
	0.45	0.7	1600	0.75	3.15	3.20	5.5	0.586
$\Rightarrow$	0.5	0.7	1600	0.75	3.7	3.35	10.6	0.317
	0.55	0.7	1600	0.75	4.2	3.47	15.4	0.225
	0.5	0.6	1600	0.75	2.9	3.02	2.8	1.098
	0.5	0.8	1600	0.75	4.5	3.69	20.1	0.184
	0.5	0.7	1500	0.75	5	2.96	6.8	0.435
	0.5	0.7	1600	0.6	4	4.21	10.8	0.389
	0.5	0.7	1600	0.4*	4.2	5.29	13.3	0.397

Table 5.5: Recuperated optimum performance with variations in the main cycle characteristics (assuming a $1mm^2$ intake area, $\dot{m}_{air} = 1.8 * 10^{-4} kg/s$). $\Rightarrow$ indicates the design cycle. * in the last case indicates that heat exchanger total pressure ratios of 98% and 97% have been used instead of 96% and 94% for the cold and hot sides respectively.

The optimum pressure ratio is sometimes limited to 5 in order to remain in the reasonable range, but then it does not correspond to an absolute optimum. The power output is a lot more sensitive to parameter variations than is the fuel flow; this is the main source of variation in the PSFC.

- The power output for $\eta_c = 0.45$, $\eta_t = 0.6$ and $T_{t4} = 1600K$ is very low. Therefore, no cycle can be defined for lower efficiencies, except with very low pressure ratios.

Engine with recuperator

- As for the engine with no recuperator, any gain in η_c, η_t or T_{t4} reduces the PSFC but also increases the required compressor pressure ratio π_c for optimization (see Figures 5-4, 5-10, 5-14).

- In general, the minimum PSFC and the maximum power output do not correspond to the same π_c, everything else remaining the same. In opposition to the non recuperated case, $(\pi_c)_{PSFC\ min}$ is less than $(\pi_c)_{P_{out}\ max}$, at least in the effectiveness range considered, but the power output difference between the two cases is still very small (about $0.2W$). Figure 5-19 shows that when ϵ decreases,

the difference between $(\pi_c)_{PSFC\ min}$ and $(\pi_c)_{P_{out}\ max}$ also decreases, so that at $\epsilon = 0.6$, both pressure ratios match.

- Higher heat exchanger effectivenesses require lower compressor pressure ratios for optimization. The resulting PSFC then drops greatly (see Figure 5-14), but the change in P_{out} is very slight (see Figure 5-16).

- Table 5.5 illustrates quantitatively the optimum performance variation with changing component characteristics. The last case corresponds to a heat exchanger with very low effectiveness (0.4) and low total pressure drops (2% of the inlet pressure on the cold side, 3% on the hot side); the cold flow exit temperature is then $870K$, thus limiting the risk of hydrogen autoignition.

Comparison of the two configurations

- On one side, P_{out} increases greatly in both configurations when η_c is raised and π_c is adjusted for optimization. On the other side, for the same parametric variation, $\dot{m}_f$ increases for the recuperated engine and decreases for the non-recuperated one. However, the fuel massflow change is very small, so that the resulting optimum PSFC is always increasing when η_c is raised. Considering η_t instead of η_c leads to the same observation.

- The PSFC without recuperation is obviously larger than with it (by roughly $0.1kg.kW^{-1}.h^{-1}$), because of the higher fuel consumption without heat exchanger (factor 2 between the two cases). However, the maximum power output is larger without this additional device which introduces pressure drop across the channels. Thus, about $5W$ are lost by using a recuperator.

- The recuperated engine with a low effectiveness, low pressure drop heat exchanger is an attractive alternative to the non-recuperated engine. This additional device reduces the PSFC from 0.452 to $0.397kg/(kW * h)$ for a powerloss of $3W$. The fuel consumption is also reduced by $2g/h$.

5.5 Conclusion

This chapter has determined the optimum cycles with and without recuperator, thus establishing micro-gas turbine component design goals. It also gives curves illustrating the sensitivity of this optimum to the component performance: they will be useful further in the project when actual component characteristics will be known accurately.

This analysis showed that very high power density can be obtained (the Power Specific Fuel Consumption ranges from 0.3 to 0.4 $kg/(kW*h)$, especially when a recuperator is added to the cycle. The shaft power ranges from 10 to $20W$ per mm^2 inlet area (60 to 90 $kW/(kg_{air}/s)$). This does not represent a wide margin above break-even, since no parasitic losses such as bearing friction have been considered. The recuperator worsens the situation through its additional pressure drop. Therefore, inspite of the resulting PSFC loss, it is believed that an engine without recuperation should be considered first in order to maximize success in terms of power output. Then, the engine complexity would also be reduced.

Table 5.6 presents the microengine design cycle and compares it to two large scale radial gas turbines. The first comparative engine is an automotive gas turbine called Advanced Gas Turbine (AGT 100) developed by Allison Gas Turbines (1988) under a NASA/DOE contract [2]. The second one is a typical light helicopter turboshaft engine [8]. Microengine component efficiencies are assumed low in comparison to the other engines. In our design, we set them below routinely achieved efficiencies to account for the penalty imposed by the low Reynolds numbers. Logically, the resulting specific power (power per unit airflow) is lower for microengines than for the other turboshafts. However, the PSFC are roughly of the same order of magnitude in all cases. The reason is that hydrogen, which is burned in the microengine, has a higher heating value than diesel, JP-5 or methanol for which the AGT and the helicopter turboshaft are designed. This better fuel thus compensates for the lower efficiencies in term of power density.

Characteristic	Microengine		AGT	Helicopter engine
	without recuperator	with recuperator		
Power (W)	15.8	10.6	50,000	415,000
PSFC $(kg_{fuel}/(kW * h))$	0.452	0.317	0.278	0.38
Specific power $(kW/(kg_{air}/s))$	87.8	58.9	151	163
Airflow rate (kg/s)	$1.8 * 10^{-4}$	$1.8 * 10^{-4}$	0.33	2.5
$T_{t4}(K)$	1600	1600	1470	≈ 1600
π_c	4.6	3.7	4.34	8.5
η_c	0.5	0.5	0.77	0.77
η_t	0.7	0.7	$\eta_{t,gasifier} = 0.80$ $\eta_{t,power} = 0.86$	0.90
n_{HE}	–	0.75	0.91	–

Table 5.6: Comparison of the microengine design with an automative gas turbine (Allison AGT 100) and a typical light helicopter turboshaft

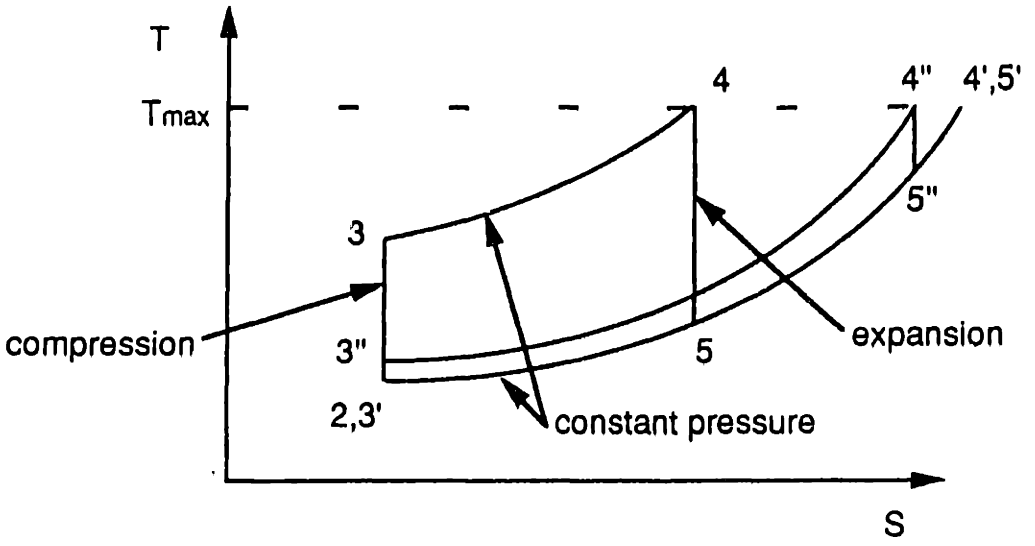

Figure 5-1: Temperature-entropy diagram of an ideal Brayton gas turbine engine cycle.

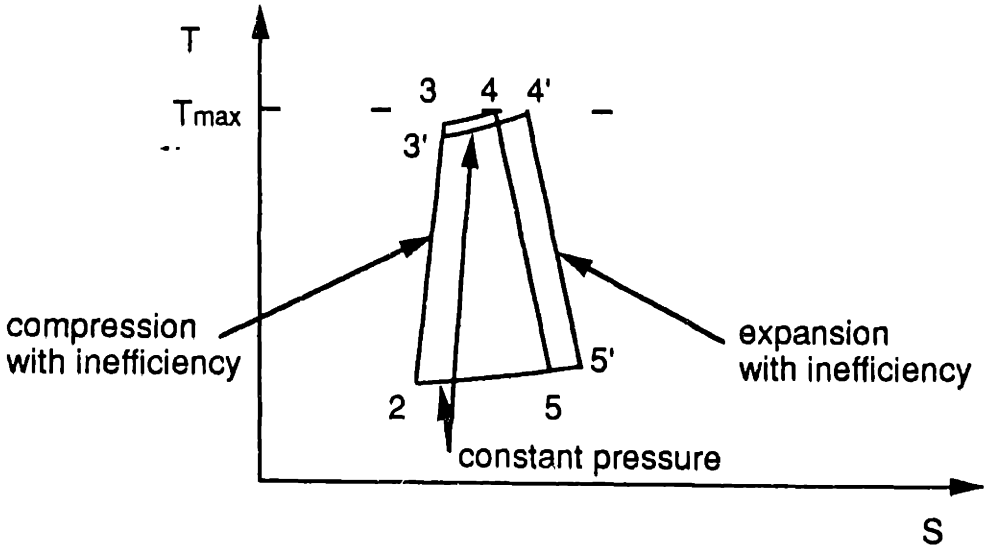

Figure 5-2: Temperature-entropy diagram of a Brayton gas turbine engine cycle with compression and expansion inefficiencies.

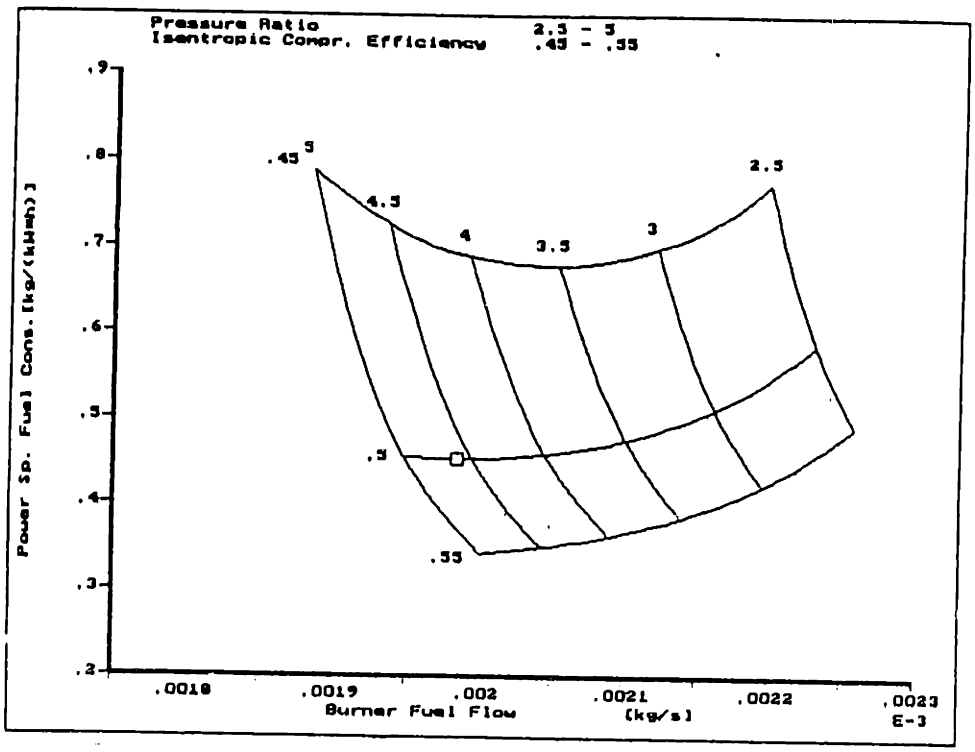

Figure 5-3: Power Specific Fuel Consumption as a function of Fuel Flow for different Pressure Ratios and Isentropic Compressor Efficiencies ($\dot{m}_{air} = 1.8 * 10^{-4} kg/s$, $\eta_t = 0.7$, $T_{t4} = 1600K$, no recuperator)

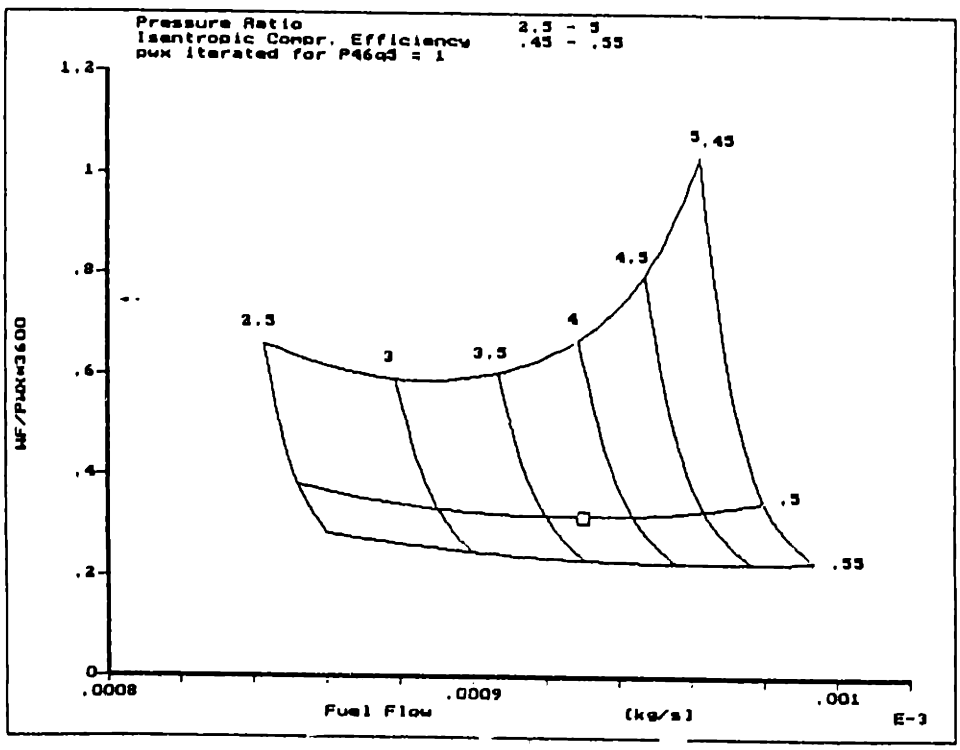

Figure 5-4: Power Specific Fuel Consumption ($kg/(kW.h)$) as a function of Fuel Flow for different Pressure Ratios and Isentropic Compressor Efficiencies ($\dot{m}_{air} = 1.8 * 10^{-4} kg/s$, $\eta_t = 0.7$, $T_{t4} = 1600K$, with recuperator: $\epsilon = 0.75$, $(P_{t,out}/P_{t,in})_{cold} = 0.96$, $(P_{t,out}/P_{t,in})_{hot} = 0.94$)

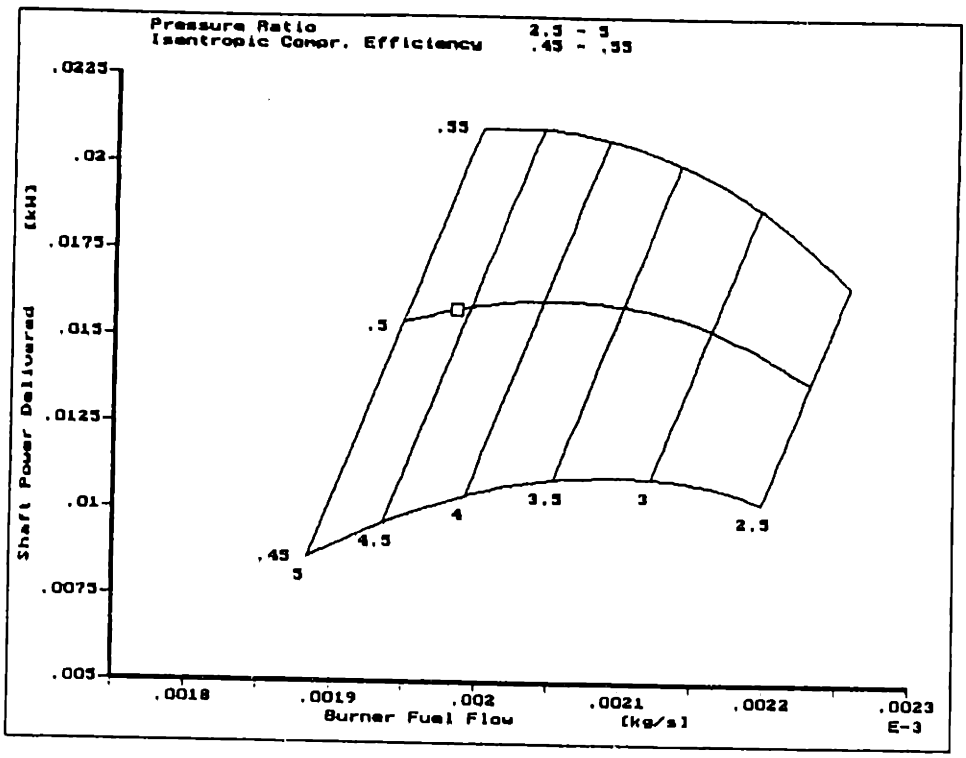

Figure 5-5: Shaft Power Delivered as a function of Fuel Flow for different Pressure Ratios and Isentropic Compressor Efficiencies ($\dot{m}_{air} = 1.8 * 10^{-4} kg/s$, $\eta_t = 0.7$, $T_{t4} = 1600K$, no recuperator)

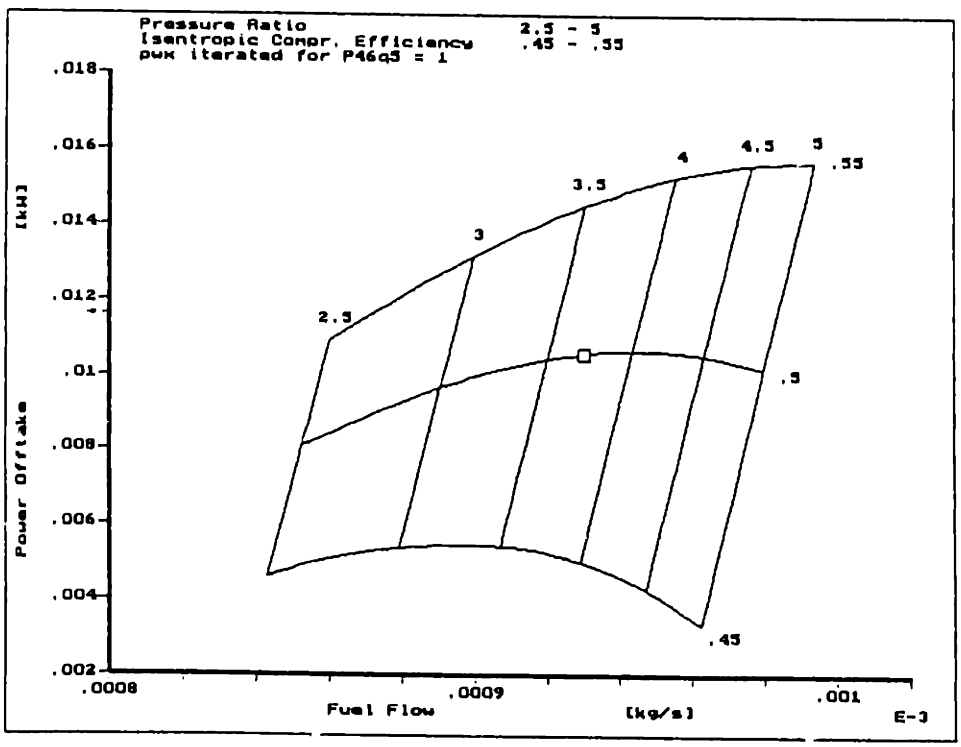

Figure 5-6: Shaft Power Delivered as a function of Fuel Flow for different Pressure Ratios and Isentropic Compressor Efficiencies ($\dot{m}_{air} = 1.8 * 10^{-4} kg/s$, $\eta_t = 0.7$, $T_{t4} = 1600K$, with recuperator: $\epsilon = 0.75$, $(P_{t,out}/P_{t,in})_{cold} = 0.96$, $(P_{t,out}/P_{t,in})_{hot} = 0.94$)

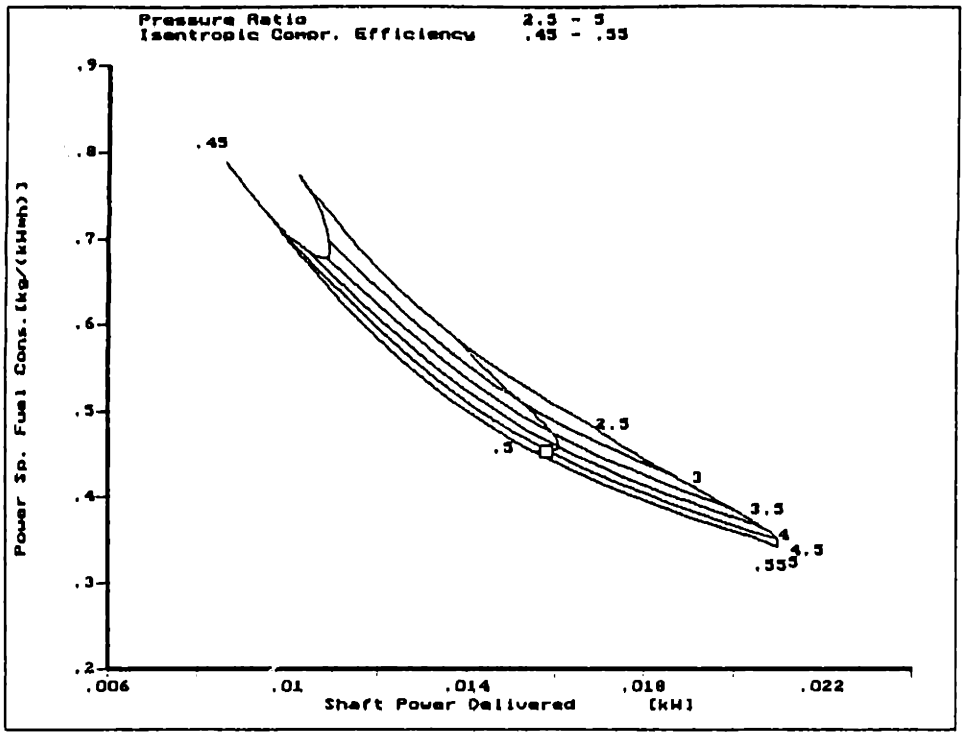

Figure 5-7: Power Specific Fuel Consumption as a function of Shaft Power Delivered for different Pressure Ratios and Isentropic Compressor Efficiencies ($\dot{m}_{air} = 1.8 * 10^{-4} kg/s$, $\eta_t = 0.7$, $T_{t4} = 1600K$, no recuperator)

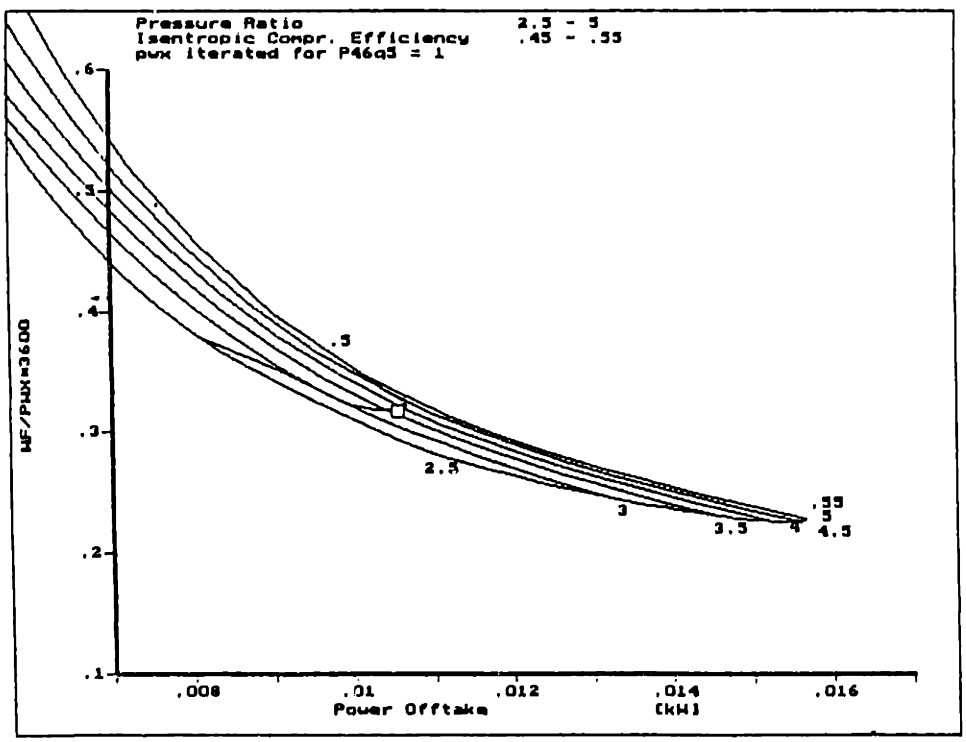

Figure 5-8: Power Specific Fuel Consumption ($kg/(kW.h)$) as a function of Shaft Power Delivered for different Pressure Ratios and Isentropic Compressor Efficiencies ($\dot{m}_{air} = 1.8 * 10^{-4} kg/s$, $\eta_t = 0.7$, $T_{t4} = 1600K$, with recuperator: $\epsilon = 0.75$, $(P_{t,out}/P_{t,in})_{cold} = 0.96$, $(P_{t,out}/P_{t,in})_{hot} = 0.94$)

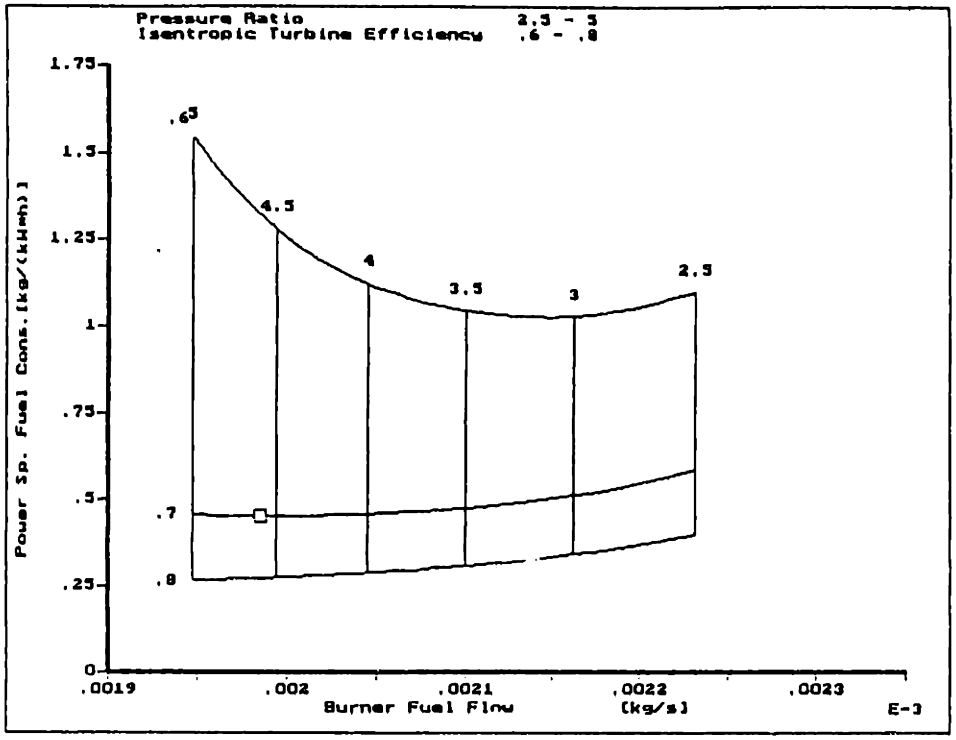

Figure 5-9: Power Specific Fuel Consumption as a function of Fuel Flow for different Pressure Ratios and Isentropic Turbine Efficiencies ($\dot{m}_{air} = 1.8 * 10^{-4} kg/s$, $\eta_c = 0.5$, $T_{t4} = 1600K$, no recuperator)

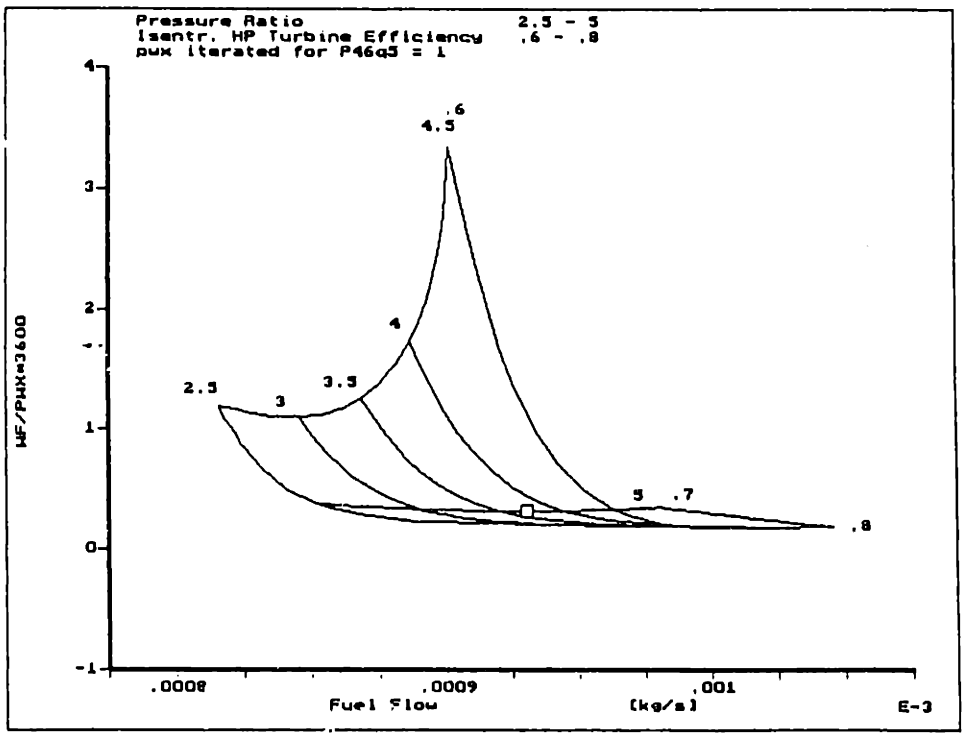

Figure 5-10: Power Specific Fuel Consumption ($kg/(kW.h)$) as a function of Fuel Flow for different Pressure Ratios and Isentropic Turbine Efficiencies ($\dot{m}_{air} = 1.8 * 10^{-4} kg/s$, $\eta_c = 0.5$, $T_{t4} = 1600K$, with recuperator: $\epsilon = 0.75$, $(P_{t,out}/P_{t,in})_{cold} = 0.96$, $(P_{t,out}/P_{t,in})_{hot} = 0.94$)

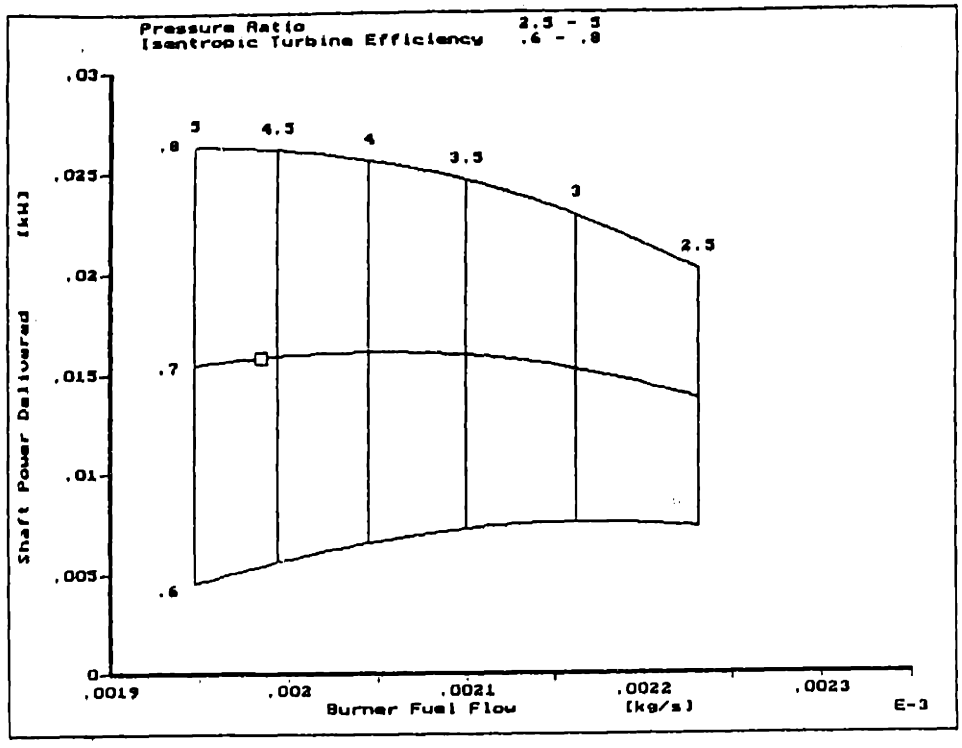

Figure 5-11: Shaft Power Delivered as a function of Fuel Flow for different Pressure Ratios and Isentropic Turbine Efficiencies ($\dot{m}_{air} = 1.8 * 10^{-4} kg/s$, $\eta_c = 0.5$, $T_{t4} = 1600K$, no recuperator)

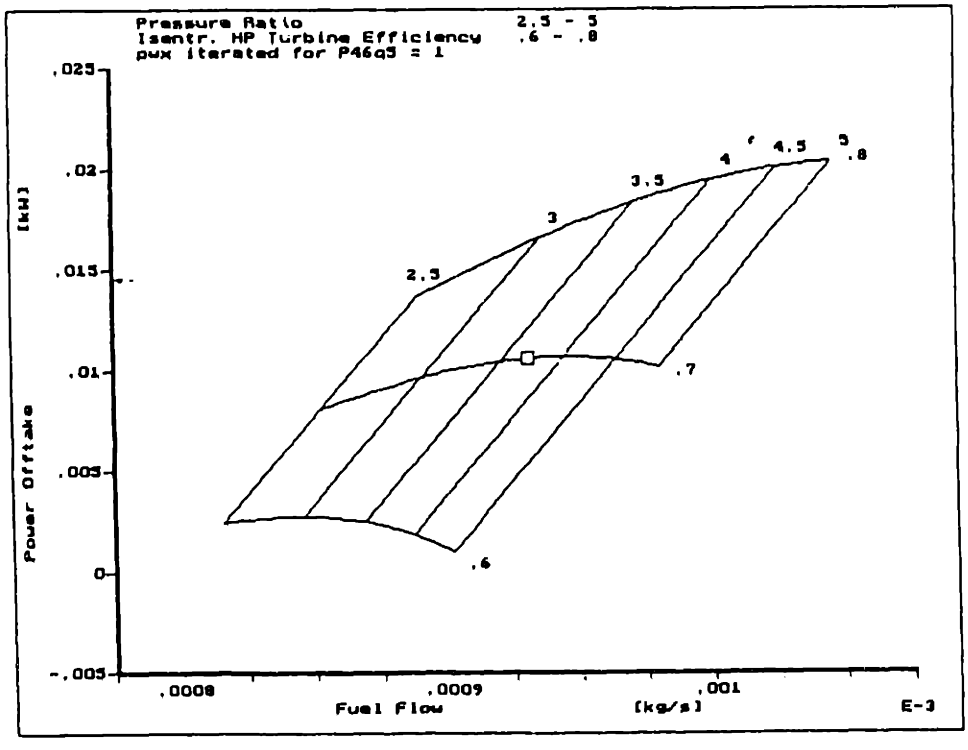

Figure 5-12: Shaft Power Delivered as a function of Fuel Flow for different Pressure Ratios and Isentropic Turbine Efficiencies ($\dot{m}_{air} = 1.8 * 10^{-4} kg/s$, $\eta_c = 0.5$, $T_{t4} = 1600K$, with recuperator: $\epsilon = 0.75$, $(P_{t,out}/P_{t,in})_{cold} = 0.96$, $(P_{t,out}/P_{t,in})_{hot} = 0.94$)

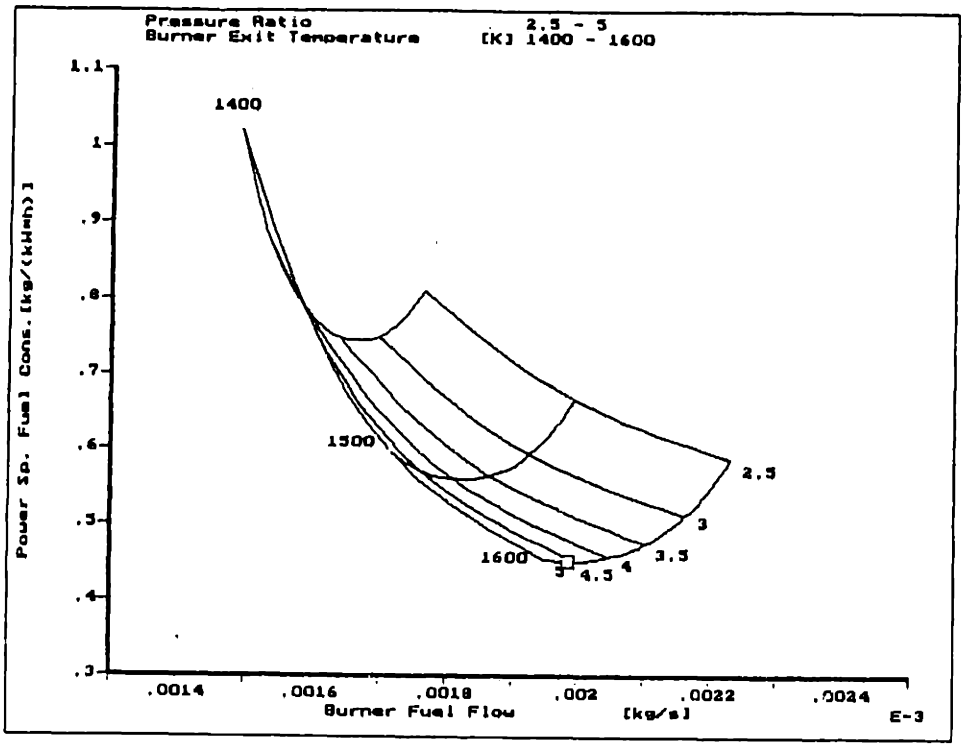

Figure 5-13: Power Specific Fuel Consumption as a function of Fuel Flow for different Pressure Ratios and Burner Exit Temperatures ($\dot{m}_{air} = 1.8 * 10^{-4} kg/s$, $\eta_c = 0.5$, $\eta_t = 0.7$, no recuperator)

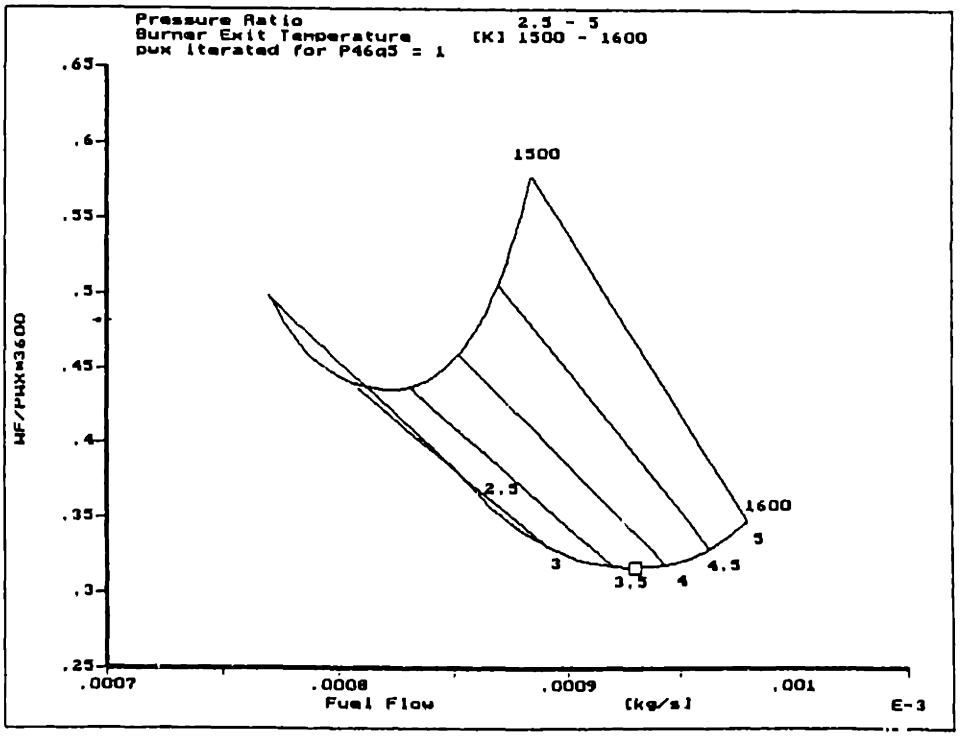

Figure 5-14: Power Specific Fuel Consumption ($kg/(kW.h)$) as a function of Fuel Flow for different Pressure Ratios and Burner Exit Temperatures ($\dot{m}_{air} = 1.8 * 10^{-4} kg/s$, $\eta_c = 0.5$, $\eta_t = 0.7$, with recuperator: $\epsilon = 0.75$, $(P_{t,out}/P_{t,in})_{cold} = 0.96$, $(P_{t,out}/P_{t,in})_{hot} = 0.94$)

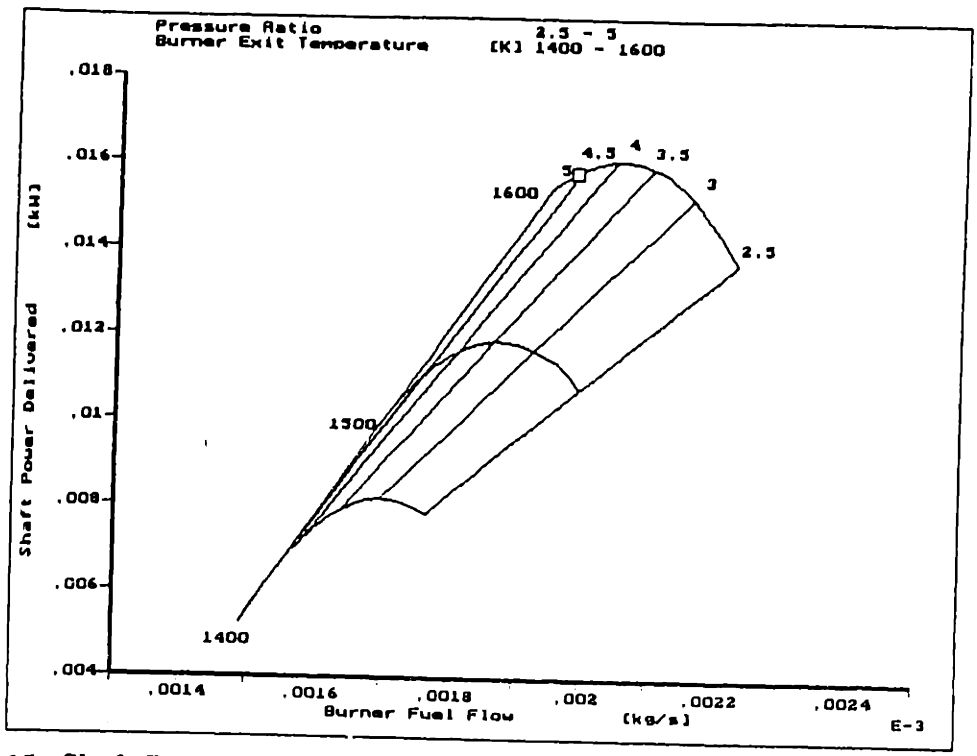

Figure 5-15: Shaft Power as a function of Fuel Flow for different Pressure Ratios and Burner Exit Temperatures ($\dot{m}_{air} = 1.8 * 10^{-4} kg/s$, $\eta_c = 0.5$, $\eta_t = 0.7$, no recuperator)

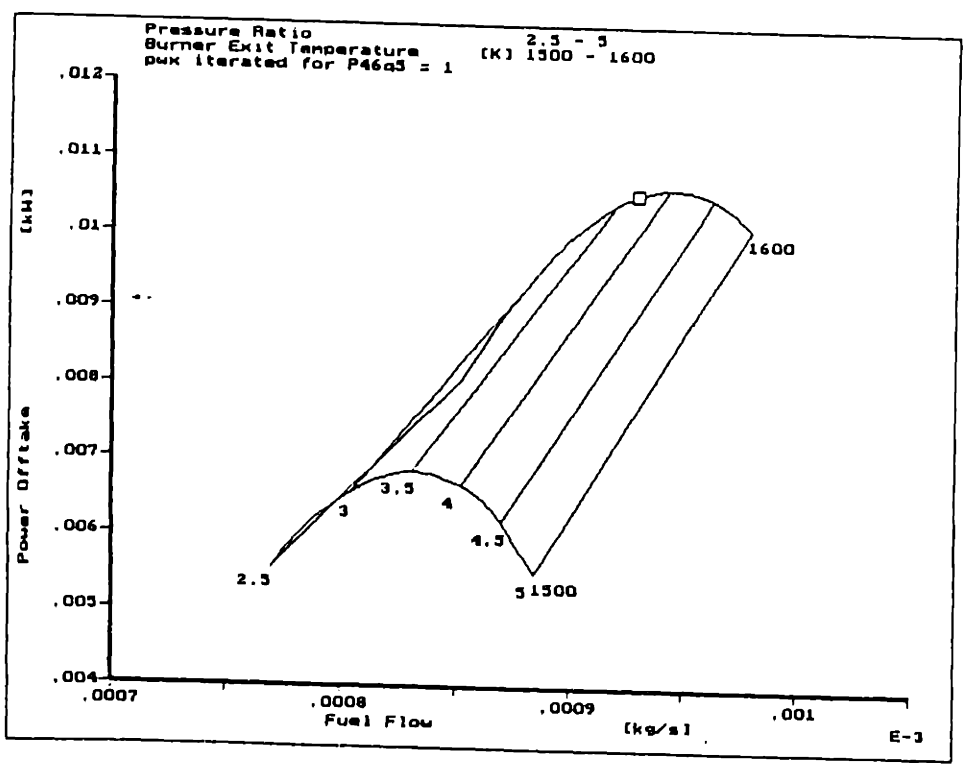

Figure 5-16: Shaft Power as a function of Fuel Flow for different Pressure Ratios and Burner Exit Temperatures ($\dot{m}_{air} = 1.8 * 10^{-4} kg/s$, $\eta_c = 0.5$, $\eta_t = 0.7$, with recuperator: $\epsilon = 0.75$, $(P_{t,out}/P_{t,in})_{cold} = 0.96$, $(P_{t,out}/P_{t,in})_{hot} = 0.94$)

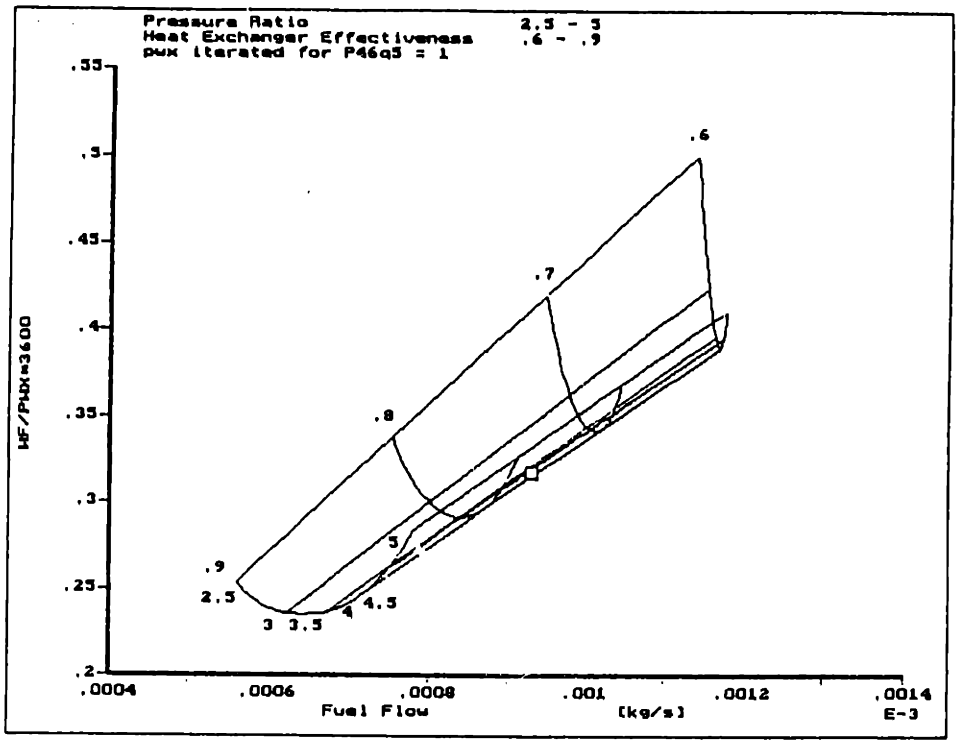

Figure 5-17: Power Specific Fuel Consumption ($kg/(kW.h)$) as a function of Fuel Flow for different Pressure Ratios and Heat Exchanger Effectiveness ($\dot{m}_{air} = 1.8 * 10^{-4} kg/s$, $\eta_c = 0.5$, $\eta_t = 0.7$, $T_{t4} = 1600K$, with recuperator: $(P_{t,out}/P_{t,in})_{cold} = 0.96$, $(P_{t,out}/P_{t,in})_{hot} = 0.94$)

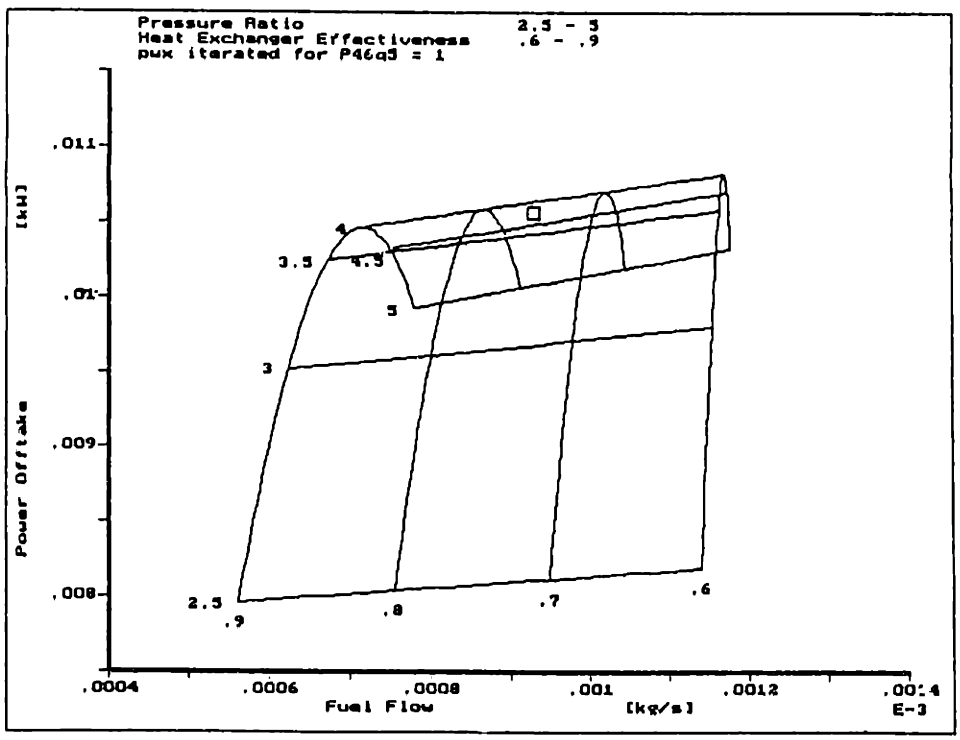

Figure 5-18: Shaft Power Delivered as a function of Fuel Flow for different Pressure Ratios and Heat Exchanger Effectiveness ($\dot{m}_{air} = 1.8 * 10^{-4} kg/s$, $\eta_c = 0.5$, $\eta_t = 0.7$, $T_{t4} = 1600K$, with recuperator: $(P_{t,out}/P_{t,in})_{cold} = 0.96$, $(P_{t,out}/P_{t,in})_{hot} = 0.94$)

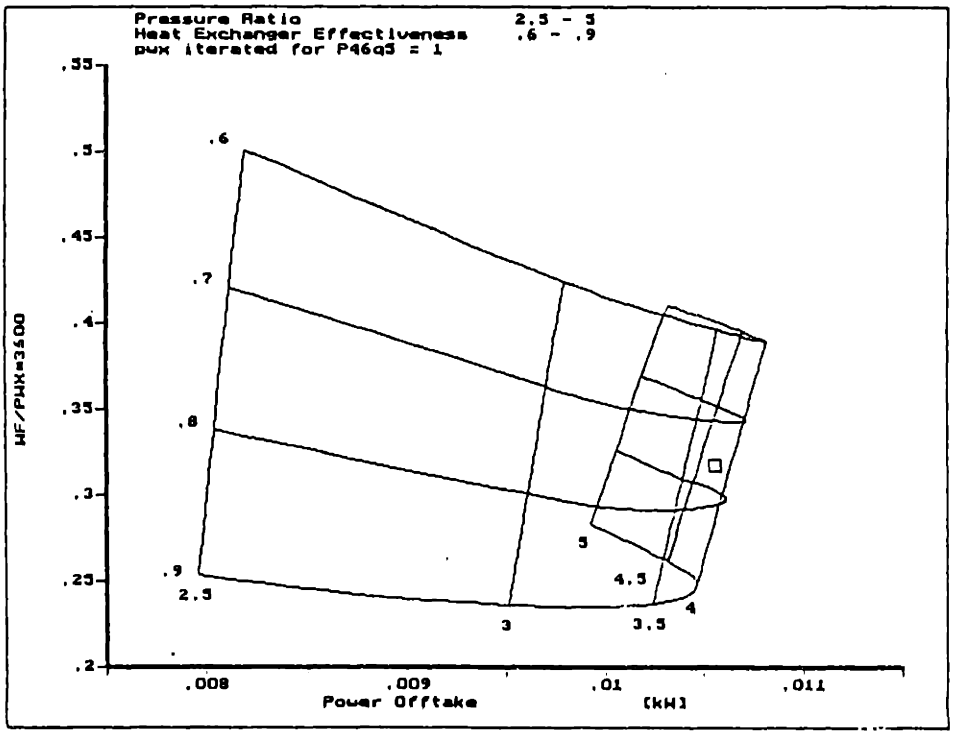

Figure 5-19: Power Specific Fuel Consumption ($kg/(kW.h)$) as a function of Shaft Power Delivered for different Pressure Ratios and Heat Exchanger Effectiveness ($\dot{m}_{air} = 1.8 * 10^{-4} kg/s$, $\eta_c = 0.5$, $\eta_t = 0.7$, $T_{t4} = 1600K$, with recuperator: $(P_{t,out}/P_{t,in})_{cold} = 0.96$, $(P_{t,out}/P_{t,in})_{hot} = 0.94$)

Chapter 6

Component Design

6.1 Introduction

The cycle optimization in the previous chapter has given an estimate of the level of performance required from each component. Now, we examine what each component may look like to achieve such performance. At this stage, only the non-recuperated engine is considered.

6.2 Compressor Design

6.2.1 Theoretical Approach

The cycle optimization of the micro-gas turbine without recuperator has set the following goals for the compressor:

$$\pi_c = 4.6$$
$$\eta_c = 0.5 \ .$$

Current microfabrication technology is capable of producing only planar components and this constraint suggests that a centrifugal type compressor would be most appropriate. Centrifugal compressors can have a planar design (although this is non-standard and will be addressed later in this section) and are capable of obtaining high

pressure ratios in a single stage, thus simplifying the compressor design. On the other hand, axial compressors are inherently three-dimensional and would require multiple stage for the desired pressure ratio. A drawback of centrifugal compressor is that they have a low massflow capacity per unit frontal area [14]. This, however, does not appear to be a concern for the microengine.

Therefore, a centrifugal compressor is considered. As we just explained, it can have a planar design even if this is a non-standard design. A centrifugal compressor consists of a rotor followed by a diffuser. The rotor spins the air, imparting angular momentum and also raising the pressure as the air moves radially outward. The diffuser converts the angular momentum in the fluid at the rotor outlet into static pressure rise. Typically, the total pressure rise through a centrifugal compressor is equally split between the rotor and diffuser. Conventional centrifugal rotors consist of two parts (see Figure 6-1): an inducer progressively spinning the flow through essentially axial passages and an impeller providing the radial acceleration. The former is highly three dimensional in order to prevent flow separation. Since microfabrication techniques do not allow this kind of geometry, the inducer will be omitted and the rotor will be reduced to simply an impeller. For the same reason, it would be difficult to build blades whose height changes with radius. The passage height will therefore be kept constant across the rotor and the stator.

The maximum allowable tip speed is constrained by the maximum stress that the material can bear. For a solid disc, the tangential and radial stresses at the center are given by:

$$\sigma_\theta = \sigma_r = \frac{3+\nu}{8}\rho V^2$$

where ν is the Poisson's ratio, ρ is the material density and V is the tip tangential velocity. For silicon carbide, $\nu = 0.25$ and $\rho = 3 * 10^3 kg/m^3$. A disc tip speed of $500m/s$ would lead to a stress of $\sigma \approx 300MPa$, giving a substantial margin on the theoretical tensile strength ($\sigma_f \approx 3GPa$). The actual margin may be smaller, since this σ_f has not been measured for SiC components made by microfabrication. In addition, the stress in the blade root will probably be critical. However, limiting the

rotor tip speed to not more than $500m/s$ seems to be conservative.

Given that the rotor tip speed is $500m/s$, setting the tip radius then sets the shaft rotational speed ω.

The Euler equation gives the rotor work, in this case for a gas with constant specific heat [14]:

$$c_p\,(T_{tc} - T_{tb}) = \omega(r_c v_c - r_b v_b) \tag{6.1}$$

where

station b: rotor inlet

station c: rotor exit and stator inlet

station d: stator exit

r: radius

v: absolute tangential velocity

The stagnation temperature is assumed constant across the stator, so that: $T_{tb} = T_{t2}$ and $T_{tc} = T_{td} = T_{t3}$. These values are set by the compressor characteristics π_c and η_c: $T_{t2} = 288K$ so that $T_{t3} = 603K$.

We assume that there are no inlet guide vanes so that there is no swirl at the rotor inlet and V_b is purely radial. Then, the absolute tangential velocity at the exit of the rotor can be obtained by Equation (6.1). We also assume that there is no swirl at the exit of the stator. Thus, all the tangential velocities are known.

The velocities are obtained by writing the mass flow conservation between the different stations. By considering the flow area ($2\pi * radius * (blade\ height)$) and the radial velocity V_r (which is perpendicular to the surface considered), this conservation can be written as follow:

$$\rho V_r * 2\pi r h = \dot{m}$$

or converted into an expression with absolute Mach numbers:

$$\frac{\dot{m}\sqrt{T_t}}{P_t\ 2\pi r h} = \sqrt{\frac{\gamma}{r}} M_{radial}(1 + \frac{\gamma - 1}{2} M^2)^{-\frac{\gamma+1}{2(\gamma-1)}} \tag{6.2}$$

If the radius is set and the height is kept constant, the absolute Mach number can

Station	b	c	d
$r\ (mm)$	1.00	1.60	3.00
$h\ (\mu m)$	141	141	141
M	0.60	1.62	0.05
$V\ (m/s)$	197	647	25
$v\ (m/s)$	0	632	0
$\beta\ (°)$	0	77.9	0
$\beta'\ (°)$	−57.8	44.2	−

$r_c\omega\ (m/s)$	500
$\omega\ (rpm)$	$3 * 10^6$
R	0.57
D_{rotor}	≥ 0.49
D_{stator}	≥ 0.96

Table 6.1: Compressor design parameters ($\gamma = 1.4$)

be deduced from the previous expression (the actual way to proceed is to iterate on the Mach number needed at a given radius in order to keep the height constant). Using large radius ratios leads to lower Mach numbers. The Mach numbers then yield the absolute velocities. All the velocity components (radial and tangential) are now known at each station and the angles with the radial direction can be calculated.

6.2.2 Results

The results are presented in Table 6.1 and in Figure 6-2.

The results show that the blade design will be very challenging. Very high angles are required for achieving the desired pressure ratio: the stator inlet angle in the absolute frame is very large and the turning in the rotor is almost 100°. The degree of reaction R defined on the basis of the static pressure rise [17]:

$$R = \frac{P_c - P_b}{P_d - P_b} \tag{6.3}$$

is not far from 0.5 as desired for a good "sharing of the burden of the stage static pressure rise" between the rotor and the stator [17]. However, the diffusion factors D are very high. Usually, no more than 0.5 is desirable in turbulent flow to avoid flow separation ([17] p.240). In laminar flow, this limit should even be lower. The

diffusion factor is defined as follow ([14] p.237):

$$D_{rotor} = (1 - \frac{V'_c}{V'_b}) + \frac{| v_c - v_b |}{2\sigma_r V'_b}$$

$$D_{stator} = (1 - \frac{V_d}{V_c}) + \frac{| v_d - v_c |}{2\sigma_s V_c}$$

where $\sigma = c/s$ is the ratio of the blade chord to the spacing between two blades. The first term corresponds to the average static pressure rise in the airfoil channel and the second to the additional static pressure rise along the suction surface due to curvature or lift [17]. The values given in Table 6.1 represent only the first term, the second always being positive. This shows that no matter how large σ is, the diffusion factor cannot go below this value. These large diffusion factors result from the height constraint on the blades which implies low velocities at the exit of the rotor and of the stator. These low velocities are perfect for the combustor which requires long residence time but are also favorable to flow separation. Many attempts have been made for reducing the diffusion factor without success. A solution could be to introduce a height step between the rotor and the stator in order to increase the velocities and to design it for limiting the pressure losses.

6.3 Turbine Design

6.3.1 Theoretical Approach

The cycle characteristics define the turbine pressure ratio required. The compressor and burner pressure ratios are set to $\pi_c = 4.6$ and $\pi_b = 0.95$ and we wish an exhaust stagnation pressure 1.03 times the ambient pressure: $P_{t5}/P_{amb} = 1.03$. The latter ratio gives a sufficient margin on the stagnation pressure above the ambient pressure to prevent blockage at the nozzle exit. Thus, the turbine design goal is $\pi_t = 0.236$ with an efficiency $\eta_t = 0.7$.

The turbine has to satisfy the same kind of constraints as the compressor. The microfabrication imposes a planar geometry so that a radial inflow turbine will be

Station	a	b	c
$r\ (mm)$	3.00	1.60	1.00
$h\ (\mu m)$	368	368	368
M	0.03	1.48	0.70
$V\ (m/s)$	27	994	467
$v\ (m/s)$	0	985	312
$\beta\ (°)$	0	82.5	42.0
$\beta'\ (°)$	–	74.9	0

$r_b\omega\ (m/s)$	500
$\omega\ (rpm)$	$3 * 10^6$
R	0.026

Table 6.2: Turbine design parameters ($\gamma = 1.3$)

used. The rotor tip speed is set to $500m/s$ for the same material stress considerations as for the compressor.

The Euler equation (6.1) is still valid for the turbine rotor. The stagnation temperature is assumed constant across the inlet guide vanes, so that $T_{ta} = T_{tb} = T_{t4}$ and $T_{tc} = T_{t5}$ with $T_{t4} = 1600K$ and $T_{t5} = 1282K$. Station (a) is the stator inlet, (b) the stator exit and rotor inlet, (c) the rotor exit. The problem is solved exactly as for the compressor. In particular, the same mass flow conservation equation (6.2) has been used for defining the absolute Mach number at each station. A purely radial inlet absolute velocity has been considered, but we kept the option of having swirl at the exit of the rotor.

6.3.2 Results

The results are presented in Table 6.2 and in Figure 6-3.

The turbine rotor tip radius is the same as that of the compressor rotor. Indeed, the maximum tip speed is the same in both cases ($500m/s$) and the rotational speed is obviously the same.

As for the compressor, the blade design will be very challenging because very high angles are necessary for achieving the desired pressure ratio. At the stator exit, the absolute velocity is almost tangential. The turning across the rotor has been reduced by keeping some swirl at the exit: the velocity is purely radial in the relative frame. A very low stator inlet velocity was necessary for keeping the height constant along

the radius, but this is not a concern as it was for the compressor, because this time the pressure gradient is favorable. Reference [17] suggests to use a definition of the degree of reaction based on the temperature instead of the one given in Equation (6.3):

$$R = \frac{T_b - T_c}{T_{tb} - T_{tc}}.$$

The turbine degree of reaction is very low, showing that we have almost an impulse turbine. The biggest part of the pressure drop is taken across the stator, resulting in a relatively small static pressure difference and thus a relatively small density difference across the rotor blades. This factor allows a constant blade height in the rotor.

6.4 Combustor Design

Designing a micro-combustor is one of the most challenging parts of this project. The chemical reaction time is independent on the size of the burner. Since the reaction chamber is much smaller in the microengine than in typical gas turbine, the residence time in the micro-burner is smaller. Therefore, methods must be found to accelerate the mixing and combustion processes. One possible idea is to use hydrogen instead of hydrocarbon fuels. Hydrogen has a characteristic reaction time, a diffusion velocity in air and a vaporization rate larger by a factor 10 than conventional hydrocarbons [3]. It also presents other advantages such as very high heating value $H = 120MJ/kg$ and wide flammabilty limits (from 4% to 75% volume). The autoignition temperature of H_2 ($858K$) is higher than that of hydrocarbons ($500K$).

In addition to these favorable properties of hydrogen, placing the injectors upstream of the compressor would increase the residence time and help the mixing process. As long as no recuperator is introduced, the operating temperature upstream of the burner remains below the autoignition conditions. However, premixing could cause some problems, since gas bearing must be supplied with compressed air from the compressor. Ignition could occur in the case of shaft and sleeve contact during operation, for hydrogen ignition energy is very low.

Due to the high temperature capability of ceramics, no cooling is required for lean equivalence ratios. This represents a consequent gain in simplicity for the burner.

This work does not go far in the details but just gives a rough sketch of the burner. Reference [3] suggests that premixing allows combustor residence times as low as $0.5ms$. The flow velocity at the exit of the compressor stator is $25m/s$ but expansion can reduce it down to $10m/s$. Thus, a $5mm$ long burner would be sufficient.

Injection could be done through a series of holes in the flow intake. The fuel pressure and the hole diameter are the parameters to be optimized for getting good jet penetration to the center of the flow as well as for good mixing, but this is beyond the scope of this analysis.

6.5 Bearings Design

Chapter 3 demonstrated that gas bearings could provide sufficient load capability without dissipating too much power in viscous losses. This analysis was done with hemispherical gas bearings which presented many advantages on other geometries. However, while large scale hemispheres are easy to manufacture, this is not true at micro-scale where microfabrication techniques do not readily allow 3-D shapes. Therefore, disc thrust bearings and journal gas bearings have to be considered for practical applications. Figures 3-1 and 6-4 give examples of combinations of these two kind of bearings. Reference [6] details the load capability and the friction torque of these two geometries.

6.5.1 Journal Bearings

Journal bearings are slightly different from what had been developed in Chapter 3. Three geometric parameters are of importance for a journal bearing: the radius, the clearance and the length of the journal (L). The bearing number definition is similar to Equation (3.1), but now the load capability is given by:

$$Load_{radial} = \bar{K} P_a L D$$

where $\bar{K}$ is given by curves for plain cylindrical journal gas bearings as a function of Λ and L/D [7]. The friction torque is expressed by the Petroff equation [6]:

$$T = \frac{2\pi\mu R^3 L\omega}{C}$$

The length of the bearing logically influences the torque (since the surface is directly related to it), but it must be noticed that the pressure does not appear in this formula.

The journal bearing is subject to the most critical loads due to the very high rotational speed. For instance, if a $20mg$ shaft rotating at $3 * 10^6 rpm$ has its center of gravity displaced by $1\mu m$ from the centerline, the unbalance force is:

$$F_u = m\ \delta r\ \omega^2$$

or

$$F_u = 1.97\ N$$

The bearing should then be able to stand this unbalance force. However, when the bearing load capability increases, the power loss due to friction increases as well. Indeed, since the pressure and the rotational speed are fixed, the remaining parameters are R, L, and C. They all appear in the expressions of the load and of the torque. Therefore, the load capability cannot be increased without increasing the viscous losses, which should be as low as possible. One way to maximize the load to torque ratio is to use bearings with low compressibility numbers (between 10 and 20) and with L/D near 1. In addition, the desired compressor and turbine clearances ($\approx 1\mu m$) set C to $1\mu m$. All these considerations lead to the journal bearing design presented in Table 6.3. A pressure of 7 atm has been used instead of the 4.6 obtained at the exit of the compressor, because the spiral grooved thrust bearing can build up this pressure (see Figure 6-4).

$R\ (mm)$	0.4
$L\ (mm)$	2
$C\ (\mu m)$	1
$P_a\ (atm)$	7
$\omega\ (rpm)$	$3 * 10^6$
$\mu\ (N.s.m^{-2})$	$30.30 * 10^{-6}$
Λ	13
$Load_{radial}\ (N)$	1.65
$Power\ (W)$	2.4

Table 6.3: Plain cylindrical journal gas bearing

6.5.2 Thrust Bearings

The thrust bearing insures the axial position of the rotor and therefore is not subject to stringent constraints as is the journal bearing (no centrifugal acceleration, just the residual thrust load). The load requirement can be estimated by calculating the total engine thrust and by assuming that all this force is carried by the rotor (usually, the force is shared between rotating and stationary parts). The nominal exhaust conditions $T_{t5} = 1300K$ and $P_{t5}/P_{amb} = 1.03$ lead to an exhaust velocity $V_{axial} = 145m/s$ $(M = 0.21)$ for a throttle radius of $r = 1.2mm$. The thrust is then given by

$$F = \dot{m}(V_5 - V_0) + (P_5 - P_0)A_5$$

which finally leads to a total thrust of $0.03N$. Thus, small axial load capabilities are sufficient for balancing the gas pressure forces on the rotor. Only one disc thrust bearing is considered necessary. We have placed it in the center of the shaft (as shown on Figure 6-5 with details on Figure 6-4) for several reasons:

- This location allows both sides of the rotor to expand freely during engine starting. The compressor and turbine clearances will then reduce simultaneously. A front or rear thrust bearing would not offer this advantage.

- The disc thrust bearing is fed in with gas at compressor exit pressure P_1 (see Figure 6-4). This disc is spiral grooved, thus pumping up the gas inward and increasing the pressure at the same time (see Chapter 3). This results in a

so-called "superambient pressure" P_2 with $P_2 > P_1$. The gas at higher pressure is split evenly between the two sides of the journal bearing.

- Taking air just at the compressor rotor exit would lead to a loss a load capability compared to the selected configuration. At this station, the absolute velocity is very high, inducing a static pressure smaller than the total pressure (3 compared to 4.6). The inlet pressure in the bearing would then be this low static pressure, thus reducing the radial load capability. Therefore, bearing gas must be taken after the compressor vanes, where the velocity is slow.

The advantages of this configuration are balanced by an inconvenience inherent to fuel premixing: the bearing is fed in with an air/hydrogen mixing which could burn in it. Moreover, if the burner ignition takes place upstream of the feed holes (see Figure 6-5), the gas would be at high temperature, thus constraining the structure more. However, it is believed that the ignition should be downstream of these holes, because mixing and vaporization are slower than burning, and the holes are half-way into the burner.

For the disc thrust bearing, the definition of the compressibility number is slightly different than before:

$$\Lambda = \frac{3\mu\omega(R_{out}^2 - R_{in}^2)}{P_a C^2}$$

The non-dimensional stiffness $\bar{K}$ is given as a function of Λ by curves depending on R_{in}/R_{out} [7]. The load capability is then:

$$Load_{axial} = \bar{K}\pi P_a(R_{out}^2 - R_{in}^2)$$

The friction has the following expression [6]:

$$T = \frac{\pi}{2}\frac{\mu\omega(R_{out}^4 - R_{in}^4)}{C}$$

The resulting thrust bearing design is detailed in Table 6.4.

R_{out} (mm)	0.6
R_{in} (mm)	0.4
C (μm)	1
P_a (atm)	5
ω (rpm)	$3 * 10^6$
μ $(N.s.m^{-2})$	$30.30 * 10^{-6}$
Λ	11
$Load_{azial}$ (N)	0.16
$Power$ (W)	0.5

Table 6.4: Spiral grooved disc thrust gas bearing

6.5.3 Summary

The bearing design led to one disc thrust bearing and one journal bearing split into two parts, as shown on Figures 6-5 and 6-4. The nominal axial load capability is $0.16N$ and the radial one is $1.65N$. Viscous forces result in a dissipation of $3.4W$ in the bearing.

6.6 Engine Drawing

The previous analysis has defined each component. All the results are now integrated for drawing the whole engine. Figure 6-5 represents a section of this engine. The fuel injection in the intake has been represented by channels coming from the outside of the device where the tank will be installed. The holes feeding in the thrust bearing have also been drawn, proposing a possible location. The back of the rotor discs is characterized by large gaps with the stationary parts. This is meant to reduce the aerodynamic friction losses. The shaft extends out through the intake nozzle. At low Reynolds number, this may induce a tangential velocity in the incoming flow, thus substituting for the missing compressor inducer. Last, no recuperator has been included, since it is believed that with the estimated component efficiencies, too much power would be lost due to pressure drop.

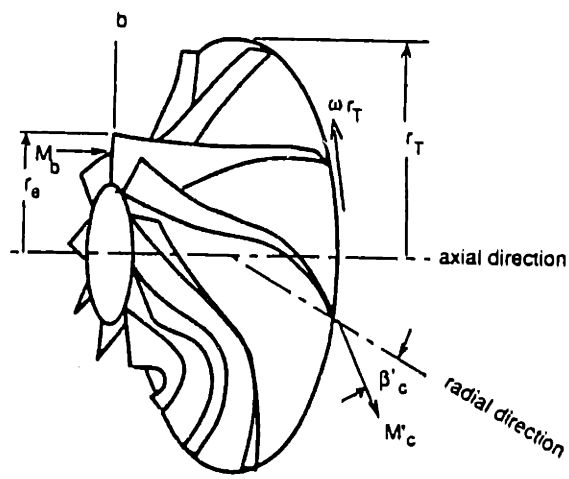

Figure 6-1: Inducer and impeller of a centrifugal compressor, with inlet and exit velocities (from reference [14]).

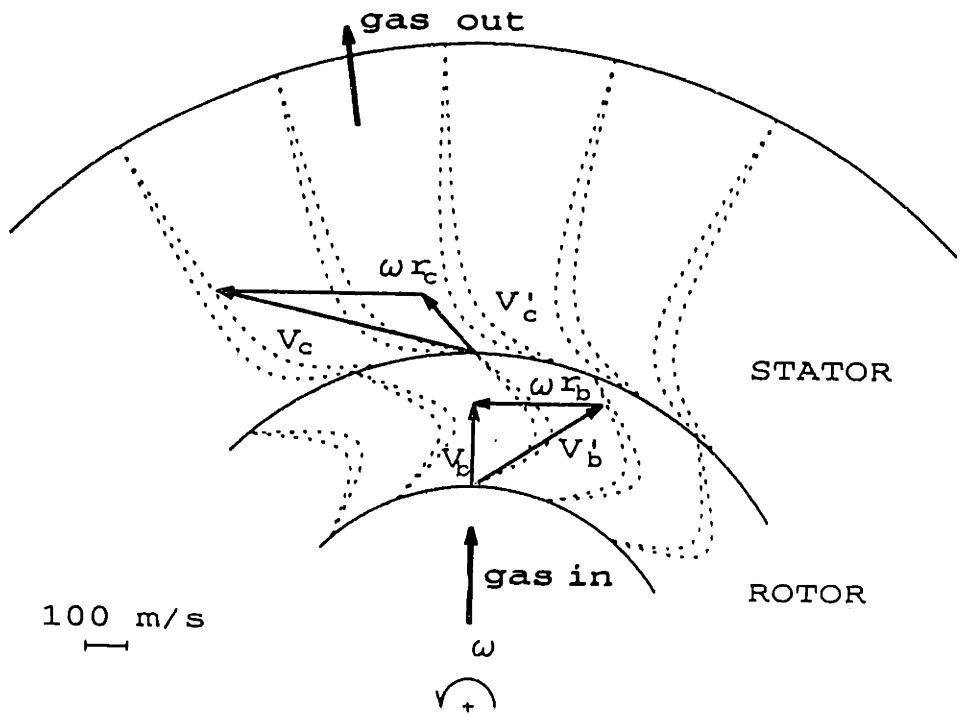

Figure 6-2: Compressor velocity triangles in the (r, t) plane ($V_{axial} = 0$, V is the velocity in the absolute frame, V' is in the relative one).

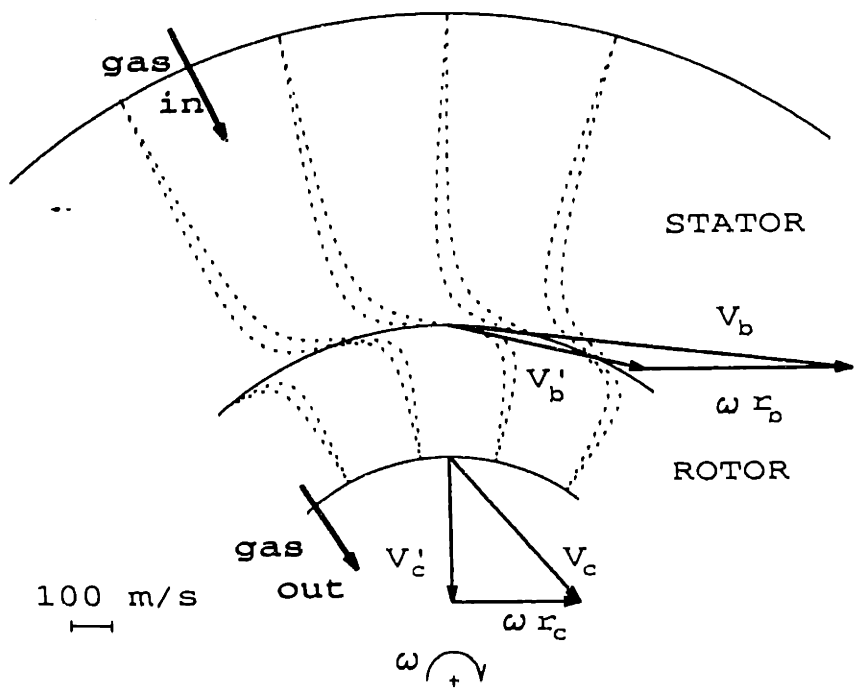

Figure 6-3: Turbine velocity triangles in the (r, t) plane ($V_{axial} = 0$, V is the velocity in the absolute frame, V' is in the relative one).

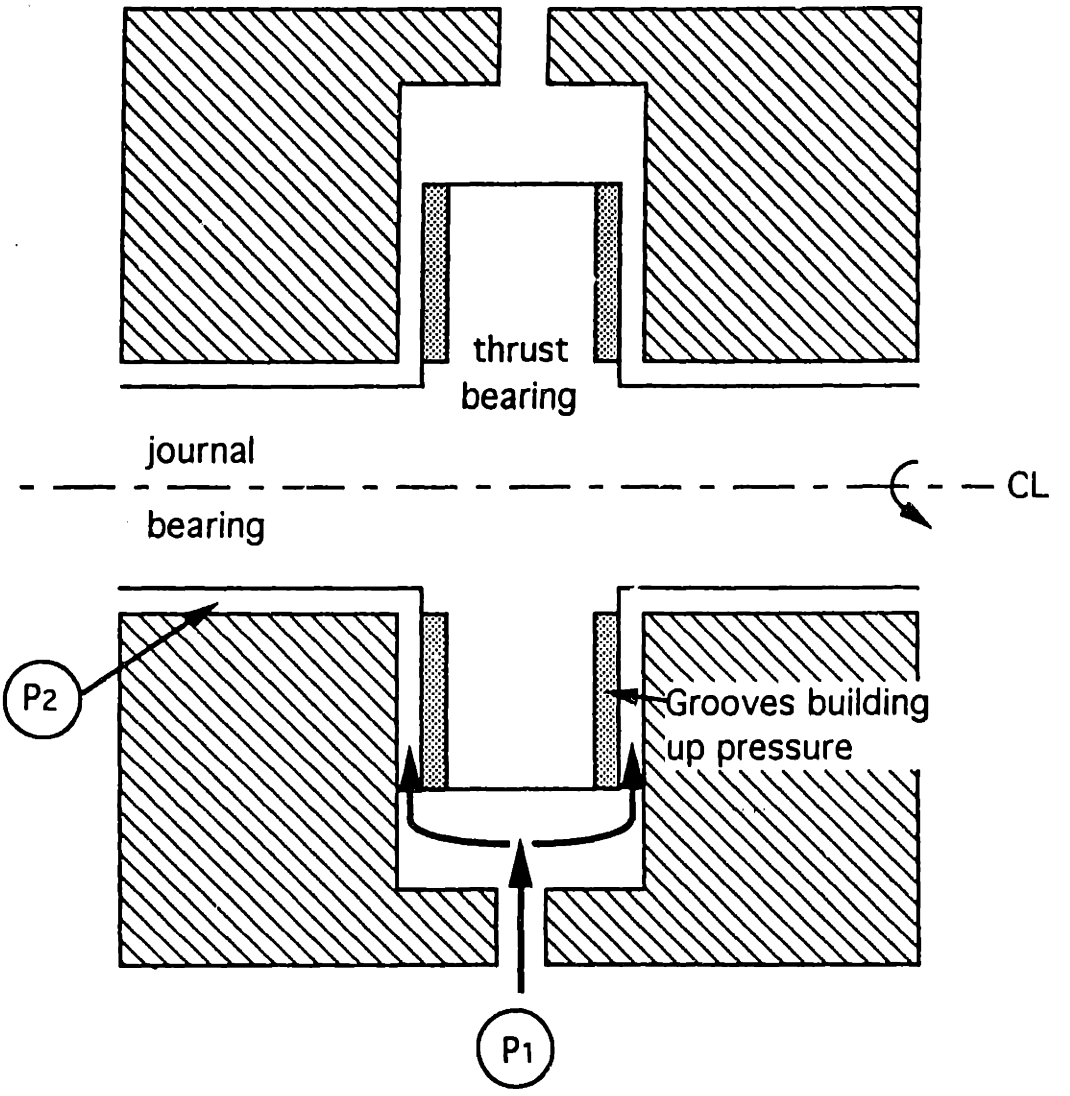

Figure 6-4: Journal and thrust bearing detail. Spiral grooves on the thrust bearing pump up gas and build up a pressure from P_1 to P_2 ($P_2 > P_1$).

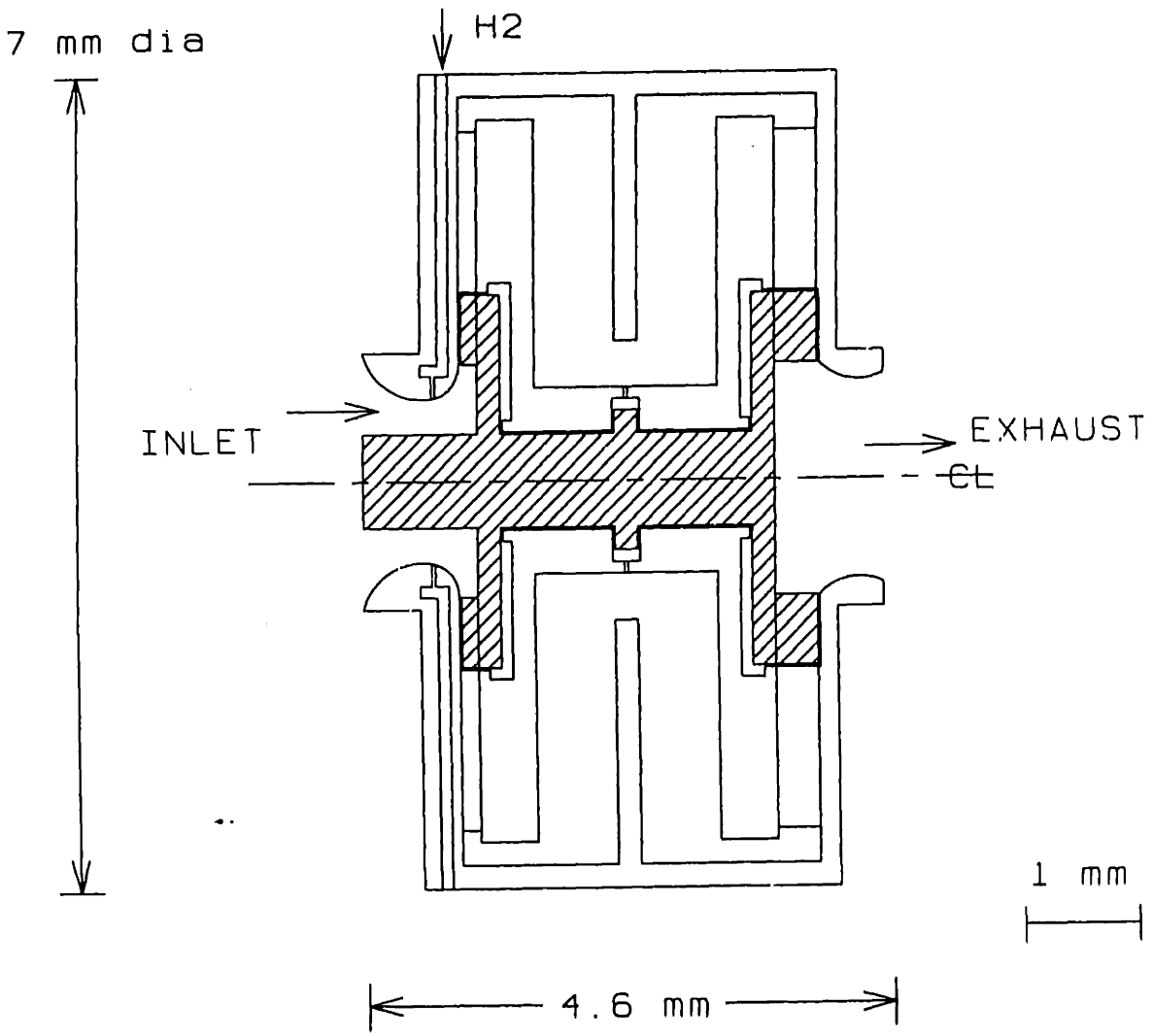

Figure 6-5: Engine drawing for $1mm^2$ intake area (scale 15:1). At design point: $\dot{m}_{air} = 1.8 * 10^{-4} kg/s$, $\pi_c = 4.6$, $\eta_c = 0.5$, $\eta_t = 0.7$, $\omega = 3 * 10^6 rpm$.

Chapter 7

Conclusions

This analysis suggests that it is feasible to realize a gas turbine in the micro-scale range. Even with low component efficiencies, it appears that useful levels of power can be extracted from such a device. Indeed, a microengine has been proposed which produces $12W$ of shaft power with $1mm^2$ intake area at a 4.6:1 pressure ratio. However, many challenges have been pointed out in addition to the one detailed in introduction:

- The design of the compressor and turbine blades is critical. Indeed, the high pressure ratio desired requires high tangential velocities, imposing large turning angles to the blades. This is accentuated by the constant height constraint imposed by microfabrication techniques, thus leading to small radial velocities at the large radii. This could lead to flow separation, which is already critical at low Reynolds numbers. One solution may be to introduce a height change between the rotor and the stator, thus reducing the effect of the manufacturing constraints.

- Small tolerances between rotating and stationary parts are desired to prevent parasitic leakage losses. However, they may also introduce large aerodynamic friction losses. The present analysis has considered these losses only in the bearings. But they should be estimated everywhere for an accurate prediction of power output. Material expansion under high temperature and centrifugal acceleration should then be considered in such an analysis.

- Introducing a micro-recuperator in the cycle is an efficient way to increase the Power Specific Fuel Consumption. This would allow a reduction in the size of the fuel tank which will dominate the overall package size as soon as more than a few minutes of power is required. However, the recuperator has pressure drops associated with it which reduce the maximum power output and therefore the margin above break-even. The actual level of performance does not allow any loss and recuperation should be postponed to further development of the project. Then, the autoignition problem of hydrogen should also be addressed.

- One solution suggested for obtaining good fuel mixing despite the burner low residence time is to inject hydrogen upstream of the compressor. However, the gas bearings must be fed in with compressed gas, which in this case would be an air/fuel mixture. Combustion could then occur in the bearings, leading to high temperatures which are not desirable.

- In the present work, gas bearings have been designed for carrying a typical rotor unbalance force. However, if the engine is operated at a frequency near the rotor critical frequency, larger loads could appear and the present design would not be appropriate. Moreover, gas bearings stability has not been addressed. Therefore, a more detailed gas bearing analysis should be conducted.

- Stress should be evaluated accurately in each part of the rotor. Several aspects make it critical. The high rotational speed generates very large centrifugal forces which may induce high stress concentrations. This could be critical especially at the sharp corners that micromachining imposes to the geometry.

- Since one important application for micro-gas turbines is electric power generation, the generator should be considered in the design of the gas turbine.

- The most critical constraints in building a micro-gas turbine engine probably remain those of microfabrication. As a prerequisite, this technique has to define clearly its limits on size and tolerance. A thermodynamically and mechanically satifying engine design must be consistant with micromachining technology.

Appendix A

Physical Properties of Air

The air physical properties are analytically approximated by the following equations [5], where T is the temperature in K:

Density (kg/m^3)

$$\rho = \frac{P}{287T}$$

Specific heat $(kJ/(kg.K))$

if $260K < T < 610K$

$$C_p(T) = 4180(0.249679 - 7.55179 * 10^{-5}T + 1.69194 * 10^{-7}T^2 - 6.46128 * 10^{-11}T^3)$$

if $610K < T < 1500K$

$$C_p(T) = 4180(0.239496 - 3.89538 * 10^{-5}T + 1.36120 * 10^{-7}T^2 - 6.40730 * 10^{-11}T^3)$$

Thermal conductivity $(W/(m.K))$

$$k(T) = 1.3003035 * 10^{-3} + 9.3676581 * 10^{-5}T - 4.4424691 * 10^{-8}T^2 + 2.3171580 * 10^{-11}T^3 - 6.5997572 * 10^{-15}T^4$$

Viscosity $(N.s/m^2)$

$$\mu(T) = 2.2879728 * 10^{-6} + 6.2597929 * 10^{-8}T - 3.1319564 * 10^{-11}T^2 + 8.1503801 * 10^{-15}T^3$$

Appendix B

Recuperator Design Study Results

	Cold side	Hot side
# of passages	4	4
height (μm)	31	145
D_h (m)	$6.15 * 10^{-5}$	$2.91 * 10^{-4}$
Re_{D_h}	147	87
h ($W/(m^2.K)$)	5522	2538
T_{in} (K)	528	1229
T_{out} (K)	1063	806
$V_{in,core}$ (m/s)	20	45
$V_{out,core}$ (m/s)	42	30
P_{out}/P_{in}	0.96	0.95
$P_{t,out}/P_{t,in}$	0.96	0.94

$\dot{m}$ (kg/s)	$1.8 * 10^{-4}$
core length (mm)	3
mean radius (mm)	3.5
wall thickness (μm)	10
NTU	2.46
C_{min}/C_{max}	0.791
ϵ	0.76

Table B.1: Selected concentric counterflow heat exchanger design.

	Cold side	Hot side
# of passages	4	4
height (μm)	31	145
D_h (m)	$6.15 * 10^{-5}$	$2.91 * 10^{-4}$
Re_{D_h}	147	87
h ($W/(m^2.K)$)	5526	2572
T_{in} (K)	528	1229
T_{out} (K)	994	861
$V_{in,core}$ (m/s)	20	45
$V_{out,core}$ (m/s)	39	32
P_{out}/P_{in}	0.97	0.95
$P_{t,out}/P_{t,in}$	0.97	0.94

$\dot{m}$ (kg/s)	$1.8 * 10^{-4}$
core length (mm)	2
mean radius (mm)	3.5
wall thickness (μm)	10
NTU	1.66
C_{min}/C_{max}	0.791
ϵ	0.66

Table B.2: Concentric counterflow heat exchanger with shorter core length than selected design.

	Cold side	Hot side
# of passages	5	5
height (μm)	25	119
D_h (m)	$4.92 * 10^{-5}$	$2.38 * 10^{-4}$
Re_{D_h}	118	70
h ($W/(m^2.K)$)	6912	3105
T_{in} (K)	528	1229
T_{out} (K)	1126	756
$V_{in,core}$ (m/s)	20	45
$V_{out,core}$ (m/s)	45	28
P_{out}/P_{in}	0.93	0.94
$P_{t,out}/P_{t,in}$	0.94	0.93

$\dot{m}$ (kg/s)	$1.8 * 10^{-4}$
core length (mm)	3
mean radius (mm)	3.5
wall thickness (μm)	10
NTU	3.79
C_{min}/C_{max}	0.791
ϵ	0.85

Table B.3: Concentric counterflow heat exchanger with more passages than selected design.

	Cold side	Hot side
# of passages	4	4
height (μm)	31	145
D_h (m)	$6.15 * 10^{-5}$	$2.91 * 10^{-4}$
Re_{D_h}	147	87
h ($W/(m^2.K)$)	5525	2539
T_{in} (K)	528	1229
T_{out} (K)	1063	806
$V_{in,core}$ (m/s)	20	45
$V_{out,core}$ (m/s)	42	30
P_{out}/P_{in}	0.96	0.95
$P_{t,out}/P_{t,in}$	0.96	0.94

$\dot{m}$ (kg/s)	$1.8 * 10^{-4}$
core length (mm)	3
mean radius (mm)	3.5
wall thickness (μm)	40
NTU	2.46
C_{min}/C_{max}	0.791
ϵ	0.76

Table B.4: Concentric counterflow heat exchanger with larger wall thickness than selected design.

	Cold side	Hot side
# of passages	4	4
height (μm)	41	159
D_h (m)	$8.19 * 10^{-5}$	$3.19 * 10^{-4}$
Re_{D_h}	147	87
h ($W/(m^2.K)$)	4150	2316
T_{in} (K)	528	1229
T_{out} (K)	1037	827
$V_{in,core}$ (m/s)	15	40
$V_{out,core}$ (m/s)	30	27
P_{out}/P_{in}	0.98	0.95
$P_{t,out}/P_{t,in}$	0.98	0.95

$\dot{m}$ (kg/s)	$1.8 * 10^{-4}$
core length (mm)	3
mean radius (mm)	3.5
wall thickness (μm)	10
NTU	2.10
C_{min}/C_{max}	0.791
ϵ	0.73

Table B.5: Concentric counterflow heat exchanger with lower core inlet velocities than selected design.

	Cold side	Hot side
# of passages	4	4
height (μm)	25	137
D_h (m)	$4.93 * 10^{-5}$	$2.74 * 10^{-4}$
Re_{D_h}	147	87
h ($W/(m^2.K)$)	6888	2700
T_{in} (K)	528	1229
T_{out} (K)	1080	792
$V_{in,core}$ (m/s)	25	50
$V_{out,core}$ (m/s)	55	33
P_{out}/P_{in}	0.92	0.94
$P_{t,out}/P_{t,in}$	0.92	0.93

$\dot{m}$ (kg/s)	$1.8 * 10^{-4}$
core length (mm)	3
mean radius (mm)	3.5
wall thickness (μm)	10
NTU	2.74
C_{min}/C_{max}	0.791
ϵ	0.79

Table B.6: Concentric counterflow heat exchanger with higher core inlet velocities than selected design.

Appendix C

GASTURB 6.0 Cycle Deck

C.1 GASTURB Modifications for Hydrogen Fueled Engines

The inital version of GASTURB 6.0 considers only fuels such as hydrocarbons with 86.08 % mass of carbon and 13.92 % mass of hydrogen and characterized by a Lower Heating Value $H_{C_mH_n,T_R} = 43.1$ MJ/kg at $T_R = 288$ K. This composition matches closely kerosene, JP-4 and other fuels used in aviation and for stationary gas turbines [16]. Moreover, the burned gases characteristics such as specific heat at constant pressure (c_p), enthalpy (h) and entropy (Ψ) are given as functions of the temperature for this kind of fuel:

$$c_p(T,f) = \frac{c_{p,air}(T) + f * \Theta_{c_p}(T)}{1+f} \tag{C.1}$$

$$h(T,f) = \frac{h_{air}(T) + f * \Theta_h(T)}{1+f} \tag{C.2}$$

$$\Psi(T,f) = \frac{\Psi_{air}(T) + f * \Theta_\Psi(T)}{1+f} \tag{C.3}$$

where:

Θ is a correction term function of the temperature only

f is the fuel-to-air ratio.

The energy balance then gives the fuel-to-air ratio (with the assumption that the fuel is at ambient temperature T_R):

$$f = \frac{h_{air,T_{t4}} - h_{air,T_{t3}}}{ECV(T_{t4})}$$

where ECV is the Effective Caloric Value defined by:

$$ECV(T_{t4}) = H_{C_mH_n,T_R} - \Theta_{h,T_{t4}} + \Theta_{h,T_R} \tag{C.4}$$

All these formula were adapted so that hydrogen could be studied as a fuel. The Lower Heating Value is now $H_{H_2} = 120\text{MJ/kg}$. The air properties remain the same but the new correction terms Θ and ECV have to be derived from basic equations.

If the combustion reaction is complete, then it can be described by:

$$H_2 + \frac{1}{2\Phi}(O_2 + 3.78N_2) \longrightarrow H_2O + (\frac{1}{2\Phi} - \frac{1}{2})O_2 + \frac{3.78}{2\Phi}N_2 \tag{C.5}$$

where Φ is the equivalence ratio defined by:

$$\Phi = \frac{f}{f_{stoichiometric}} = \frac{f}{0.0290}$$

Before the reaction occurs, the air specific heat is given by:

$$\dot{m}_{air,before}\ c_{p,air} = \dot{m}_{O_2,before}\ c_{p,O_2} + \dot{m}_{N_2,before}\ c_{p,N_2} \tag{C.6}$$

with

$$\dot{m}_{air,before} = \dot{m}_{O_2,before} + \dot{m}_{N_2,before} \tag{C.7}$$

Before the reaction, for each mole of O_2, there are 3.78 moles of N_2. Therefore, we

have:

$$\dot{m}_{N_2,before} = \dot{N}_{N_2,before} * M_{N_2} = (3.78\dot{N}_{O_2,before}) * M_{N_2} = 3.78 M_{N_2}(\frac{\dot{m}_{O_2,before}}{M_{O_2}})$$

where $\dot{N}$ is a mole flow rate

so that

$$\dot{m}_{N_2,before} = 3.78\frac{14}{16}\dot{m}_{O_2,before}$$

Replacing in Equation C.7 then gives:

$$\dot{m}_{air,before} = (1 + 3.78\frac{14}{16})\dot{m}_{O_2,before} \tag{C.8}$$

Now considering the gas after the reaction, we can calculate the average specific heat $\bar{c_p}$:

$$\dot{m}_{gas}\ \bar{c_p} = \dot{m}_{H_2O,after}\ c_{p,H_2O} + \dot{m}_{O_2,after}\ c_{p,O_2} + \dot{m}_{N_2,after}\ c_{p,N_2} \tag{C.9}$$

Using the mass conservation and the definition of the fuel-to-air ratio f, the gas mass flow can be expressed as:

$$\dot{m}_{gas} = \dot{m}_{air,before} + \dot{m}_{fuel,before} = \dot{m}_{air,before}(1 + f) \tag{C.10}$$

According to Equation C.5, the mass flows of oxygen before and after combustion are linked by:

$$\dot{m}_{O_2,after} = \frac{\frac{1}{2\Phi} - \frac{1}{2}}{\frac{1}{2\Phi}}\ \dot{m}_{O_2,before}$$

or

$$\dot{m}_{O_2,after} = \dot{m}_{O_2,before} - \Phi\ \dot{m}_{O_2,before} \tag{C.11}$$

Nitrogen is considered as inert, so that Equation C.9 can now be written as follow (with Equations C.10 and C.11):

$$\dot{m}_{air,before}(1 + f)\ \bar{c_p} = \dot{m}_{H_2O,after}\ c_{p,H_2O} - \Phi\ \dot{m}_{O_2,before}\ c_{p,O_2} + (\dot{m}_{O_2,before}\ c_{p,O_2} + \dot{m}_{N_2,before}\ c_{p,N_2})$$

Between the parentheses, we then recognize the specific heat of air before the reaction, so that:

$$\dot{m}_{air,before}(1+f)\,\bar{c_p} = \dot{m}_{H_2O,after}\;c_{p,H_2O} - \Phi\;\dot{m}_{O_2,before}\;c_{p,O_2} + \dot{m}_{air,before}\;c_{p,air} \quad \text{(C.12)}$$

By using Equation C.8 and writing that:

$$\dot{m}_{H_2O,after} = \frac{18}{32}\frac{1}{\frac{1}{2\Phi}}\;\dot{m}_{O_2,before} = \frac{9}{8}\Phi\;\dot{m}_{O_2,before}$$

we get the final expression of Equation C.12:

$$(1+f)\bar{c_p} = c_{p,air} + \Phi\frac{1}{1+3.78\frac{14}{16}}(-c_{p,O_2} + \frac{9}{8}c_{p,H_2O})$$

or

$$\bar{c_p} = \frac{c_{p,air} + f(-8c_{p,O_2} + 9c_{p,H_2O})}{1+f} \quad \text{(C.13)}$$

Equation C.13 has the same form as Equation C.1 of the source program GAS-TURB with Θ_{c_p} defined as:

$$\Theta_{c_p}(T) = -8c_{p,O_2}(T) + 9c_{p,H_2O}(T)$$

Equation C.2 is obtained by integration:

$$h(T) = \int_0^T c_p(T)dT$$

and by noting that integration is a linear function. Θ_h is then defined by:

$$\Theta_h(T) = \int_0^T \Theta_{c_p}(T)dT$$

Identically, since entropy is defined by:

$$\Psi(T) = \frac{1}{R}\int_0^T \frac{c_p(T)}{T}dT$$

the correction factor Θ_Ψ of Equation C.3 is defined as:

$$\Theta_\Psi(T) = \frac{1}{R}\int_0^T \frac{\Theta_{c_p}(T)}{T} dT$$

Practically, $c_{p,O_2}(T)$ and $c_{p,H_2O}(T)$ are expressed as polynomial functions of the temperature:

$$c_p = C_0 + C_1 T + C_2 T^2 + ...$$

so that the correction coefficients can also be expressed the same way.

The Effective Caloric Value ECV (EKV in the program) has been obtained by using its definition C.4.

All the changes that had to be made have now been defined. The two files which needed to be modified were SIMPPROP.PAS and GLOB_CYC.PAS. The latter contains the lower heating value (denoted FHV in the program) and the former defines all the gas characteristics described above. The modified files have been compiled with Borland Pascal 7.0.

C.2 Engine Cycle Optimization with and without a Recuperator

GASTURB 6.0 allows cycle optimization when you specify the variables to be changed, the constraints and the figure of merit. Two cases have been considered: one without a recuperator, the other with it. The first case has been solved by using the configuration called "Single Spool Jet, Turboshaft, Turboprop" and by selecting the option Turboshaft in the input window. The power output is then automatically determined in order to produce the desired nozzle pressure ratio ($P_{t5}/P_{amb} = 1.03$ in our case). Table C.1 summarizes the GASTURB inputs for this configuration. The 0-0.3kW range for P_{out} leads to fast and precise iterations for defining the optimum.

However, recuperation is not an option in the Single Turboshaft Engine menu but is proposed for a "Two Spools Turboshaft, Turboprop" engine, so that this configu-

	Parameters	Range
Variable	π_c	$2.5 - 5$
	$P_{out}\ (kW)$	$0 - 0.03$
Constraints	–	
Figure of merit	$PSFC$	*minimized*

Table C.1: Optimization inputs for GASTURB 6.0 for an engine without recuperator.

	Parameters	Range
Variables	π_c	$2.5 - 5$
	$P_{out}\ (kW)$	$0 - 0.03$
Constraints	$\pi_{PowerTurbine}$	$1.000 - 1.001$
Figure of merit	$PSFC = WF/PWX$	*minimized*

Table C.2: Optimization inputs for GASTURB 6.0 for an engine with recuperator.

ration has to be chosen. The way to simulate a single spool engine is to iterate the cycle in order t , set the Power Turbine pressure ratio to 1: this way the power turbine does not produce any work and all the turbine power excess goes out through the power offtake (PWX). Table C.2 summarizes the GASTURB inputs for the recuperated gas turbine. The power turbine pressure ratio has been constrained to remain in the 1-1.001 range for the reason explained above. The PSFC is not defined for this configuration, so that a composed value WF/PWX (fuel massflow rate divided by power output) has been used.

Bibliography

[1] Allied-Signal Aerospace Company, "Advanced Gas Turbine AGT Technology Development Project", Final Report to NASA Lewis Research Center, DOE/NASA 0167-12, March 1988.

[2] Allison Gas Turbine Division, "Advanced Gas Turbine AGT Technology Project", Final Report to NASA Lewis Research Center, DOE/NASA 0168-11, August 1988.

[3] Epstein,A.H., Groshenry,C., Haldeman,C.W., Schmidt,M.A., Senturia,S.D., Tan,C.S., Waitz,I.A., Wong,J., "Microjet Engines, Final Technical Report", MIT, April 1995.

[4] Geary,P.J., "Fluid Film Bearings", British Scientific Instrumentation Research Association, Report R.286, pp.7-10,42-49, 1962.

[5] General Electric Company, "Fluid Flow Data Book", Genium Publishing Corporation, N.Y., 1988

[6] Grassam,N.S., Powell,J.W., "Gas Lubricated Bearings", Butterworths, London, 1964.

[7] Gross,W.A., Matsch,L.A., Castelli,V., Eshel,A., Vohr,J.H., Wildmann,M., "Fluid Film Lubrication", John Wiley & Sons, New York, 1980.

[8] Jane's Information Group, "Jane's All the World's Aircraft", Mark Lambert, 1993-94.

[9] Japikse,D., "Turbocharger Turbine Design and Development", Creare Incorporated, Hanover,NH, p.5-6, 1977.

[10] Kays,W.M. ndon,A.L., "Compact Heat Exchangers", McGraw-Hill Book Company, New York, pp.15-19,120, 1984.

[11] Kays,W.M., Crawford,M.E., "Convective Heat and Mass Transfer", McGraw-Hill, Inc., pp.111,301,419-421,424-427, 1993.

[12] Keating,W.H., "Gas Bearings", Sensor Systems Modeling, Report R-1000, Section 2.4.2, pp.1-28.

[13] Keating,W.H., "A Comparison of the Spool, Cone and Hemisphere Spin-Axis Gas-Bearing Configurations from the MTI Infinite-Groove Theory", Instrumentation Laboratory, Massachusetts Institute of Technology, E-2223, Feb. 1968.

[14] Kerrebrock,J.L., "Aircraft Engines and Gas Turbines", The MIT Press, Cambridge, USA, pp.192, 1992.

[15] Kreith,F., "Principles of Heat Transfer", International Textbook Company, Scranton, 1958.

[16] Kurzke,J., "GASTURB Version 6.0 User's Manual", Germany, 1995.

[17] Mattingly,J.D., Heiser,W.H., Daley,D.H., "Aircraft Engine Design", AIAA Eduaction Series, Washington, 1987, pp.240,242.

[18] Mehregany,M., Senturia,S.D., Lang,J.H., "Measurement of Wear in Polysilicon Micromotors", IEEE Trans. on Electron Devices, Vol.39, No.5, pp.131-138, May 1992.

[19] Osborne,C., "Turbocharger Compressor Design and Development", Creare Incorporated, Hanover,NH, p.4-13, 1977.

[20] Shah,R.K., London,A.L., "Laminar Flow Forced Convection in Ducts", Academic Press, New York, 1978.

[21] Watson,J.T.R., "Viscosity of Gases in Metric Units", National Engineering Laboratory, Edinburgh, HMSO, pp.2,6,22, 1972.